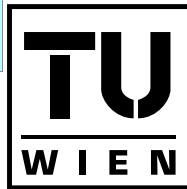


Die approbierte Originalversion dieser Dissertation ist an der Hauptbibliothek der Technischen Universität Wien aufgestellt (<http://www.ub.tuwien.ac.at>).

The approved original version of this thesis is available at the main library of the Vienna University of Technology (<http://www.ub.tuwien.ac.at/englweb/>).



TECHNISCHE
UNIVERSITÄT
WIEN
VIENNA
UNIVERSITY OF
TECHNOLOGY

DISSERTATION

Experimental and Numerical Investigations of Perforated FRP- Laminates

*ausgeführt zum Zwecke der Erlangung des akademischen Grades eines
Doktors der technischen Wissenschaften unter der Leitung von*

o.Univ.Prof. Dipl.-Ing. Dr.techn. Franz G. Rammerstorfer
E317
Institut für Leichtbau und Flugzeugbau

eingereicht an der Technischen Universität Wien
Fakultät für Maschinenbau

von

Dipl.-Ing. Dieter H. Pahr
Matr.Nr.: 9326307
Stuben 71
7434 Bernstein

Wien, im Feber 2003

Dieter H. Pahr

Acknowledgments

This work was carried out in the course of my employment as “Universitätsassistent” at the Institute of Lightweight Structures and Aerospace Engineering (ILFB) at the Vienna University of Technology. I am deeply indebted to my thesis advisor, Prof. Dr. F.G. Rammerstorfer, head of the above Institute, for his assistance in preparing this work and his advice in many discussions.

I also like to thank Prof. Dr. S. Seidler from the Institute of Materials Science and Testing for acting as coadvisor for this thesis.

Many thanks are given to Prof. Dr. H. W. Weber and his team from the Atomic Institute of the Austrian Universities for making experimental testing equipment available.

The financial support for parts of the research work by FACC AG (Fischer Advanced Composite Components, Ried, Austria) under the framework of the Austrian Aeronautics Research/Network (AAR), as well as the financial support for the numerical calculations by the “Hochschuljubiläumsstiftung der Stadt Wien”, is gratefully acknowledged.

Additionally, I would like to express my thanks to all colleagues at the ILFB, who have always been helpful and friendly. The resulting positive atmosphere at the ILFB has helped me during many scientific setbacks and made my time at the ILFB an interesting, inspiring and joyful period.

Special thanks are given to my neglected family, especially to my son Achim and my wife Silvia.

Kurzfassung

Die hier präsentierte wissenschaftliche Arbeit zeigt die Entwicklung einer auf Finiten Elemente basierenden Methode zur Untersuchung des mechanischen Verhaltens von inhomogenen Materialien unter monotoner statischer Belastung sowie deren experimentelle Untersuchung. Die Inhomogenitäten, deren Topologie, Geometrie und Materialverhalten das effektive Materialverhalten stark beeinflussen, können dabei auf verschiedenen Längenskalen auftreten. Im Falle der hier näher betrachteten perforierten (akustischen) Faserverbund Lamine treten auf den verschiedenen Längenskalen folgende Inhomogenitäten auf:

- Makroskala ... periodisch angeordnete Löcher (Perforationen)
- Mesoskala ... verschiedene Laminatschichten
- Mikroskala ... Faser und Matrix
- ...

Im vorliegenden Fall erfolgt eine Modellierung bis zur Mesoskala unter der Verwendung von Einheitszellen Modellen und hierarchischen Meso-Makro- (Zwei-Skalen-) Konzepten.

Perforierte Lamine werden zum Beispiel als Deckschichten bei Sandwich-Verbunden in Flugzeugtriebwerken verwendet, welche neben ihren aero- und strukturmechanischen Funktionen auch die Aufgabe haben, Schall zu absorbieren. Da diese Verbunde beachtliche mechanische Lasten aufnehmen müssen, sind das effektive Steifigkeitsverhalten, die lokale Spannungsverteilung und das effektive Festigkeitsverhalten von Interesse.

Für die Berechnung des effektiven Steifigkeitsverhalten perforierter Lamine wurde die Homogenisierungsmethode verwendet. Homogenisierung bedeutet in diesem Zu-

sammenhang, dass das aktuelle inhomogene Material (z.B. der perforierte Verbundwerkstoff) durch ein äquivalentes homogenes Material ersetzt werden kann, wobei die berechnete homogenisierte Steifigkeit das gleiche makroskopische Materialverhalten ergibt wie der perforierte Verbundwerkstoff.

Die hier beschriebenen Versagensuntersuchungen basieren vorwiegend auf linearen 3D Finite Elemente Einheitszellen Modellen, welche inter-laminare Spannungen (Folge von freien Rand Effekten) berücksichtigen. Verschiedene Versagensmodelle wurden für die Festigkeitsvorhersagen von perforierten Laminaten entwickelt. In dieser Arbeit wird ein auf gemittelten Spannungen basierendes Versagensmodell verwendet. Bei diesem Modell werden anstelle von tatsächlich berechneten Spannungen gemittelte Spannungen um den Lochrand verwendet und dienen, in Verbindung mit Anfangsfestigkeiten, als Eingabewerte für 3D Versagenskriterien. Verwendete Versagenskriterien sind: Das Tsai-Wu Kriterium, das Maximalspannungskriterium, das 3D Puck Kriterium und ein Delaminationskriterium. Das Ziel der Versagensanalyse ist die Berechnung eines Sicherheitsfaktors oder einer Anstrengung (Risiko Faktors) für alle möglichen Lastkombinationen in der Ebene. Das Ergebnis dieser Berechnungen sind Anfangsversagenflächen in einem makroskopischen Membrankraftraum.

Mit Hilfe der berechneten effektiven Steifigkeiten und Anfangsversagenflächen können die Deformationen, die Festigkeit und das Stabilitätsverhalten von Strukturen, welche perforierte Lamine enthalten, einfach und schnell auf der Strukturebene, d.h. Makroebene, erfolgen. Dabei muss weder bei der Finite Elemente Diskretisierung noch bei der Ermittlung der Spannungsfelder auf die Perforationen explizit Rücksicht genommen werden.

Abschliessend wurden die vorgestellten numerischen Modelle mittels Experimenten verifiziert. Zugversuche an perforierten und nicht perforierten Laminaten wurden in Verbindung mit akustischen Emissionsmessungen durchgeführt, um die entsprechenden Steifigkeiten und den Beginn des Versagens (Anfangsfestigkeiten) zu ermitteln. Die erhaltenen Versuchsergebnisse zeigten eine gute Übereinstimmung mit den numerischen Ergebnissen.

Abstract

This work shows the development of a the finite element based two-scale analysis method to study problems related to the mechanical behavior of inhomogeneous materials under monotone static loading conditions, as well as, their experimental investigation. The inhomogeneities, which influence the effective mechanical response by their topology, geometry and material behavior, can occur on different length scales. In the case of perforated (acoustic) laminates, which are studied in this work, the following inhomogeneities are evident on the different length scales:

- Macro-scale ... periodically arranged holes (perforations)
- Meso-scale ... different laminae (plies)
- Micro-scale ... fiber and matrix material
- ...

In the current case the modeling goes down to the meso-scale and is realized by unit cell models and hierarchical meso-macro (two-scale) concepts.

Perforated laminates are applied, e.g., as face sheets in sandwich compounds in the casing of aircraft turbine engines. They are designed for absorbing noise and, in the most cases, they must carry mechanical loads as well. Hence, the effective stiffness behavior, the local stress distribution in the individual layers, and the effective strength of the perforated laminate are of interest.

For calculating the effective stiffness behavior of perforated laminates the homogenization method is applied. Homogenization means that the actual inhomogeneous material (e.g., the perforated composite) is replaced by an equivalent homogeneous material, with the calculated homogenized stiffness leading to the same macroscopic deformation behavior.

The described failure investigations are based on linear 3D finite element unit cell calculations, where inter-laminar stresses (due to free edge effects) are taken into account. Numerous failure models have been developed for strength predictions in perforated laminates. In this work a stress based failure model, the average stress model, is used. In this model averaged stresses (instead of true stresses around the hole) are used in combination with first ply failure (FPF) strength values, as input for different 3D failure criteria. Applied failure criteria are: The Tsai-Wu criterion, the maximum stress criterion, the new Puck criterion, and a delamination criterion. The goal of the failure analysis is to calculate a safety factor or risk parameter for all possible in-plane loading combinations. The results of these computations are failure-initiation surfaces in the space of macro-membrane forces.

The deformation and strength evaluation of structures, which contain such perforated laminates, can be performed simply and fast on the structural level (macroscopic level) by using the effective stiffness and the failure-initiation surfaces. Furthermore, the structural analysis does not need to account explicitly for the perforations, neither in the finite element discretization nor in the evaluation of stress fields.

Finally the introduced numerical models are verified by experiments. Tensile tests on perforated and non-perforated laminates are performed in combination with acoustic emission measurements to obtain the first ply failure strengths of the perforated and non-perforated laminate. The obtained test results shows good agreement with the numerical predictions.

Contents

1	Introduction	1
1.1	Introduction to Composite Materials	1
1.1.1	The What - What is a Composite Material?	2
1.1.2	The Why - Advantages of Fiber Reinforced Composite Materials	2
1.1.3	The How - Applications of Composite Materials	4
2	Literature Review	7
2.1	Failure and Damage of Layered Laminates	7
2.1.1	Overview	7
2.1.2	Detailed Descriptions of the Failure Modes	9
2.2	Failure Analysis of Laminates with Low Stress Gradients	12
2.2.1	Introduction to Failure Models	12
2.2.2	Failure Hypotheses for Low Stress Gradients	15
2.2.3	Remarks on the Modeling of Layered Laminates Composed of Woven Fabric Layers	26
2.3	Failure Analyses of Laminates with High Stress Gradients	27
2.3.1	Free Edge Effect	27
2.3.2	Geometry Effect of a Hole	29
2.3.3	Computation of Concentrated Stresses within Perforated Laminates	30
2.3.4	Failure Models for Laminates with High Stress Gradients	31

2.4	Introduction to the Acoustic Emission Technique	35
2.4.1	Schematic Test Setup	36
2.4.2	Acoustic Emission Signals - Events	36
2.4.3	Linear Source Location Technique	38
3	Homogenization	42
3.1	Mathematical Background	42
3.1.1	Coordinate Systems	42
3.1.2	Introduction to Tensor and Index Notation	43
3.1.3	General Remarks on Vectors, Matrices and Tensors	45
3.1.4	Kronecker Delta and ϵ -Tensor	47
3.1.5	Divergence Theorem	49
3.2	Homogenization from the View Point of Standard FEM	49
3.2.1	Introduction	49
3.2.2	Description of a Periodic Medium	50
3.2.3	Homogenized Stresses and Strains	52
3.2.4	Summary of the Homogenization Problem	61
4	Determination of Material Properties	63
4.1	Tensile Test Specimen	63
4.2	Experimental Setup and Procedure	66
4.3	Stiffness Determination of Non-perforated and Perforated Laminates	71
4.3.1	Gage Length Effect	71
4.3.2	Measured Stiffness of Non-perforated Laminates	76
4.3.3	Measured Stiffness of Perforated Laminates	79
4.4	Strength Determination of Non-perforated and Perforated Laminates	82
4.5	Determination of Inter-laminar Shear Strength	90
4.5.1	Standardized Shear Strength Evaluation	91

4.5.2	Finite Element Analysis	91
4.5.3	Experimental Procedures	93
4.5.4	Analytical and Experimental Results	95
5	Investigations of Perforated Laminates	104
5.1	Two-scale Analysis Strategy	104
5.2	Model Parameters	105
5.2.1	Unit Cell Geometry	105
5.3	Unit Cell Investigations of Uni-directional Laminates	108
5.3.1	Geometry of the Unit cell	108
5.3.2	Ply Material	108
5.3.3	Results	109
5.4	Investigations of Perforated Woven Fabric Laminates - Material System I .	118
5.4.1	Geometry of a Unit Cell	118
5.4.2	Ply Material	118
5.4.3	Results	118
5.4.4	Global Analyses	128
5.5	Investigations of Perforated Woven Fabric Laminates - Material System II	130
5.5.1	Geometry	130
5.5.2	Material Model	130
5.5.3	Stiffness Behavior of Perforated Laminates	131
5.5.4	Deformation Patterns	133
5.5.5	Failure of Perforated Laminates	134
5.5.6	Application of Two-Scale Modeling	140
5.6	Conclusion	145
	Bibliography	146

Chapter 1

Introduction

Composite materials are ideal for structural applications where high strength-to-weight and/or stiffness-to-weight ratios are required. Aircrafts and spacecrafts are typical weight-sensitive structures in which composite materials are utilized.

The study of composite materials actually involves many topics such as, for example, manufacturing processes, anisotropic elasticity, strength of anisotropic materials, and micro mechanics.

This thesis shows a finite element based two-scale analysis method for studying problems related to the mechanical behavior of perforated laminates under monotone static loading conditions.

1.1 Introduction to Composite Materials

Three basic questions must be addressed when composite materials are used:

1. The What - What is a composite material?
2. The Why - Why are composite materials used instead of homogeneous ones, e.g., metals?
3. The How - How are composite materials used in structural applications?

1.1.1 The What - What is a Composite Material?

The word composite in the term of composite materials signifies that two or more materials are combined. Composite materials have a long history of technical usage. For example, straw was used to strengthen mud bricks, or medieval swords and armor were constructed with different layers of different metals. More recently, fiber-reinforced resin-matrix composite materials have become important in weight sensitive applications such as aircraft and space vehicles.

Commonly accepted types of composite materials are:

1. Fibrous composite materials that consist of fibers (long or short fibers, specifically a randomly oriented, ...) in a matrix material (polymer, metal, ...)
2. Laminated composite materials that consist of layers (for example, layers are woven fabric plies, uni-directional plies, ...) of various materials
3. Particulate composite materials that are composed of particles in a matrix (SiC in metal matrix composites, gravel in concrete, ...)
4. Combinations of some or all of the first three types

This work focusses on laminated, long fiber reinforced, composite materials so called laminates. A laminate is a bonded stack of laminae (layers) with various orientations of the principal material directions as shown in FIGURE 1.1. The layers of the laminate are usually bonded together by the same matrix material that is used in the individual laminae. The lay-up follows from the required strength and stiffness in the given application.

1.1.2 The Why - Advantages of Fiber Reinforced Composite Materials

The current and the potential advantages of fiber reinforced composite materials are:

1. Strength and stiffness advantages
2. Weight advantages
3. Cost advantages

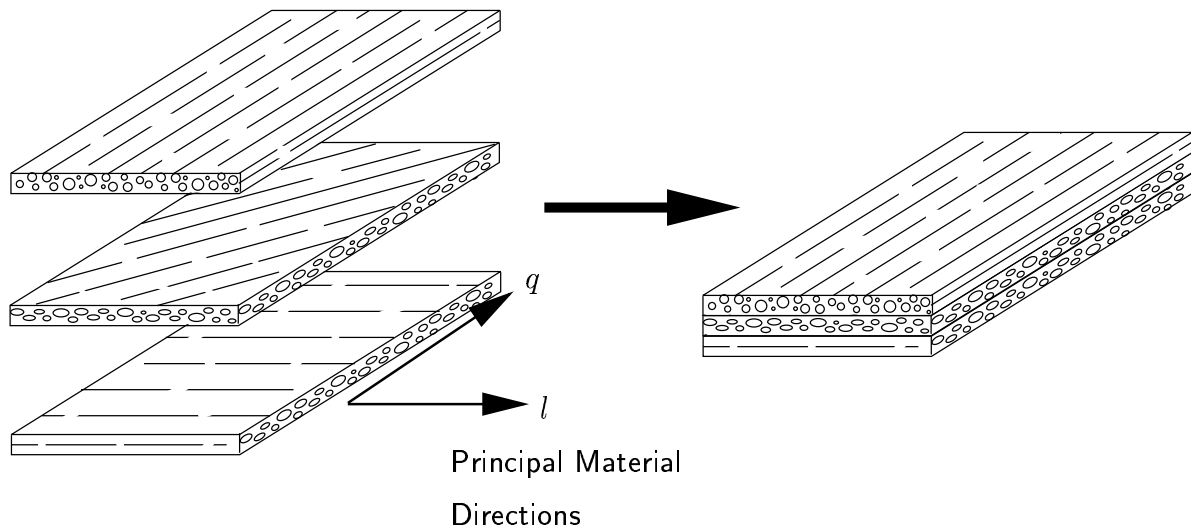


FIGURE 1.1: Unbonded (left) and bonded (right) view of a laminate construction

An example for the first two points are carbon fiber reinforced polymers (CFRP). They are up to three times stronger than as aluminum, a common aircraft structural material, yet weigh only 60% as much!

A graphical representation of the strength and stiffness of many materials on the basis of effectiveness per unit weight density is shown in FIGURE 1.2. The properties of common structural metals are denoted by open squares. Various forms of advanced composite materials are denoted by three kinds of open circles. Obviously, the most effective materials lie in the upper right corner. Fibers alone are stiffer and stronger than when placed in a matrix. However, in general fibers can not be used without a matrix. Also, unidirectional configurations are stiffer and stronger in fiber direction than in-plane isotropic configurations in either of the two directions. Laminates used in practice typically lie somewhere inbetween unidirectional and in-plane isotropic configurations. The metals each occupy only one point in FIGURE 1.2. Although metals show a low specific strength and stiffness they have the advantages of uniform in-plane (isotropic) properties.

Regarding the cost advantages, they can be split into initial costs (raw material, design, fabrication, assembly) and operating costs (operating, maintenance, salvage). Both cost parts are summarized as life-cycle cost. Often the initial costs are substantially higher but the operating costs, as well as the life-cycle cost, are lower for composite structures than for metallic structures.

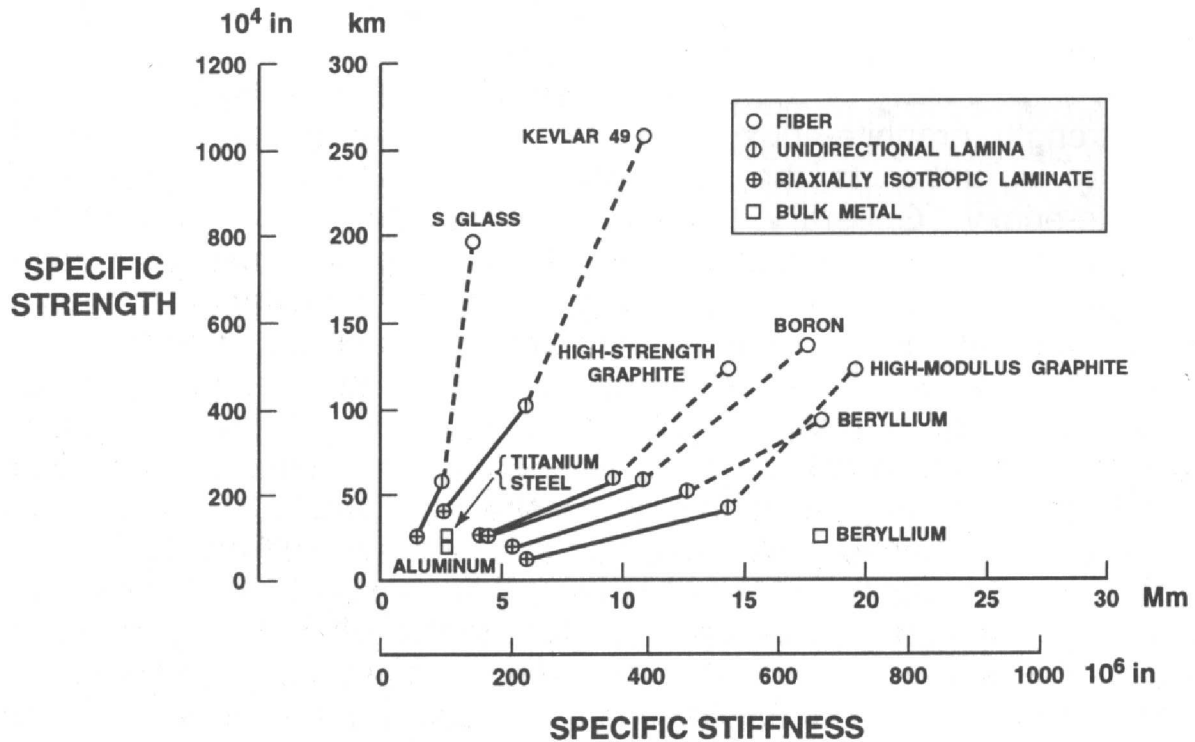


FIGURE 1.2: Specific strength and stiffness of composite materials and metals (from Jones [1999])

1.1.3 The How - Applications of Composite Materials

Currently, almost every company involved in aircraft design is developing products made of fiber-reinforced composite materials. Therefore, a variety of applications of composites are available, where one example - the blocker door - is described in the following.

Application Example: Blocker Door

FIGURE 1.3 (right) shows the blocker doors at the end of the bypass duct in a Rolls Royce Trent 500 engine. The left picture in FIGURE 1.3 shows how the blocker doors are placed around the bypass duct.

The operation of a blocker door is shown in FIGURE 1.4 for a better understanding of the mode of action. The two main states are the flight position, where the blocker doors mainly have to absorb sound (FIGURE 1.4 left). The second position is the thrust

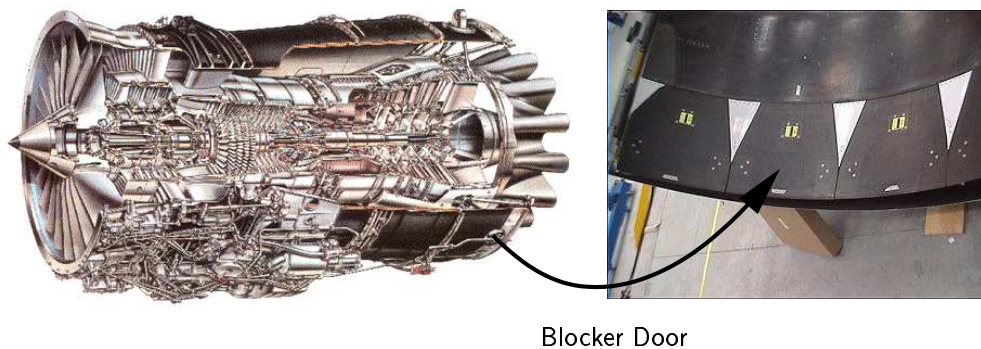


FIGURE 1.3: Mounted blocker door of a Rolls Royce Trent 500 engine (left) and unmounted view (Courtesy of FACC AG, Ried, Austria)

reverser mode (FIGURE 1.4 right), where the blocker doors have to move into the airflow and, therefore, mainly have to carry mechanical loads. That is, blocker doors have to be designed for absorbing sound and for carrying mechanical loads as well.



FIGURE 1.4: Operation of a blocker door. Flight position (left) and thrust reverser position after landing (right)

The structure of a blocker door mainly consists of a sandwich compound (see FIGURE 1.5) which is composed of an aluminum honeycomb core, a non-perforated carbon fiber reinforced skin at one side and a perforated carbon fiber reinforced skin at the other side. Earlier blocker door designs have been based on the idea that the non-perforated skin carries the loads, and the perforated skin acts only as “sound inlet” for the sound absorption, where the honeycomb cells operate as Helmholtz resonators. In later design concepts the perforated skin was more and more utilized to carry loads as well in order to save weight. One problem is, that no efficient numerical design methods were available and expensive material tests had to be performed to characterize the stiffness and strength of a perforated skin material. Even so, the behavior of the perforated

laminate within a structure could only be checked with material tests on the final structure. Therefore, a fast and accurate analysis tool for the design of structures containing perforated laminates was needed in order to save material and design cost, as well as weight. This thesis shows a finite element based two-scale analysis method for study-

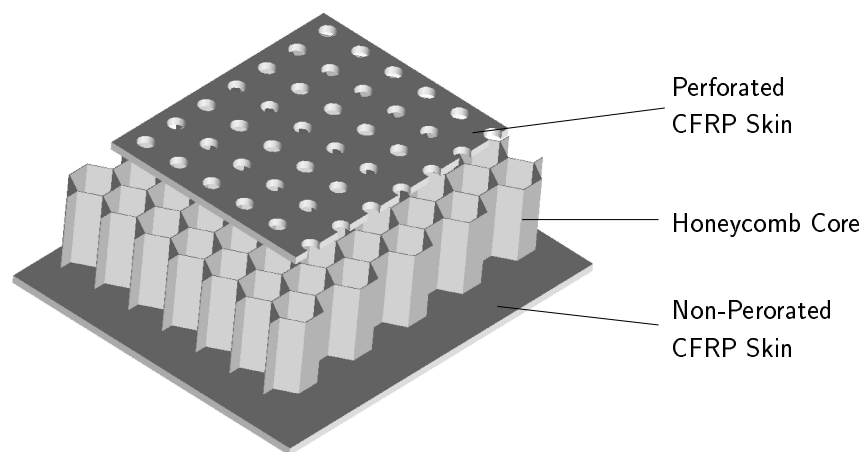


FIGURE 1.5: Parts of a blocker door sandwich compound

ing problems related to the mechanical behavior of perforated layered composites. Unit cell models and hierarchical meso-macro concepts are presented. Regarding the “effective first ply failure strength”, both inter- and intra-laminar failure, as well as free edge effects, are taken into account on the meso-level (ply level). Thus, the deformation and strength evaluation of structures containing perforated laminates can be performed simply on the structural (macroscopic) level.

Chapter 2

Literature Review

2.1 Failure and Damage of Layered Laminates

2.1.1 Overview

The presented failure and damage considerations are mainly based on the ideas of Puck (Puck [1996], Puck and Schürmann [1998]) and Ladevèze (Ladevèze [2001], Ladevèze and Lubineau [2002]).

The difference between failure and damage can be described as follows: If a laminate is loaded various failure processes happen within the plies. The sum of all failure processes up to a certain load level are called damage of the laminate at this load level. Usually, damage starts at the beginning of the loading, which might be during the cool down after curing. The failure processes can be split into characteristic failure modes: Fiber failure, inter-fiber failure, first ply failure, last ply failure, and ultimate failure. FIGURE 2.1 shows the characteristic failure modes. In addition the damage mechanisms and used damage/failure models during mechanical loading of a typical uni-directional multi-layered laminate are sketched.

At the beginning of loading initial damage exists in form of micro cracks. Increasing loads lead to the first single fiber cracks and/or growth of the micro matrix cracks up to the point where first ply failure appears. First ply failure means the failure of some thousand fibers (for example, a roving) or an inter-fiber failure, where a meso matrix crack runs completely through the thickness of one ply. After first ply failure micro and meso fiber/matrix damage progresses and degrades the stiffness of the damaged

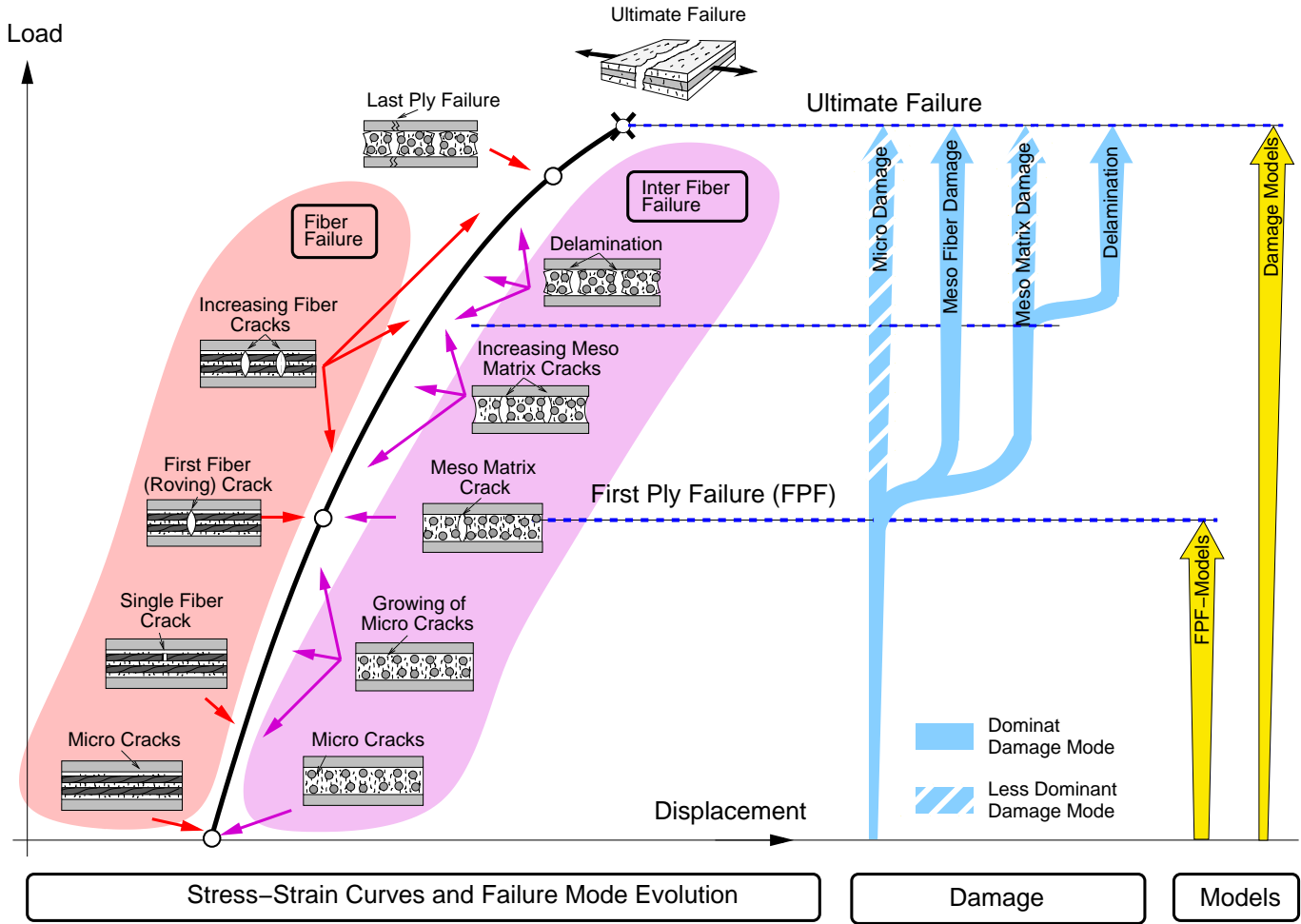


FIGURE 2.1: Characteristic failure modes, damage mechanisms, and damage/failure models during mechanical loading

ply. More and more cracks arise, and in the case of meso matrix cracks a new failure mode - delamination - becomes dominant before last ply failure appears. Last ply failure indicates a crack running completely through the thickness of the laminate. Thus, the whole laminate fractures (e.g., breaks into two or more parts) and the ultimate load is reached.

FIGURE 2.1 also shows the dominant damage mechanisms. First micro damage appears and becomes more and more a damage on the meso scale. With the exception of possible situations at the free edge delamination shows up very late in the load history. The reason for this is that in the case of an initially perfect laminate delamination must be initiated, e.g., by “crack initiation regions” such as crack tips from meso matrix cracks.

Finally, FIGURE 2.1 indicates the required numerical models for the investigation of damaged laminates. Universal tools are damage models which may be very complex in their formulation. Simpler tools are first ply failure models. They are suitable for predicting first ply failure only. Due to the fact that these models do not take damage into account, they are called failure models instead of damage models.

2.1.2 Detailed Descriptions of the Failure Modes

Characteristic failure modes in layered composites should be considered at different length scales. Failure modes at the micro scale are:

- Single fiber failure
- Micro matrix failure (micro matrix cracks)

Typical meso failure modes for layered laminates are:

- (Multiple) fiber failure
- Inter-fiber failure (fiber/matrix debonding, meso matrix cracking, delamination)

Both meso failure modes are denoted as first ply failure (FPF). Characteristic macro failure modes are:

- Last ply failure
- Ultimate failure

Fiber Failure

Basically fiber failure is the only “desired” failure mode of layered composites, because fibers are the “load carrying parts” of layered laminates. Ideally they should be loaded until their strength limit is reached and nothing else should rupture before.

Fiber failure means in general the fracture of some thousand fibers (e.g. a roving or tow) and not the fracture of single fibers.

Inter-fiber Failure

Puck [1996] distinguished between three different inter-fiber failure modes for in-plane loading (see FIGURE 2.2): Mode A, Mode B, and Mode C. Mode A means a fracture due to transverse tensile and shear stresses. Mode B fracture is caused by moderate transverse compression stresses and significant shear stresses. In the case of Mode C fracture is initiated by high transverse compression stresses and shear stresses. In the last case the hazard of an “explosion” of the laminate due to a wedge effect is very high if θ reaches a critical value, where θ is the inter-fiber fracture plane angle. For a detailed description of the Puck modes see Puck and Schürmann [1998].

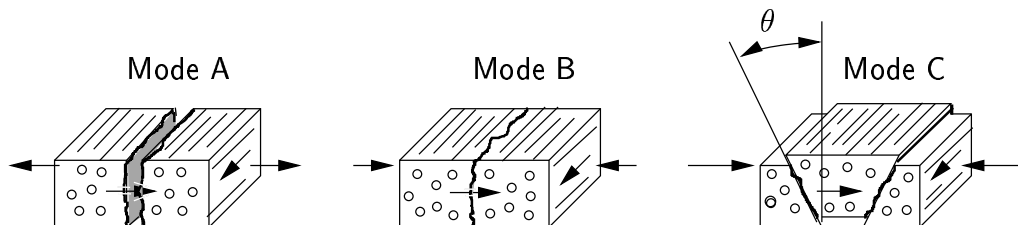


FIGURE 2.2: Sketch of Puck’s failure modes and inter-fiber fracture plane angle θ for in-plane loading (following Puck [1996])

According to Puck, inter-fiber failure summarizes three different failure types:

- Meso matrix cracking
- Fiber/matrix debonding
- Delamination

Fiber/Matrix Debonding

Fiber/matrix debonding means that the matrix material is separated from or along the fibers (fracture plane parallel to the fiber axis), respectively. In this work fiber/matrix debonding is an inter-fiber failure and is not considered separately.

Delamination

A further inter-fiber (inter-laminar) failure mode of laminated materials is the separation of individual layers which is denoted as delamination. This failure mode occurs between two adjacent layers and is a result of inter-laminar stresses. Near free edges a tri-axial stress state appears which might cause delamination (see Niederstadt [1985]). Another source of delamination are meso matrix cracks which also produces a tri-axial stress state at the crack tip.

Finally, it should be emphasized that in this thesis delamination is not considered as a separate failure mode. Delamination is treated just as a special case of inter-fiber failure, where the fracture angle is $\theta = 90^\circ$, however, an interface weakening faktor (f_{wI}) is introduced in the strength values (see Puck and Schürmann [1998]).

First Ply Failure

The load which leads to the first occurrence of intra-laminar failure (meso fiber cracks or meso matrix cracks, respectively) is defined as first ply failure (FPF) load. It is typical for monotonically increased loading of layered composite materials that first ply failure occurs long before ultimate failure occurs. For example, the FPF load can be determined experimentally by acoustic emission tests.

Last Ply Failure

The last ply failure (LPF) load is reached when all plies rupture at a certain position along a cross-section of a laminate. Due to the non-linear behavior of structures after the FPF, complex damage models are needed for the numerical treatment.

Ultimate Failure

The ultimate failure load is achieved when the structure ruptures completely and breaks into two or more parts. In the case of homogeneously loaded structures (for example, test specimens) the ultimate failure is identical to the last ply failure.

2.2 Failure Analysis of Laminates with Low Stress Gradients

With the exception of regions close to free edges the stresses within homogeneously loaded laminates can simply be obtained from Classical Lamination Theory (CLT). Introductions to the CLT are given in Jones [1999], Rammerstorfer and Böhm [1998], Niederstadt [1985]. The CLT is based on the assumptions of:

- Effective, linear elastic ply material behavior
- Kirchhoff's plate theory (linear strains along the thickness, neglectation of out-of-plane shear)

Thus, a set of relations is obtained which links the structural membrane forces (\underline{N}) and moments (\underline{M}) with the strains ($\underline{\bar{\epsilon}}$) and curvature changes ($\underline{\bar{\chi}}$) of a reference plane. The isothermal constitutive equation is given as:

$$\begin{pmatrix} \underline{N} \\ \underline{M} \end{pmatrix} = \begin{pmatrix} \underline{A} & \underline{B} \\ \underline{B} & \underline{D} \end{pmatrix} \begin{pmatrix} \underline{\bar{\epsilon}} \\ \underline{\bar{\chi}} \end{pmatrix}, \quad (2.1)$$

with the in-plane stiffness (\underline{A}), the bending stiffness (\underline{D}), and the coupling stiffness (\underline{B}). The local strains within a layer are computed from the strains and curvature changes of the reference plane, as well as from rotational transformations, and application of the ply material law gives the local ply stresses. If the stress fields show low gradients, and these stresses can be used for failure predictions in standard failure criteria (see Section 2.2.2).

2.2.1 Introduction to Failure Models

The used coordinate systems are shown in Section 3.1.1 (FIGURE 3.1). In the following the axes of the local material coordinate systems of individual layers are introduced as l

(in fiber direction), q (in-plane transverse fiber direction) and t (out-of-plane transverse fiber direction). The superscript “ m ” indicates the considered ply of the laminate. The axes of the unit cell coordinate system are denoted as 1, 2 and 3. The axes of the global coordinate system of the structure are defined as x , y and z .

Failure Criterion, Failure Condition:

Many different definitions are used for the notation “failure criterion” in the literature. In this work the failure criterion is defined as:

$$F({}^m\sigma_{ij}, {}^mR_{ij}) \begin{cases} \leq 1 & i \dots {}^ml, {}^mq, {}^mt \\ > 1 & j \dots {}^ml, {}^mq, {}^mt \end{cases} \quad m \dots \text{layer index.} \quad (2.2)$$

The failure criterion indicates if the stress state ${}^m\sigma_{ij}$ is endured ($<$) or leads just to failure of ply m ($=$ failure condition). Values of $F > 1$ indicates that failure has appeared and the calculated stresses are unrealistic. The strength values ${}^mR_{ij}$ characterize the first ply failure strength of the individual ply m , where in general a distinction is made between tensile and compressive strength values, denoted by superscripts or “+” and “-”, respectively.

Safety Factor and Risk Parameter

In order to assess the actual stress state ${}^m\sigma_{ij} = {}^m\sigma_{ij}^v + {}^m\sigma_{ij}^c$ with respect to the critical stress state ${}^m\sigma_{ij}^*$ a safety factor ${}^m\lambda$ for each individual layer/interface m is introduced. The superscript v denotes variable (load dependent) stresses, and the superscript c stands for constant (for example, residual) stresses. In this way, the failure condition $F = 1$ for each layer/interface can be written as

$$F({}^m\sigma_{ij}^*, {}^mR_{ij}) = F({}^m\lambda {}^m\sigma_{ij}^v + {}^m\sigma_{ij}^c, {}^mR_{ij}) = 1, \quad (2.3)$$

where ${}^mR_{ij}$ are the individual first failure strength values for the ply/interfaces m . FIGURE 2.3 shows a graphic explanation of the safety factor. It should be noted that in the following investigation the constant stress part ${}^m\sigma_{ij}^c$ is set to zero.

For a laminate consisting of n layers (denoted with the superscript m) and $n - 1$ interfaces (denoted with the superscript i) the safety factor of the laminate ${}^{\text{lam}}\lambda$ is given by

$${}^{\text{lam}}\lambda = \min_{n, n-1} ({}^m\lambda, {}^i\lambda), \quad (2.4)$$

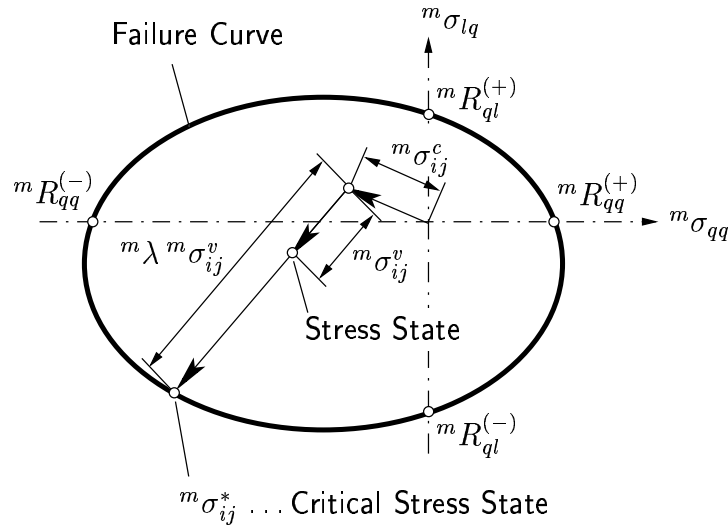


FIGURE 2.3: σ_{qq} - σ_{lq} failure curve (failure envelope) including the definition of the safety factor ${}^m\lambda$ for ply m

where the superscript i denotes the considered interface. The risk parameter of the laminate ${}^{\text{lam}}\mathcal{R}$, as defined by Puck [1996], is the reciprocal of the safety factor:

$${}^{\text{lam}}\mathcal{R} = \frac{1}{{}^{\text{lam}}\lambda} . \quad (2.5)$$

Note that the risk parameter and the failure index, which is defined as the sum of the left hand term of Equation (2.7) with $\lambda = 1$, are not the same. From a practical point of view, a risk parameter appears to be more meaningful than a failure index.

It should be mentioned that the definition of a risk parameter does not make sense in the presence of substantial constant stress contributions, because for stress states close to the failure surface the risk parameter may be very low while the actual effort of the laminate is very high.

Failure Surface, Failure Curve

A safety factor ${}^{\text{lam}}\lambda$ is based on a stress state ${}^m\sigma_{ij}^*$, where the stresses come from mechanical or hygro-thermal loading of the laminate. If the safety factor is calculated for all possible mechanical in-plane loading combinations of the membrane forces N_{ij} , then the failure surface can be plotted in the N_{11} - N_{22} - N_{12} space, building up the failure surface for the laminate with ${}^{\text{lam}}\lambda \equiv 1$. A plane cut through the failure surface gives a

failure curve (failure envelope). Usually, the cutting plane is spanned by two membrane forces and the third membrane force is set to zero, an example being, a N_{11} - N_{22} failure curve where $N_{12} = 0$. Failure curves for a uni-directional laminate are shown in FIGURE 2.4 and FIGURE 2.5 for standard failure hypotheses, which are described in the following.

2.2.2 Failure Hypotheses for Low Stress Gradients

The failure function $F({}^m\sigma_{ij}, {}^mR_{ij})$ (Equation (2.2)) can be described by using several failure hypotheses:

- Limit theories (maximum stress, maximum strain, ...)
- Tensor polynomial theories (Tsai-Wu, Tsai-Hill, ...)
- Strain energy theories (Ladevèze, ...)
- Direct mode determining theories (Puck, ...).

The failure hypotheses used in this work are:

- The maximum stress criterion (Jones [1999]) for fiber failure
- The 3D Tsai-Wu criterion (Tsai and Wu [1971]) for matrix failure
- A quadratic criterion (Brewer and Lagace [1988]) for delamination
- The 3D Puck criterion (Puck [1996], Puck and Schürmann [1998]) for all failure modes

The Tsai-Wu criterion is used, because it is of more general character than the Tsai-Hill or Hoffmann failure criteria (see Jones [1999]).

All the above failure criteria try to fit the experimental results essentially with curve fitting parameters. The simplest criterion is the maximum stress criterion and the most sophisticated one is the 3D Puck criterion. A comparison of all applied failure theories is shown in FIGURE 2.4 and FIGURE 2.5. In FIGURE 2.4 the overestimation of the strength by the Tsai-Wu criterion as compared with the maximum stress criterion,

especially for $N_{22} < 0$, becomes evident. The maximum stress criterion usually overestimates the strength for biaxial loading. Therefore, a combination of the Tsai-Wu and maximum stress criterion is reasonable. The failure envelopes look qualitatively the same for the combined Tsai-Wu – maximum stress criterion and the Puck criterion. In FIGURE 2.5 the Puck and the Tsai-Wu criteria are very similar. The above mentioned overestimation and also an underestimation of the maximum stress criterion can be seen. The underestimation comes mainly from the fact that transverse compression stresses increase the resistance against shear stresses.

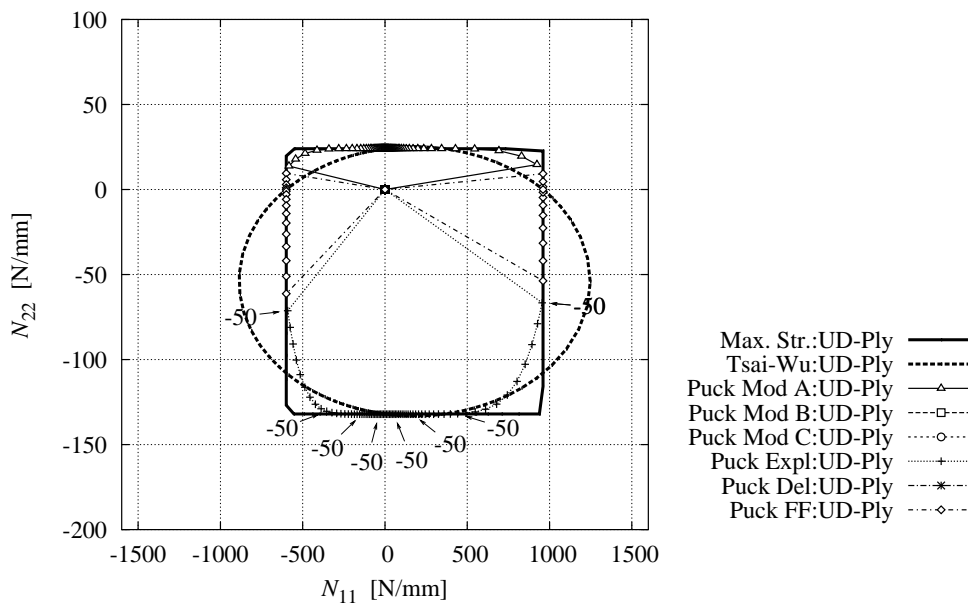


FIGURE 2.4: $N_{11} - N_{22}$ failure curves of all applied failure theories for a uni-directional [0/0/0] CFRP. The numbers along the Puck failure curves are the inter-fiber fracture angles θ .

Tsai-Wu Failure Hypothesis

The Tsai-Wu failure criterion was introduced in the seventies of the last century. At this time tensor polynomial failure theories were used to describe ductile fracture. Tsai and Wu applied a modified tensor polynomial failure criterion - the Tsai-Wu criterion - to describe the failure of layered laminates. Although it was known that brittle fracture is responsible for failure of layered laminates. Nevertheless, the Tsai Wu criterion is widely used, especially for the prediction of matrix failure.

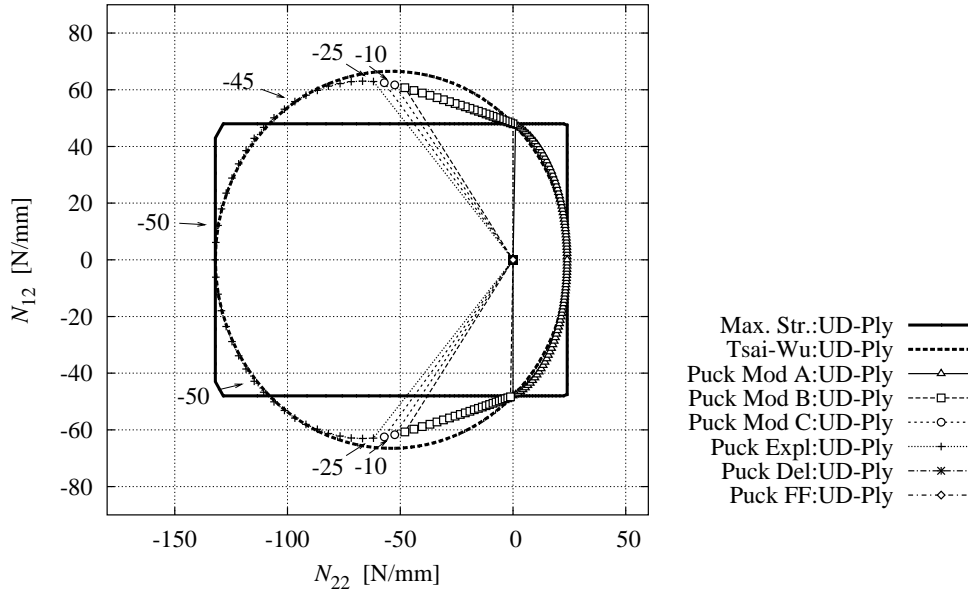


FIGURE 2.5: $N_{22} - N_{12}$ failure curves of all applied failure theories for a uni-directional $[0/0/0]$ CFRP. The numbers along the Puck failure curves are the inter-fiber fracture angles θ .

The Tsai-Wu failure condition for the individual layer m is defined in tensorial form as:

$${}^m \lambda F_{rs} {}^m \sigma_{rs} + {}^m \lambda^2 F_{rsuv} {}^m \sigma_{rs} {}^m \sigma_{uv} = 1 \quad r, s, u, v = l, q, t, \quad (2.6)$$

where ${}^m \sigma_{rs}$ stands for the actual stress state of the m -th ply, and the product ${}^m \lambda {}^m \sigma_{rs}$ leads to the critical stress state ${}^m \sigma_{rs}^*$. The extended form of the Tsai-Wu failure condition is given by (the index m is not written in the following):

$$\lambda (F_{ll} \sigma_{ll} + F_{qq} \sigma_{qq} + F_{tt} \sigma_{tt}) + \lambda^2 (2F_{llqq} \sigma_{ll} \sigma_{qq} + 2F_{lltt} \sigma_{ll} \sigma_{tt} + 2F_{qqtt} \sigma_{qq} \sigma_{tt} + F_{llll} \sigma_{ll}^2 + F_{qqqq} \sigma_{qq}^2 + F_{tttt} \sigma_{tt}^2 + F_{qtqt} \sigma_{qt}^2 + F_{ltlt} \sigma_{lt}^2 + F_{lqlq} \sigma_{lq}^2) = 1, \quad (2.7)$$

where

$$\begin{aligned} F_{ll} &= \frac{1}{R_{ll}^{(+)}} - \frac{1}{R_{ll}^{(-)}} & F_{llll} &= \frac{1}{R_{ll}^{(+)} R_{ll}^{(-)}} & F_{qtqt} &= \frac{1}{R_{qt}^{(+)} R_{qt}^{(-)}} & F_{llqq} &= K \sqrt{F_{llll} F_{qqqq}} \\ F_{qq} &= \frac{1}{R_{qq}^{(+)}} - \frac{1}{R_{qq}^{(-)}} & F_{qqqq} &= \frac{1}{R_{qq}^{(+)} R_{qq}^{(-)}} & F_{tttt} &= \frac{1}{R_{tt}^{(+)} R_{tt}^{(-)}} & F_{qqtt} &= K \sqrt{F_{qqqq} F_{tttt}} \\ F_{tt} &= \frac{1}{R_{tt}^{(+)}} - \frac{1}{R_{tt}^{(-)}} & F_{tttt} &= \frac{1}{R_{tt}^{(+)} R_{tt}^{(-)}} & F_{qlql} &= \frac{1}{R_{ql}^{(+)} R_{ql}^{(-)}} & F_{lltt} &= K \sqrt{F_{llll} F_{tttt}} \end{aligned}$$

with positive values for all $R_{ij}^{(-)}$. In Equation (2.7) some interaction terms are neglected (see Tsai and Wu [1971]). The shear strengths in the above equation are often assumed to be independent of the loading direction ($R_{qt}^{(+)} = R_{qt}^{(-)}$), $R_{tl}^{(+)} = R_{tl}^{(-)}$ and $R_{ql}^{(+)} = R_{ql}^{(-)}$. Furthermore, it should be mentioned that the shear strengths R_{tl} and R_{ql} are denoted with tl and ql instead of lt and lq , because usually $R_{ql} < R_{lq}$ and $R_{tl} < R_{lt}$, respectively.

One fitting parameter of the Tsai-Wu failure condition is the interaction parameter K . The bounds of this parameter are obtained from energy considerations, because the magnitudes of the interaction terms F_{llqq} , F_{qqtt} and F_{lltt} are constrained. For example, in the case of F_{llqq} the following inequality must hold:

$$F_{lll}F_{qqqq} - F_{llqq}^2 \geq 0 \quad \Rightarrow \quad -K \sqrt{F_{lll}F_{qqqq}} \leq F_{llqq} \leq +K \sqrt{F_{lll}F_{qqqq}} \quad (2.8)$$

and based on this inequality K must lie between $[-1, 1]$. Some values used in the literature for K are listed in TABLE 2.1.

TABLE 2.1: Multiplier in the interaction terms (interaction parameter)

K	Reference
-0.5	Skrna-Jakl [1994]
0.0	Jones [1999]

To show the influence of the interaction term the Tsai-Wu failure curves are plotted for several values of K ($-0.5, 0, +0.5$) and displayed in FIGURE 2.6. A strong influence of K can be seen, which is less important, if the Tsai-Wu criterion is used in combination with, e.g., the maximum stress criterion and the minimum safety factor of both theories is used.

For the calculation of the safety factor ${}^m\lambda$ Equation (2.7) is split into linear terms $\sum L$ and quadratic terms $\sum Q$ and the failure condition can then be rewritten as:

$${}^m\lambda^2 \sum Q + {}^m\lambda \sum L - 1 = 0.$$

The solution of this quadratic equation follows as (only ${}^m\lambda > 0$ is physically meaningful):

$${}^m\lambda = \frac{1}{2\sum Q} \left(-\sum L + \sqrt{(\sum L)^2 + 4\sum Q} \right) \quad (2.9)$$

and ${}^m\lambda$ is obtained.

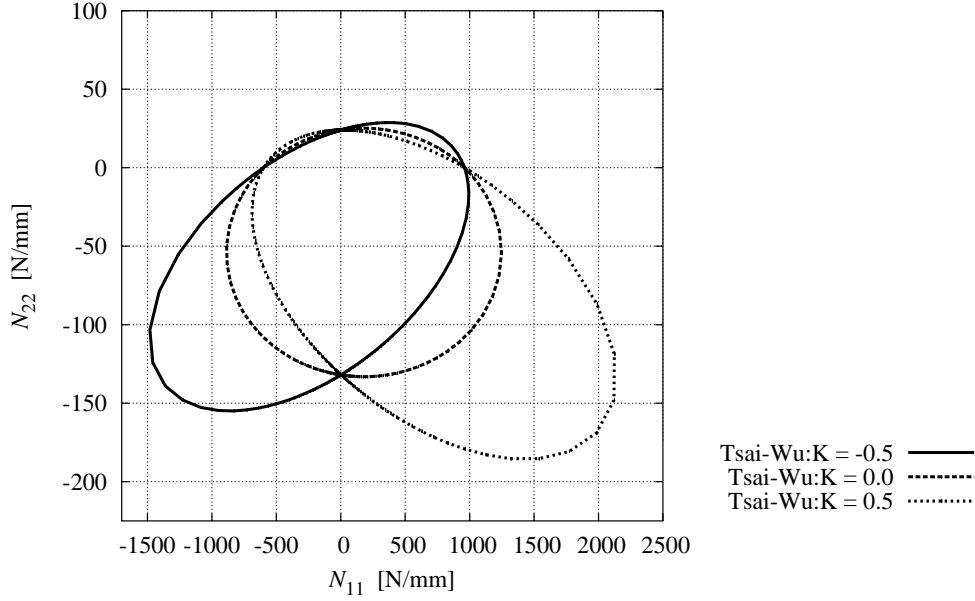


FIGURE 2.6: Comparison of the Tsai-Wu failure curves for different interaction parameters $K = -0.5, 0, +0.5$

Maximum Stress Failure Hypothesis

The maximum stress failure condition is the simplest failure criterion, and can be written for a considered ply m in the tensile/compressive directions (denoted with “ (\pm) ”) as:

$$\frac{{}^m\lambda |{}^m\sigma_{ll}|}{{R_{ll}^{(\pm)}}} = 1 \quad \frac{{}^m\lambda |{}^m\sigma_{qq}|}{{R_{qq}^{(\pm)}}} = 1 \quad \frac{{}^m\lambda |{}^m\sigma_{tt}|}{{R_{tt}^{(\pm)}}} = 1 \quad (2.10)$$

and in the shear directions as

$$\frac{{}^m\lambda |{}^m\sigma_{lq}|}{{R_{ql}}} = 1 \quad \frac{{}^m\lambda |{}^m\sigma_{lt}|}{{R_{tl}}} = 1 \quad \frac{{}^m\lambda |{}^m\sigma_{qt}|}{{R_{qt}}} = 1 \quad (2.11)$$

Herein, all stresses are defined in the local material coordinate systems. The critical safety factor is defined as the smallest safety factor obtained from one of the 9 Equations (2.10)-(2.11). In this work the maximum stress failure hypothesis is mainly used to predict fiber failure.

Quadratic Delamination Failure Hypothesis

Delamination is caused by inter-laminar stresses. These stresses act within the interface i of two adjacent layers (m and $m + 1$). For predicting the onset of delamination, the following failure condition proposed by Brewer and Lagace [1988] is applied:

$$\frac{({}^i\lambda \ {}^i\sigma_{31})^2}{(R_{31}^{IL})^2} + \frac{({}^i\lambda \ {}^i\sigma_{32})^2}{(R_{32}^{IL})^2} + \frac{({}^i\lambda \ {}^i\sigma_{33})^2}{(R_{33}^{IL})^2} = 1 \quad \sigma_{33} > 0. \quad (2.12)$$

This failure condition is based on the assumptions that delamination is only affected by stress components σ_{i3} and is understood as a failure process which happens within an inter-phase of vanishing thickness, i.e. an interface. Furthermore, this quadratic delamination failure hypothesis is based on the assumption that only transverse normal stresses σ_{33} have an influence on failure only if they are tensile stresses ($\sigma_{33} > 0$). If it is assumed that the strength values for delamination are independent of the fiber directions of adjacent layers, that is, $R_{31}^{IL} = R_{32}^{IL}$ (see Puck [1996]), then the stresses or strengths may be defined in an arbitrary coordinate system, where the third axis coincides with the local 3-axis which is normal to the reference plane of the laminate.

Due to the fabrication process (dirt, fat on the interface, etc.) the inter-laminar shear strength is in general smaller than the intra-laminar (inter-fiber) shear strength and is indicated with superscript "IL". The inter-laminar strength values can also be obtained from the intra-laminar strength values by introducing an interface weakening factor f_{wI} (see Puck [1996]):

$$R_{31}^{IL} = f_{wI} R_{tl} \quad R_{32}^{IL} = f_{wI} R_{qt} \quad R_{33}^{IL} = f_{wI} R_{tt}^{(+)} . \quad (2.13)$$

If the two shear strength values are not equal ($R_{31}^{IL} \neq R_{32}^{IL}$) an alternative approach is needed. A way, which is similar to Puck's ideas, is to introduce two safety factors ${}^m\lambda$ and ${}^{m+1}\lambda$, where m and $m + 1$ are two plies with an interface i in-between. The unknown safety factors are obtained from:

$$\frac{1}{m\lambda} = \sqrt{\frac{({}^m\sigma_{tt})^2}{(f_{wI} R_{tl})^2} + \frac{({}^m\sigma_{qt})^2}{(f_{wI} R_{qt})^2} + \frac{({}^m\sigma_{tt})^2}{(f_{wI} R_{tt}^{(+)})^2}} \quad {}^m\sigma_{tt} > 0 \quad (2.14)$$

and

$$\frac{1}{{}^{m+1}\lambda} = \sqrt{\frac{({}^{m+1}\sigma_{tt})^2}{(f_{wI} R_{tl})^2} + \frac{({}^{m+1}\sigma_{qt})^2}{(f_{wI} R_{qt})^2} + \frac{({}^{m+1}\sigma_{tt})^2}{(f_{wI} R_{tt}^{(+)})^2}} \quad {}^{m+1}\sigma_{tt} > 0. \quad (2.15)$$

Finally, the interface safety factor ${}^i\lambda$ is obtained from:

$${}^i\lambda = \min({}^m\lambda, {}^{m+1}\lambda) . \quad (2.16)$$

This delamination evaluation procedure can also be applied with other failure criteria where Equation (2.14) and Equation (2.15) are, e.g., replaced accordingly by the Tsai-Wu failure criterion (Equation (2.7)).

Referring to this the experimental determination of the inter-laminar shear strength R_{31}^{II} , R_{32}^{II} and the inter-laminar tensile strength R_{33}^{II} must be stated to be rather problematic, and in fact the experimental determination of the inter-laminar shear strength ILSS may show a difference between those obtained from two different ILS-test methods of more than 100% (see Section 4.5 or Pahr et al. [2002]).

Puck Failure Hypothesis

The Puck criterion is a physically based failure criterion for inter-fiber fracture (failure) of uni-directional fiber reinforced laminates. A combination of the criterion with the maximum stress criterion in l -direction allows the prediction of fiber failure, too.

Puck presented some different models for plane stress states (2D) and for fully tri-axial (3D) stress states. The 2D model is mentioned in Section 2.1.2, where different failure modes appear for different loading cases.

In this work the last presented 3D model (Puck [1996], Puck and Schürmann [1998], Juhasz et al. [2001]) is used. The model is based on following hypotheses:

1. A fiber reinforced layered laminate has different failure modes: fiber failure (FF) and inter-fiber failure (IFF). Both are of different nature and require, therefore, different failure criteria.
2. The failure of the matrix material can be looked upon as brittle and Mohr's fracture hypothesis can be applied, that is, the fracture limit of a brittle material is governed by the stresses in the fracture plane.
3. IFF always occurs on a plane parallel to the fibers. On such planes typically no fiber fracture occurs.
4. Inter-fiber fracture is caused by a normal stress σ_n and shear stresses $\tau_{nt'}$ and τ_{nl} in the fracture plane (FIGURE 2.7). Therefore, an IFF criterion is formulated using stresses and strengths with respect to the fracture plane.

5. If $\sigma_n \geq 0$, then IFF will be caused by the simultaneously acting transverse tensile stress σ_n and the transverse shear stresses $\tau_{nt'}$ and τ_{nl} in the fracture plane.
6. If $\sigma_n < 0$, then the transverse compressive stress σ_n normal to the fracture plane generates an additional resistance against fracture caused by the transverse shear stresses $\tau_{nt'}$ and τ_{nl} .

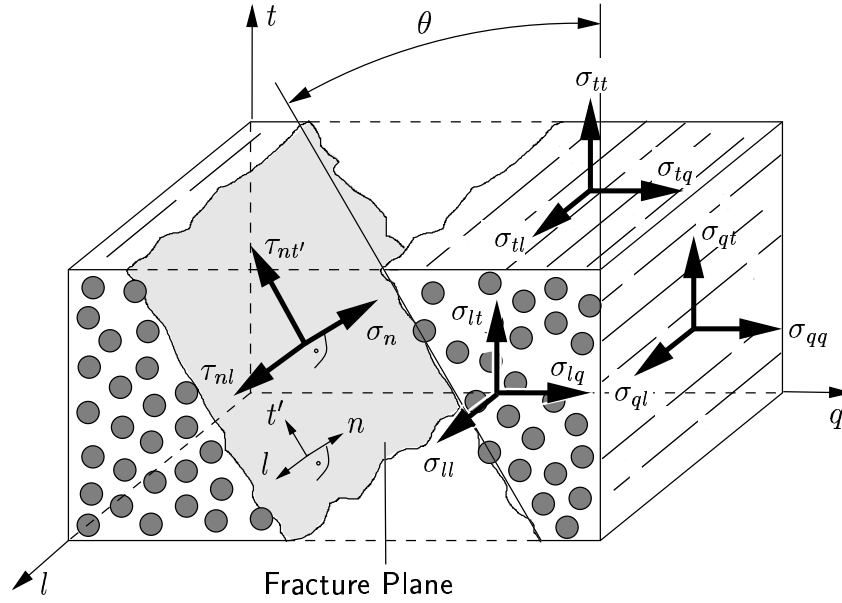


FIGURE 2.7: Components of the stress tensor and stresses in the fracture plane of a unidirectional ply element

The stresses within the fracture plane (see FIGURE 2.7) are calculated from the ply stresses in the material coordinate system as

$$\begin{aligned}
 \sigma_n(\theta) &= \sigma_{qq} \cos^2 \theta + \sigma_{tt} \sin^2 \theta + 2 \sigma_{qt} \sin \theta \cos \theta & (2.17) \\
 \tau_{nt'}(\theta) &= -\sigma_{qq} \sin \theta \cos \theta + \sigma_{tt} \sin \theta \cos \theta + \sigma_{qt} (\cos^2 \theta - \sin^2 \theta) \\
 \tau_{nl}(\theta) &= \sigma_{lt} \sin \theta + \sigma_{lq} \cos \theta
 \end{aligned}$$

and depend on the fracture angle θ (note the difference of the t and t' direction).

Based on these stresses, the fracture plane angle dependent risk parameter $\mathcal{R}(\theta)$ can be written as:

Transverse Tension: $\sigma_n \geq 0$

$$\mathcal{R}(\theta) = \frac{1}{\lambda(\theta)} = \sqrt{\left(\frac{1}{R_{qq}^{(+)} - \frac{p_{q\psi}^{(+)}(\theta)}{R_{q\psi}^A(\theta)}}\right)^2 \sigma_n(\theta)^2 + \left(\frac{\tau_{nt'}(\theta)}{R_{qt}^A}\right)^2 + \left(\frac{\tau_{nl}(\theta)}{R_{ql}}\right)^2 + \frac{p_{q\psi}^{(+)}(\theta)}{R_{q\psi}^A(\theta)} \sigma_n(\theta)} = 1 \quad (2.18)$$

Transverse Compression: $\sigma_n < 0$ (with parabolic compression stress influence)

$$\mathcal{R}(\theta) = \frac{1}{\lambda(\theta)} = \sqrt{\left(\frac{\tau_{nt'}(\theta)}{R_{qt}^A}\right)^2 + \left(\frac{\tau_{nl}(\theta)}{R_{ql}}\right)^2 + \left(\frac{p_{q\psi}^{(-)}(\theta)}{R_{q\psi}^A(\theta)} \sigma_n(\theta)\right)^2 + \frac{p_{q\psi}^{(-)}(\theta)}{R_{q\psi}^A(\theta)} \sigma_n(\theta)} = 1 \quad (2.19)$$

An overview of all Puck notations is given in FIGURE 2.8. Two new notations are the gradients of the fracture body $p_{qt}^{(\pm)}$, $p_{ql}^{(\pm)}$, and $p_{q\psi}^{(\pm)}$ for $\sigma_n = 0$, as well as the strengths of the fracture plane $R_{qq}^{A(+)} = R_{qq}^{(+)}$, $R_{ql}^A = R_{ql}$, R_{qt}^A , and $R_{q\psi}^A$ (indicated by the superscript “A”). As mentioned before the failure criterion is based on Mohr’s fracture hypothesis, which leads to a closed failure surface for $\sigma_n > 0$ and an open failure surface for $\sigma_n < 0$ (see FIGURE 2.8). This failure surface is, compared to other failure criteria, not defined in an l, q, t ply material coordinate system. It is defined in the fracture plane with a normal vector n_i and looks, therefore, different to other failure surfaces.

Further explanations on Mohr’s fracture body are given in FIGURE 2.9. There, a plane $\sigma_n - \tau_{nt'}$ section through the above fracture body is shown. At first attention is given to the determination of R_{qt}^A . Therefore, $R_{qq}^{(-)}$ is needed from a uni-axial compression test (dash dotted Mohr circle). Next the gradient $p_{qt}^{(-)}$ from the fracture body can be obtained from experiments or taken from the literature (Puck et al. [2002]). The strength of the fracture plane R_{qt}^A can then be calculated from the equation:

$$R_{qt}^A = \frac{R_{qq}^{(-)}}{2(1 + p_{qt}^{(-)})}. \quad (2.20)$$

FIGURE 2.9 shows further how the fracture plane angle can be obtained from a stress state σ_{tt}^* , σ_{qq}^* , σ_{qt}^* . This stress state is denoted as “Point A” on the solid Mohr circle (note the negative shear stress sign on the vertical axis). The stress state is assumed to be a critical stress state. First the stresses are transformed onto the principal axes leading to the stress state σ_1^* , σ_2^* (“Point B”). Next the point on the fracture curve (“Point C”) is found and the rotation angle β , as well as the critical stress state in the fracture plane σ_n^* and $\tau_{nt'}^*$, are obtained. Finally, the fracture plane angle is obtained from $\theta = \beta - (-\alpha)$.

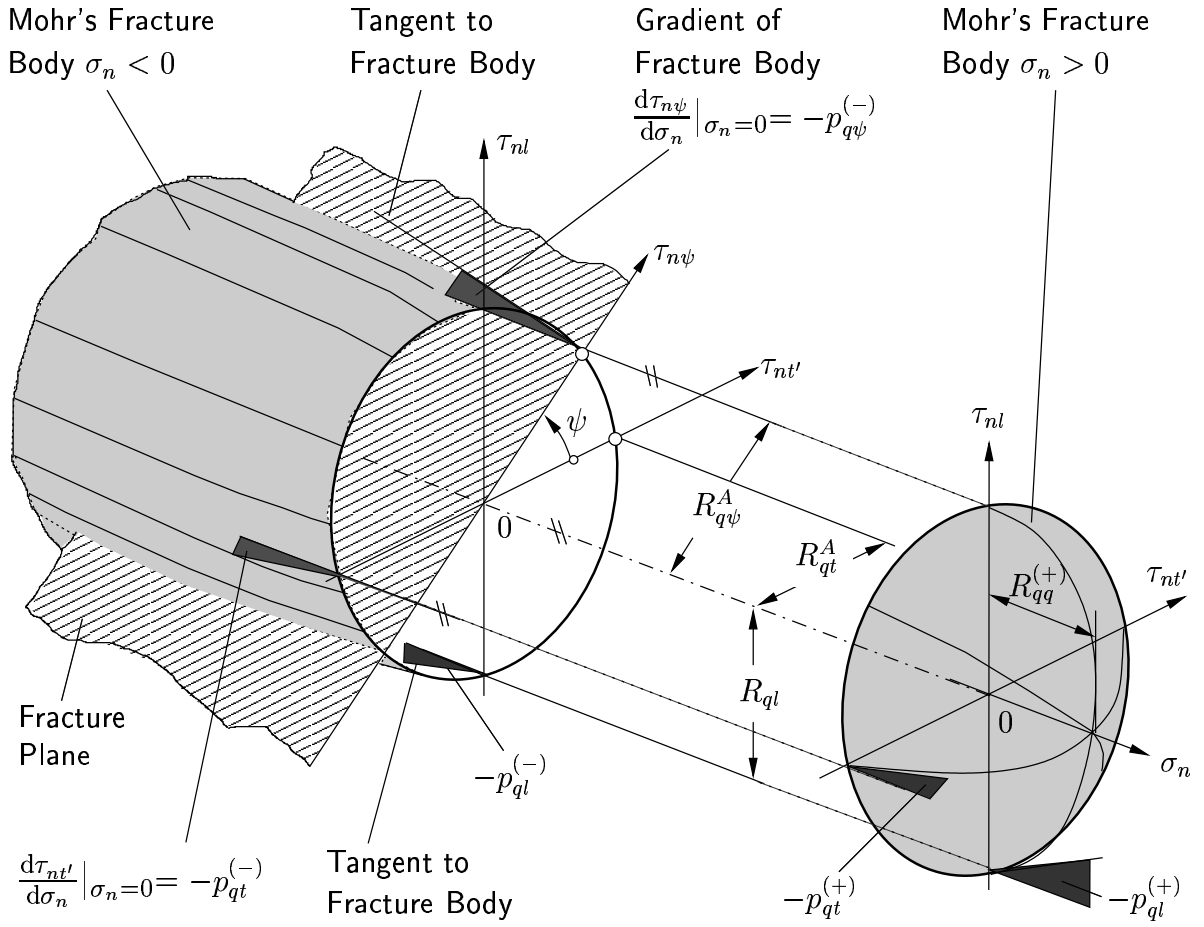


FIGURE 2.8: Mohr's fracture bodies for $\sigma_n \leq 0$ and Puck's notations

Coming back to Equation (2.18) and Equation (2.19) the ratios $\frac{p_{q\psi}^{(+)}(\theta)}{R_{q\psi}^A(\theta)}$ and $\frac{p_{q\psi}^{(-)}(\theta)}{R_{q\psi}^A(\theta)}$ are computed from the interpolation

$$\frac{p_{q\psi}^{(\pm)}(\theta)}{R_{q\psi}^A(\theta)} = \frac{p_{qt}^{(\pm)}}{R_{qt}^A} \cos^2 \psi(\theta) + \frac{p_{ql}^{(\pm)}}{R_{ql}} \sin^2 \psi(\theta) \quad \text{with} \quad \psi = \arctan \frac{\tau_{nl}(\theta)}{\tau_{nt'}(\theta)}, \quad (2.21)$$

where $p_{qt}^{(\pm)}$ are two additional material parameters, which can also be found in Puck et al. [2002].

The computed safety factor in Equation (2.18) or Equation (2.19) is a function of θ , i.e., $\lambda = \lambda(\theta)$. The relevant safety factor ${}^m\lambda$ of one ply is finally obtained from:

$${}^m\lambda = \min_{\theta} (\lambda(\theta)), \quad (2.22)$$

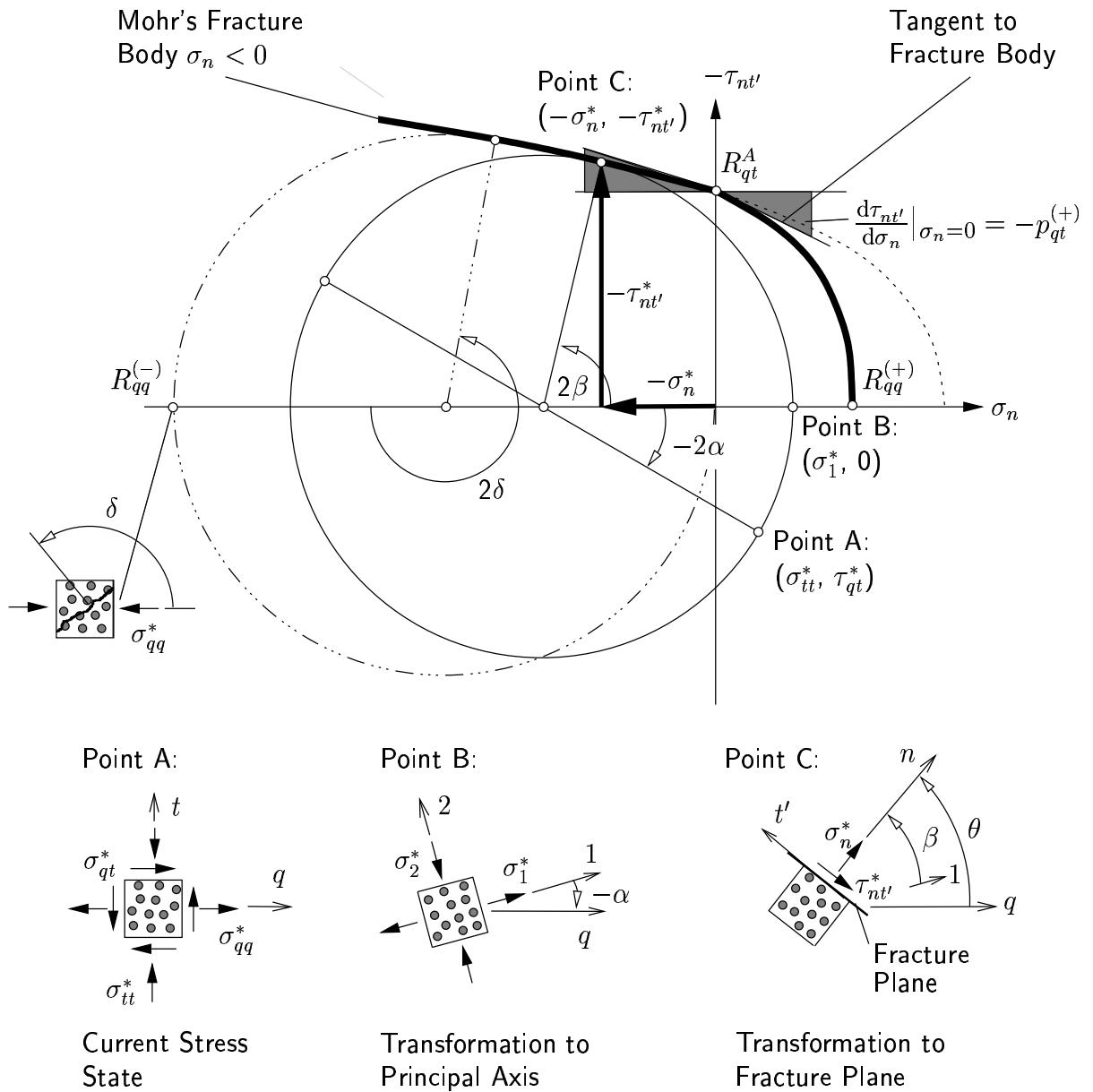


FIGURE 2.9: Determination of the strength of the fracture plane R_{qt}^A and the fracture angle θ using Mohr's circle and Mohr's fracture bodies in a $\sigma_n - \tau_{nt'}$ plane

and an iterative solution procedure is required. The critical fracture plane angle $\theta = \theta_{fp}$ is also obtained from Equation (2.22).

The above failure conditions are based on zero longitudinal stresses ($\sigma_{ll} = 0$). Additional longitudinal stresses scale, in the case of zero constant stress parts, the failure

conditions Equation (2.18) and Equation (2.19) but do not change the fracture plane angle θ_{fp} . The scaling function (weakening factor f_{wl}) is introduced as:

$$f_{wl} = 1 - \left(\left| \frac{m\lambda \sigma_{ll}}{\sigma_{ld}} \right| \right)^k, \quad (2.23)$$

where $\sigma_{ld} = 1.1 R_{ll}^{(\pm)}$ and $k = 6 \dots 8$ are suggested in Puck [1996]. The failure conditions F_i (Equation (2.18) and Equation (2.19)) can then be rewritten by using the longitudinal stress weakening factor f_{wl} as:

$$\frac{1}{f_{wl}(m\lambda \sigma_n, \dots)} F_i(m\lambda \sigma_n, m\lambda \tau_{nt}, m\lambda \tau_{nl}, \dots) = 1 \quad i = \text{Mode A, B, C}. \quad (2.24)$$

The problem of Equation (2.24) is that $m\lambda$ can not be computed explicitly and a second iterative solution procedure is needed to obtain the relevant safety factor $m\lambda$ of one ply.

Finally, it should be mentioned that Puck suggests to use his inter-fiber failure conditions (Equation (2.24)) in combination with the maximum stress criterion in l -direction in order to describe fiber failure, and the additional failure condition for fiber failure reads:

$$\frac{m\lambda |\sigma_{ll}|}{R_{ll}^{(\pm)}} = 1. \quad (2.25)$$

2.2.3 Remarks on the Modeling of Layered Laminates Composed of Woven Fabric Layers

A woven fabric layer typically contains fibers (or rovings) in longitudinal and in-plane transverse direction. From this it becomes obvious that a single woven fabric ply can approximately be modeled as two UD-layers (0/90)¹.

The first problem arising with this modeling strategy is the right choice of material parameters for the equivalent UD-layers. For such cases test results are only available for laminates composed of woven fabrics. The material parameters for the UD-layers are then chosen such that the overall stiffness behavior of the woven fabric ply is obtained. With this assumption a sensitivity study on the local stress distributions, for example, around a hole can be performed. This approach is useful for stiffness and stress analysis.

¹Puck [1996] suggested that a woven fabric layer should be separated in more than two UD-layers.

When performing a failure analysis the problem of unknown strength parameters of the UD-layer model appears. The determination of these values is not as straightforward as the determination of the stiffness material parameters and a more sophisticated approach is needed. Furthermore, an equivalent UD layer model does not take geometrically non-linear effects due to roving stretching and bending (see Section 4.3.2) into account.

2.3 Failure Analyses of Laminates with High Stress Gradients

Perforated laminates are typical laminates with high stress gradients within a ply, where the stress gradients come mainly from:

1. The free edge effect around the open hole
2. The geometry effect of the hole

The first goal is to calculate the stress fields accurately. In a second step the original or modified stress values are then used in appropriate failure criteria.

2.3.1 Free Edge Effect

Homogeneously loaded thin layered laminates show a plane stress state inside a ply, where $\sigma_{zz} = \sigma_{zx} = \sigma_{zy} = 0$. Near free edges a tri-axial stress state with high gradients may be present which can lead to the well known free edge delaminations (Jones [1999]). The reasons for these tri-axial stress states are:

1. The Poisson number mismatch of adjacent plies (see Rose and Herakovich [1993])
2. The shear coupling mismatch of adjacent plies (see Niederstadt [1985], Stiftinger [1996])

Both effects are shown in FIGURE 2.10 which are results of detailed FE-analyses. There, the figures on the left side show the deformation of the plies without any coupling between the layers (unbonded), and the figures on the right side show perfectly

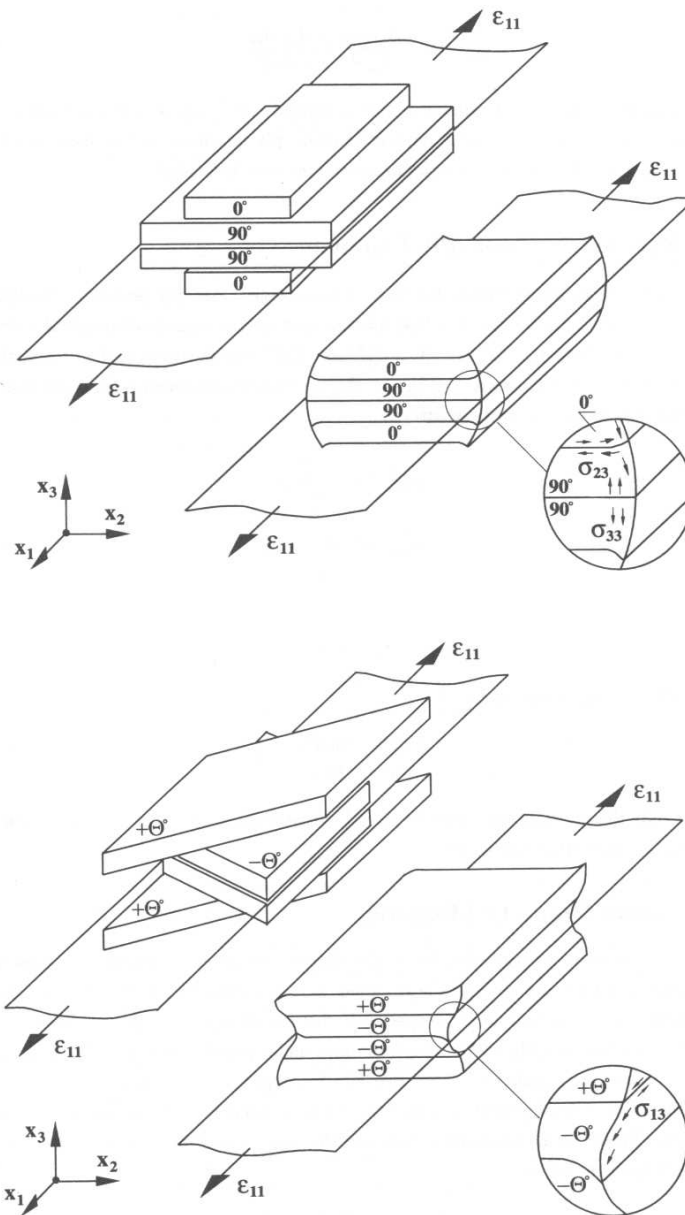


FIGURE 2.10: Free edge effect due to the Poisson number mismatch (top, for a $[0/90/90/0]$ laminate) and the shear coupling mismatch (bottom, for a $[\theta/-\theta/-\theta/\theta]$ laminate) taken from Stiffinger [1996].

bonded layers. Due to the bonding between the plies these mismatches produce additional normal and shear stresses, whereas high inter-laminar stresses are obtained in the region of the free edge.

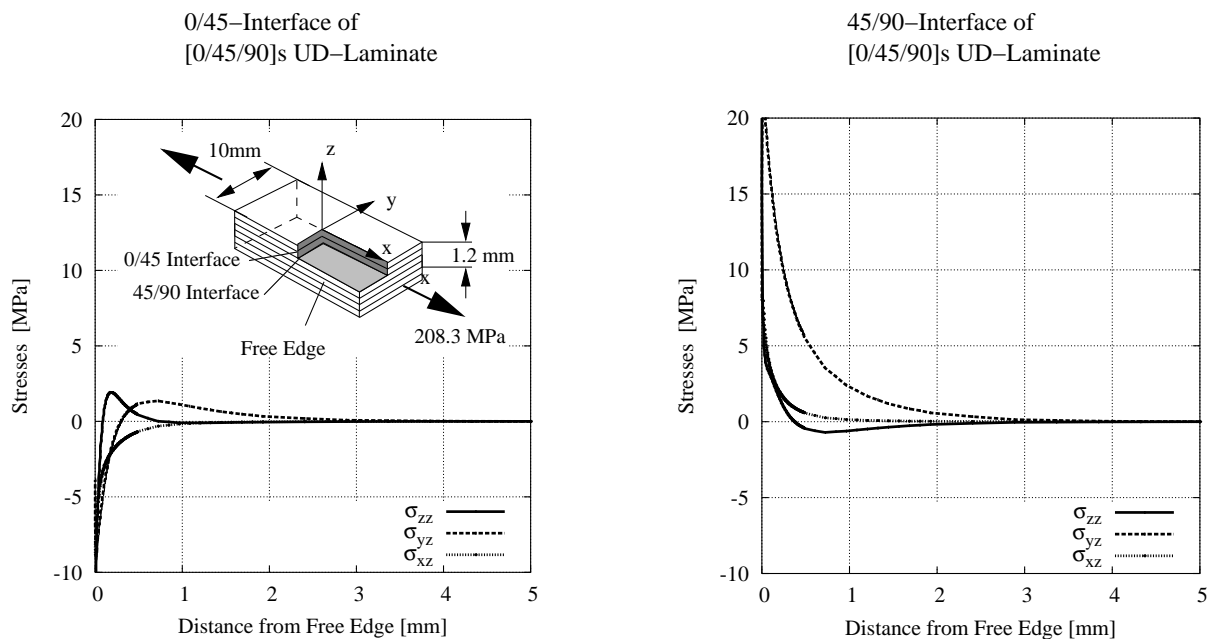


FIGURE 2.11: Stress distribution at the $0^\circ/45^\circ$ and $45^\circ/90^\circ$ interfaces of a $[0/45/90]_S$ UD laminate

As an example the free edge stresses are computed for a $[0/45/90]_S$ UD laminate (see FIGURE 2.11). The free edge effect also influences the in-plane stress components (not shown in FIGURE 2.11) due to the equilibrium equations, which additionally affects the failure behavior.

2.3.2 Geometry Effect of a Hole

The analytical solution for the stress concentration in the vicinity of a circular hole of an isotropic homogeneous plate was first given by Kirsch [1898]. FIGURE 2.12 shows the stress concentration around a circular hole in a plate of finite width and length. The plate was homogeneously loaded with a nominal stress of 100 MPa. The highest stress concentration appears at the region of the smallest cross sectional area normal to the loading direction at the free edge of the hole and has, in this example, a value of approximately 320 MPa, which leads to a stress concentration factor of 3.2.

In the case of laminates this effect is more pronounced due to the fact that some ply

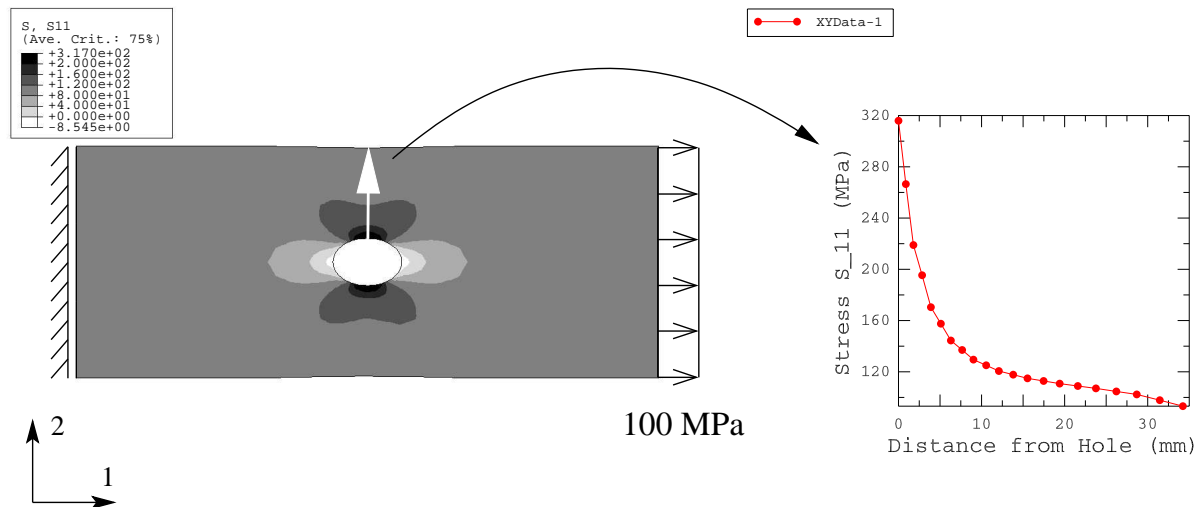


FIGURE 2.12: Tensile stresses σ_{11} in a homogeneously loaded plate containing a hole (left), and stress distribution along a line from the hole (right)

stresses are usually higher than the applied nominal stresses². Furthermore, the above mentioned free edge effect and the stress concentration around the hole are superimposed. This fact makes a hole within a laminate to a failure critical region.

2.3.3 Computation of Concentrated Stresses within Perforated Laminates

Many methods have been developed for the stress analysis of composite structures containing curvilinear free edges such as cutouts, holes, etc. They can be split into two kinds of models:

1. Analytical models describing the stresses within a ply with analytical equations for each stress component
 2. Numerical models based on finite element methods, boundary element methods,
- ...

²In the case of laminates the in-plane nominal stress is defined as the ratio of the membrane force divided by the laminate thickness

The first analytical models started with 2D considerations by Lekhnitskii [1936] who calculated stresses within an infinite plate containing an elliptical hole. These studies were followed by various applications and extensions. In further works it was tried to eliminate the limitation of infinity, as it was done by Xiao and Bathias [1993] in the so-called border collocation method. All the mentioned models are based on 2D considerations. Iarve and Pagano [2001] presented a method of the superposition of a hybrid (stress and displacement) approximation to provide an accurate stress field for a perforated multi-layered composite laminate. However this model was based on specific boundary conditions.

Numerical models play a more and more important role in the calculation of the stress fields of laminates with high stress gradients. Mostly standard finite element methods are used, where only some investigations are based on 3D finite element models (see Ng et al. [2000], Ng et al. [2001]). One of the additional advantages of numerical models is that they can easily take into account complex boundary conditions. One drawback, of course, is that standard finite elements do not explicitly account for stress singularities. When performing an FE-analysis with standard elements, it is important to investigate if the solution behaves in a consistent and reliable manner near singularities and if sufficiently accurate stress distributions, close to the singularity, can be obtained by a progressive mesh refinement. Analyses done by Whitcomb et al. [1982] lead to the conclusion that, provided the mesh is fine enough, a finite element analysis near stress singularities yields reliable stress distributions everywhere except in the two elements closest to the stress singularity. With these restrictions in mind standard FE-analyses are appropriate for calculating inter-laminar stresses in perforated layered composites.

2.3.4 Failure Models for Laminates with High Stress Gradients

Numerous failure models have been developed for strength prediction in perforated laminates. Overviews are given in Chu and Sun [1993] and Ng et al. [2000]. These models can be classified as three types: (1) Fracture mechanics models. (2) Stress based fracture models. (3) Progressive failure models.

Fracture Mechanics Models

This method can be regarded as an equivalent crack method in which a crack is assumed to represent an initial flaw or to describe damage progression in the perforated laminate. However, also an initial crack length must be assumed and because the form of damage is quite different from that of an ideal crack, such a representation is questionable. Fracture mechanics parameters such as stress intensity factor and strain energy release rate are generally used as curve fitting parameters.

Progressive Failure Models

Progressive failure models try to describe the damage process from the start of loading up to ultimate load. In the framework of this thesis the degradation models of Puck (Puck [1996], Puck et al. [2002]) and Ladevèze (Ladevèze [2001], Ladevèze and Lubineau [2002]) appear to be the most interesting ones. Both models introduce a failure mode dependent ply stiffness degradation, where Puck uses an inter-fiber failure density dependent stiffness degradation function and Ladevèze applies experimentally obtained “damage forces”, based on strain energy densities, to describe the degradation process. These models can be implemented, for example, in finite element procedures to study the damage of perforated laminates (see Pahr et al. [2003]).

At present progressive failure models have the drawback of very long computation times. Therefore, they are hardly used for investigations of partly perforated structures at this time.

Stress Based Fracture Models - Average and Point Stress Model

As mentioned above meso-mechanically based free edge investigations of laminated composites with different lay-up angles lead to singular macroscopic (effective) stress fields close to the intersection point of the interface and the free surface. Thus failure criteria for low stress gradients cannot be used directly to predict failure at the interface by using the original singular stress field.

It was argued, for instance in Chimani [1998], that the use of homogenized material description is not applicable for micro heterogeneous layered materials close to this intersection point. Chimani [1998], e.g., used a micro-mechanics approach to show that the meso-mechanically derived stress singularities disappear when the inhomogeneous

micro-structure (fiber, matrix) of the composite is accounted for explicitly. These findings justify the use of modified (appropriately averaged) mesoscopic stress values for the assessment of failure close to the free edge.

These kinds of stress based fracture models for perforated laminates, which used modified stress values, were first proposed by Withney and Nuismer [1974]. Two criteria predicting the “notched strength” of composite laminates containing circular holes were formulated and named the “Point Stress Criterion” (PSC) and the “Average Stress Criterion” (ASC). Both criteria assume that failure occurs when a designated local stress (point or average stress) at some characteristic distance away from the free edge is equal to the ultimate stress of a non-perforated laminate (see FIGURE 2.13).

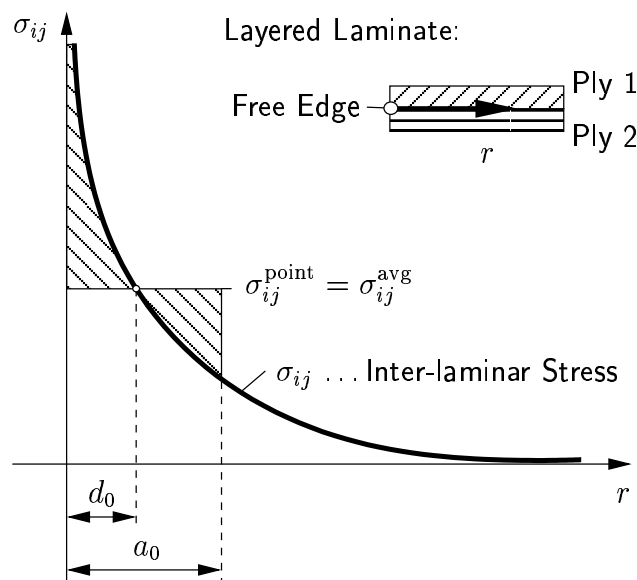


FIGURE 2.13: Evaluation of the average and point stresses from a given stress state σ_{ij}

The characteristic distances are denoted as d_0 (PSC) and a_0 (ASC), respectively. The obtained stress values are then used in failure conditions described in Section 2.2 (Tsai-Wu, maximum stress, delamination, and Puck). Consequently, key parameters in these models are d_0 and a_0 , respectively. Withney and Nuismer, as well as many other authors, assumed that the characteristic distance is a material constant and can be determined by a few material tests in conjunction with stress analyses of the perforated laminate. Many other researchers have shown that the characteristic distance is not just a material constant. Moreover, published values for a_0 vary from 0.2 mm up to 4 mm for nearly

the same notched laminate. This very confusing situation regarding the characteristic distance becomes clearer if the following model quality checks are made:

1. Is a ply by ply failure analysis (at least based on classical lamination theory) performed?
2. Is the location of failure initiation and failure propagation predicted in advance and fixed during the analysis or is the location updated during the analysis?
3. Are the notched strength data based on first ply failure tests or ultimate failure tests, that means, is the material nonlinearity taken into account in the latter case?
4. What kind of numerical models are used - 2D or 3D models?

Regarding item (1): Models without a ply by ply failure analysis are inaccurate and not considered here.

Regarding item (2): A good model to start with is Tan's minimum strength model (Tan [1988a], Tan [1988b]) where the notched strength is calculated in the individual plies at distances d_0 or a_0 around the hole and by this way the critical region is detected. Good agreement between numerical and experimental results was found. Another model proposed by Tan is the effective strength model which uses a fixed characteristic distance. This model should only be applied if the crack initiation location is known in advance. One drawback of Tan's models is that they predict ultimate failure without taking the material nonlinearity into account.

Regarding item (3): Xiao and Bathias [1993] modified Tan's minimum strength model with respect to material nonlinearity. They introduced a ply stiffness degradation after failure initiation up to the calculation of the ultimate notched strength where the stiffness degradation is assumed to be constant within one ply and was done by a simple reduction of terms in the ply stiffness matrix. The stress distribution was recalculated and the characteristic distance was determined for every critical ply by a fitting iteration process with experimental data. Although the degradation procedure appears to be over-simplified, the obtained results showed a better agreement with the experiments than the original Tan results.

Regarding item (4): Neither Tan nor Xiao and Bathias investigated 3D models in order to take free edge effects into account which have a strong impact on the stress field at the failure initiation location. Numerical models which fulfill all the above requirements can hardly be found when perforated laminates are considered. Chu and

Sun [1993] took the free edge effect into account in his semi-numerical investigations. Therefore the study presented here intends to overcome the drawback of 2D models by studying the problem of perforated laminates with detailed 3D finite element models on the meso-scale (ply level). It should also be mentioned that periodic hole arrangements are studied for which no analytical stress field solutions are available.

To summarize this literature review on stress based fracture models, the findings regarding to the influencing factors on the characteristic distances d_0 and a_0 , respectively, are:

- The individual strength parameters of the ply material/interface material
- The local stress field (which includes the failure mode dependency)

The influence of the strength parameters makes the characteristic distance material dependent where the second influence should be split into two parts. On the one hand the calculated stresses are affected by the geometry, the lay-up, the FE-model (2D, 3D) etc. In order to see if these have an impact on the characteristic distance the stress fields have to be computed as accurately as possible (including free edge stresses) and compared with suitable experiments where other influence factors are canceled out. On the other hand the influence of the failure mode depends also on the stress state and appropriate failure mode determining theories (e.g., Puck criterion) are needed to investigate the failure mode influence on the characteristic distance.

Finally, it can be said that the treatment of failure of laminates with high stress gradients is not satisfying at this time, and many open questions have to be answered.

2.4 Introduction to the Acoustic Emission Technique

As described in Section 2.1.1, the first important meso failure mode in a structure is first ply failure, because up to this point the material behaves approximately in a linear elastic way. In that case the stresses can be computed from simple linear models, and standard failure hypotheses can be applied. Therefore, it is important to know the first ply failure strength values. These characteristic strength values are determined experimentally by using the acoustic emission technique.

As the acoustic emission technique is a well known testing method a short introduction is presented in the following. When materials undergo certain deformations, tran-

sient elastic waves are generated by the spontaneous release of elastic energy from localized sources within the material. The process of wave generation and the waves themselves are defined as acoustic emission (Bassim [1990], Spanner et al. [1990], Wolters [1989]). Each rapid release of elastic energy is defined as an acoustic emission event. Sources of acoustic emission include many different mechanisms of deformation and fracture. As far as polymer composite materials are concerned, matrix cracking, debonding and fracture of the fibers, as well as delamination, are the major sources of acoustic emissions (McBride et al. [1990]). The basic idea of acoustic emission testing is to detect and monitor the transient waves released by the acoustic emission events, to use their waveform parameters to identify the sources and to evaluate their significance.

2.4.1 Schematic Test Setup

FIGURE 2.14 shows a typical test setup which is used for acoustic emission testing. In order to measure one or more of these waves, sensors are attached to the surface of the test object. They detect the mechanical movement at the surface when the acoustic emission wavefront impinges on the surface and convert it to a specific useable electric signal. The sensors used for acoustic emission testing generally utilize piezoelectric transducers as the electromechanical conversion device (Eitzen and Breckenridge [1990]). The electric signal received from the transducer is amplified and filtered in the pre-amplifier and transmitted to the mainframe of the acoustic emission monitoring system. There, the main amplification is performed and the waveform parameters of the signal are extracted. A PC is used for the processing and display of the signal data derived from the mainframe.

2.4.2 Acoustic Emission Signals - Events

Acoustic emission events appearing in polymer matrix composites are discrete signals - bursts - produced by local changes in the material (fiber or matrix cracking). A typical event is shown in FIGURE 2.15. These types of signals usually rise rapidly to the maximum amplitude and decay nearly exponentially to the level of the background noise. A threshold detection level is introduced to avoid spurious signals due to background noise. In order to characterize the acoustic emission signal the following waveform parameters are defined: Peak amplitude, rise time and event duration (see FIGURE 2.15).

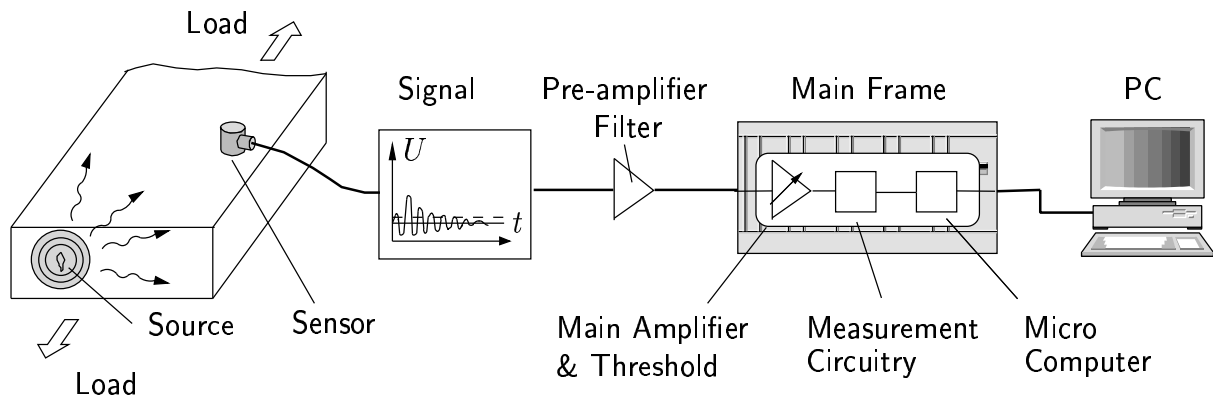


FIGURE 2.14: Acoustic emission test setup

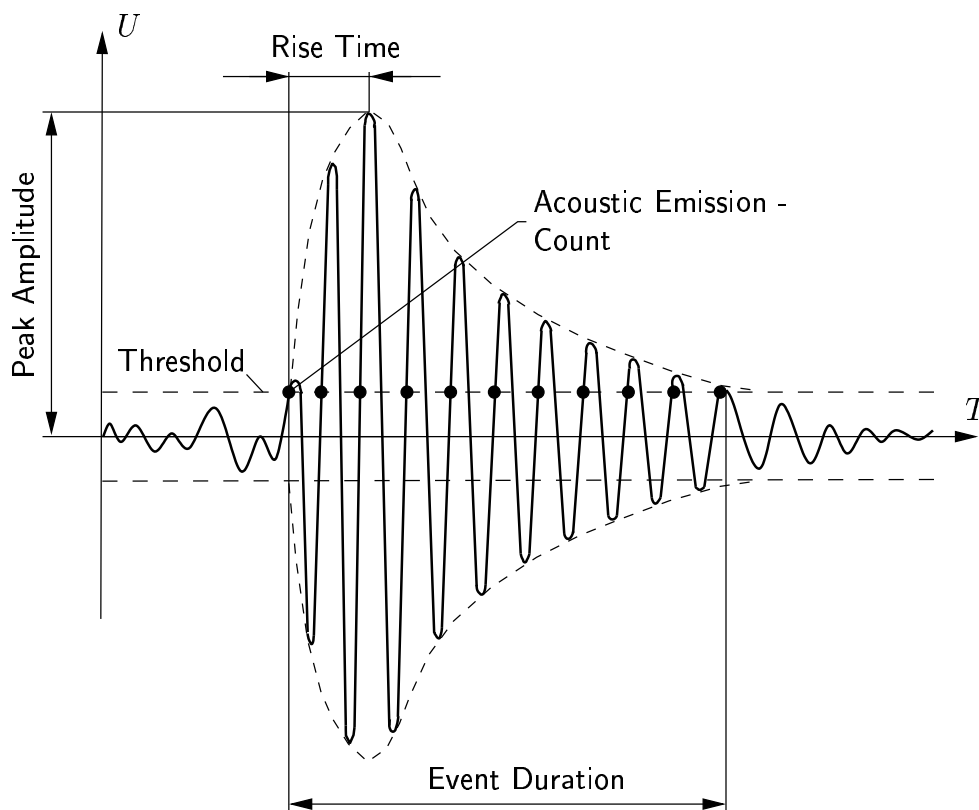


FIGURE 2.15: Characterization of an acoustic emission event

All of these parameters provide a measure for the intensity of the acoustic emission event. Since the acoustic emission activity is attributed to the rapid release of energy in the material, the energy content of the acoustic emission signal can be related to this

energy release. The electrical energy E_N of the signal is defined as

$$E_N = \frac{1}{R_E} \int_0^{D_E} U^2(T) dT \quad (2.26)$$

where R_E is the electrical resistance of the measuring circuit, D_E is the event duration (see Wolters [1989]), and U is the sensor voltage. Therefore, the measured electrical energy corresponding to the acoustic emission event represents a parameter for characterizing the acoustic emission source. One problem of this characterization is that the acoustic signal has an intensity loss of about 3-6 dB/cm, depending on the material. Therefore, the location of the acoustic emission source has to be known, and the signal has to be corrected accordingly. In practice this correction can hardly be done for anisotropic multi-layered laminates due to problems with the source location (see Section 2.4.3).

2.4.3 Linear Source Location Technique

In general one sensor is sufficient for the detection of events. The problem may be that the events appear in a region which is not of interest (for example, tab regions, load introduction points, supports, etc.). Therefore, besides the failure initiation, the location of the acoustic emission source is of major interest. A practical way for locating the source of an acoustic emission event is the time difference measurement technique. This technique can be used for source location in either one, two or three dimensions (Baron and S.P. [1990]). As a source location in one dimension will be sufficient for the investigated test specimen, only the linear source location technique is discussed in the following.

FIGURE 2.16 shows a typical test setup for the linear location of acoustic emission sources with two sensors attached to the specimen. If an acoustic emission event occurs, the measured time difference ($\Delta T = T_2 - T_1$) between the arrival of the elastic wave at the first sensor (sensor #1 in FIGURE 2.16) and the second sensor, is used to determine the location of the source (L_c) as:

$$L_c = \frac{1}{2}(D - \Delta T v) , \quad (2.27)$$

where v is the wave velocity, and D is the distance of the sensors. ΔT in Equation (2.27) is negative if the event reaches sensor #2 first ($T_1 > T_2$). If the source is not situated between the sensors, i.e., $\Delta T > \frac{D}{v}$, the event is disregarded. Thus, the failure information

is obtained on a straight line between the sensors (see FIGURE 2.17). There, the failure location is plotted in an event history plot at two different times during the loading process, e.g, 60 s and 75 s, after the start of the test.

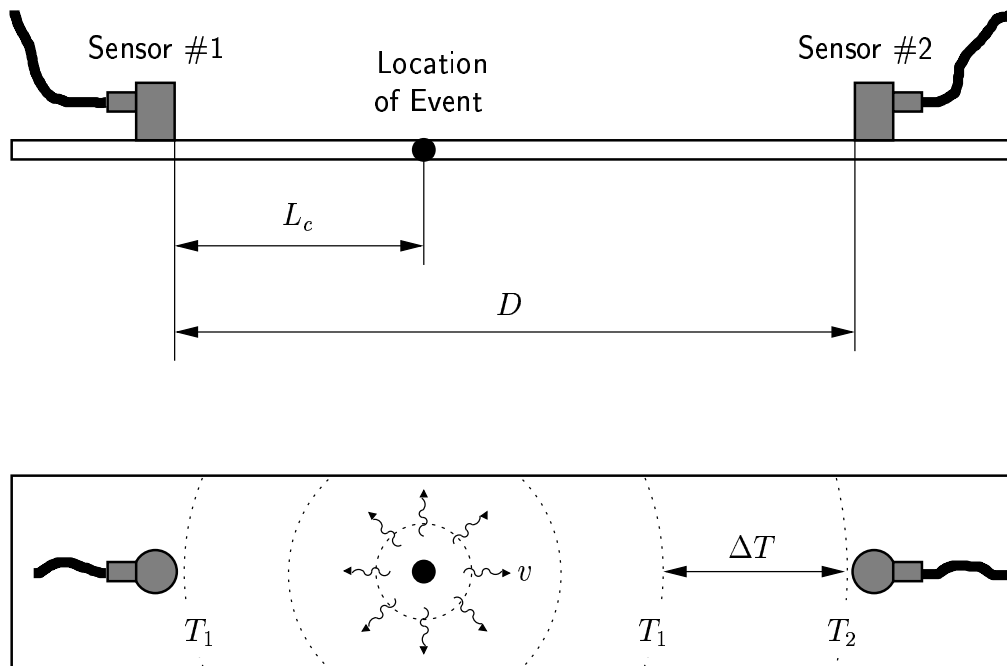


FIGURE 2.16: Linear time difference technique

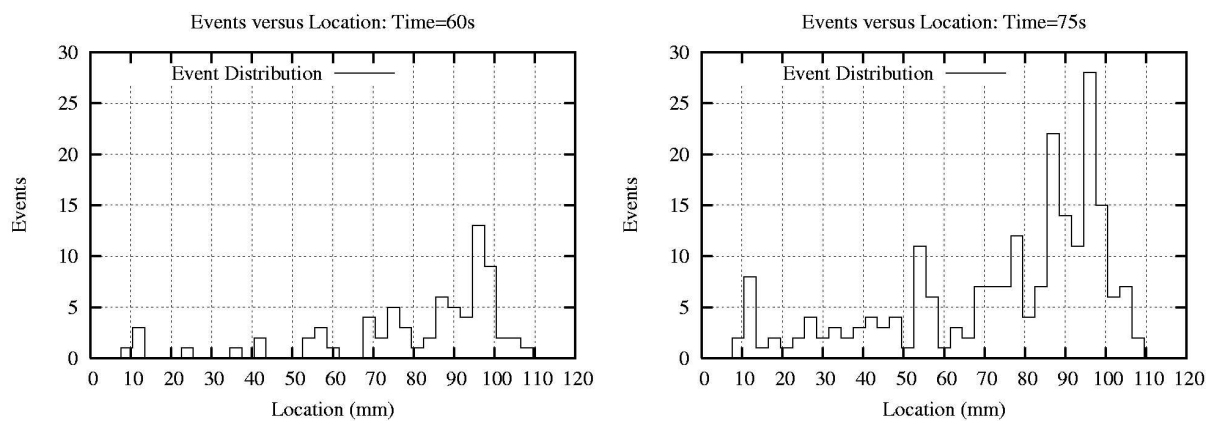


FIGURE 2.17: Event count versus event location for a 30 mm width, [0/0/0] CFR woven fabric laminate at two different time steps

The linear source location technique is appropriate, when the sensor separation is large compared to the width of the test specimen. However, if this is not the case and the linear location technique is used, then the obtained test results may contain considerable errors. FIGURE 2.18 shows a coupon with a low ratio of sensor separation to specimen width. The most important error sources can be summarized as:

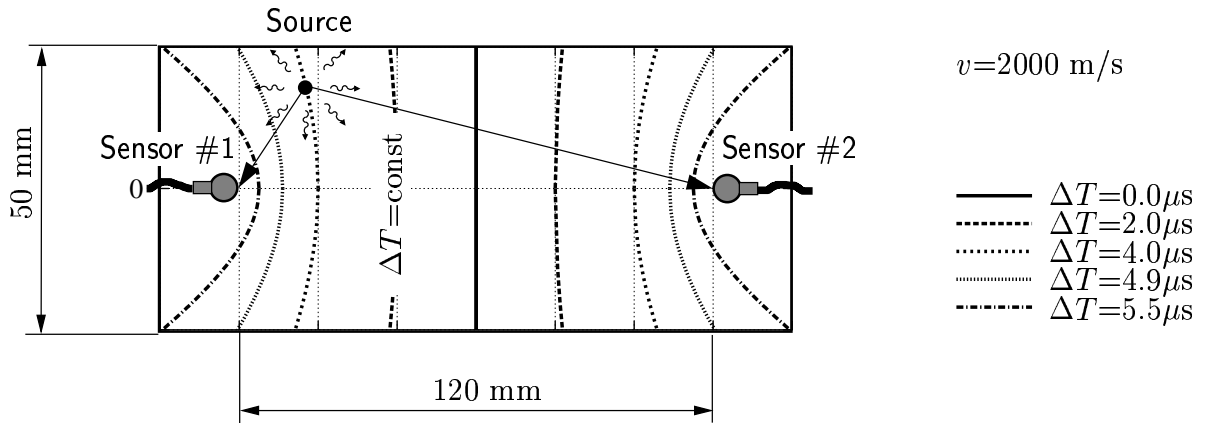


FIGURE 2.18: Problems with the linear time difference technique for small ratios of sensor separation to specimen width

1. Hyperbolic location curve error. A critical point is that the location of the acoustic emission source cannot be predicted uniquely, because the positions of constant time differences lie on a hyperbola. The event information of all events on this hyperbola is condensed into a point which lies on the straight line between the two sensors, and plots like in FIGURE 2.17 are obtained. Therefore, the location error is very high for events which occur in the regions close to the sensors.
2. Anisotropic sonic speed error. In the case of orthotropic, inhomogeneous materials the velocity of a wave traveling to the sensors is in general anisotropic and not constant as assumed in Equation (2.27). This source of error is the most critical one and is, beside others, the reason why the location technique can practically not be used for anisotropic materials.
3. Errors due to signals from outside. Signals may also come from outside of the investigated region (see curve $\Delta T = 5.5 \mu\text{s}$ in FIGURE 2.18). This leads to concentrated events near the sensors, which are visible at the right hand side of FIGURE 2.17. Filters have to be applied to eliminate this error.

It can be concluded that the acoustic emission technique is suitable for predicting the occurrence of first ply and progressive failure in the field of, in general, anisotropic materials. In contrast to that, the determination of the location of events is more difficult and reliable results can practically not be obtained for anisotropic multi-layered composites. Nevertheless, the application of two sensors is suggested in order to limit the investigated region and avoid errors due to signals from “outside”.

Chapter 3

Homogenization

3.1 Mathematical Background

The presented introduction to the mathematical background of the tensor and index notation tries to pursue two goals: On the one hand all presented basics for the following derivations should be given, and on the other hand both notations should be juxtaposed in order to make the content readable for mathematicians, engineers and physicists as well. Therefore, relevant derivations are written in tensor and index notation and juxtaposed with an arrow (" \longleftrightarrow ").

3.1.1 Coordinate Systems

The used coordinate systems are shown in FIGURE 3.1 and can be summarized as:

- A global x, y, z coordinate system for the global structure
- A global 1, 2, 3 coordinate system for the orientation of the unit cell
- A local l, q, t coordinate system for the principal material axes of the orthotropic material layers

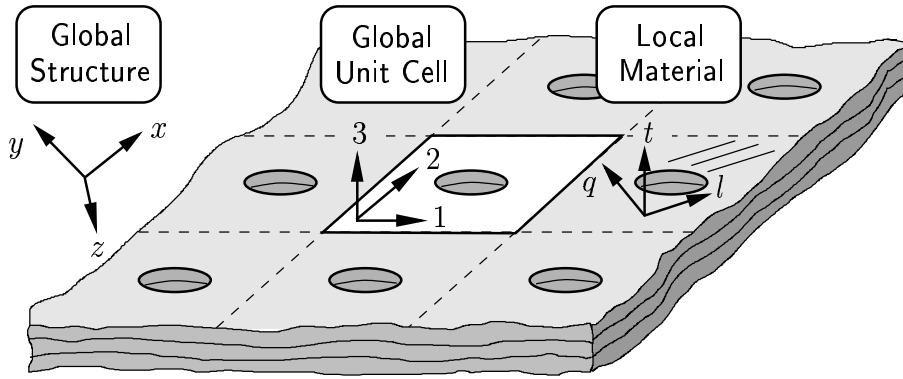


FIGURE 3.1: Applied coordinate systems

3.1.2 Introduction to Tensor and Index Notation

The following mathematical definitions are mainly based on Mang and Hofstetter [2000] and Saleeb and Chen [1983]. Vectors and matrices are only special tensors, namely tensors of first and second order, respectively.

If the three unit vectors $\underline{e}^1, \underline{e}^2, \underline{e}^3$ are given in a 1, 2, 3 coordinate system a vector (tensor of first order) \underline{a} can be written as

$$\underline{a} = a_1 \underline{e}^1 + a_2 \underline{e}^2 + a_3 \underline{e}^3 = a_1 \begin{pmatrix} 1 \\ 0 \\ 0 \end{pmatrix} + a_2 \begin{pmatrix} 0 \\ 1 \\ 0 \end{pmatrix} + a_3 \begin{pmatrix} 0 \\ 0 \\ 1 \end{pmatrix} = \begin{pmatrix} a_1 \\ a_2 \\ a_3 \end{pmatrix}. \quad (3.1)$$

Here, a_1, a_2, a_3 are the components (coefficients) of the vector \underline{a} in the 1, 2, 3 coordinate system. The transition to index notations is obtained by replacing the components of the vector \underline{e}^1 with $e_j^1 = e_1^1, e_2^1, e_3^1$. Then the connection between tensor (vector) and index notation reads as

$$\{\underline{e}^1\}_j = e_j^1 \quad (j = 1, 2, 3). \quad (3.2)$$

e_j^1 is the first unit vector in index notation. The brackets indicate the assignment of the individual coefficients to the “vector scheme”. Note, that the equation is not valid without the brackets.

The index j is an integer, which is 1, 2, 3 for 3D and 1,2 for 2D. The unit vectors in tensor notation $\underline{e}^1, \underline{e}^2, \underline{e}^3$ can then be written in index notation as e_j^1, e_j^2, e_j^3 (with $j = 1, 2, 3$ or $j = x, y, z$ depending on the used coordinate system). The unit vectors can

be further simplified as:

$$e_j^i = (e_j^1, e_j^2, e_j^3) \quad (i = 1, 2, 3). \quad (3.3)$$

Note, the superscript i , which characterizes the mutually perpendicular unit vectors in the $i = 1, 2, 3$ direction, is not an index in the sense of index notation. Therefore, the index is written as a superscript and not as a subscript. Furthermore arithmetic rules must not be applied on superscripts. Finally, Equation 3.1 can be written in index notation as:

$$\{\underline{\mathbf{a}}\}_j = a_1 e_j^1 + a_2 e_j^2 + a_3 e_j^3 = a_j \quad (j = 1, 2, 3), \quad (3.4)$$

where a_j are components of the vector $\underline{\mathbf{a}} = (a_1, a_2, a_3)^T$. It should be mentioned, that the equation of the form $a_j = a_i e_j^i$ is not correct and it is not a scalar product. A scalar product appears if a subscript appears twice in one term, i.e.:

$$a_m b_m = a_1 b_1 + a_2 b_2 + a_3 b_3, \quad (3.5)$$

where one has to sum up over all indices. This convention is known as Einstein's summation convention. The scalar product can also be written in tensor notation as the scalar product of the two vectors $\underline{\mathbf{a}}$ and $\underline{\mathbf{b}}$:

$$\underline{\mathbf{a}} \cdot \underline{\mathbf{b}} = a_m b_m = c, \quad (3.6)$$

where the arithmetic rule is indicated by the dot-operator (“.”). The repeated index is referred to as dummy index, while an index which appears once in a term is called a free index, e.g.:

$$a_{im} b_m = a_{i1} b_1 + a_{i2} b_2 + a_{i3} b_3 \quad (3.7)$$

In Equation (3.7) the index m is a dummy index and i is a free index. The conventions regarding subscripts described above can now be summarized in the following as a set of three rules:

1. If a subscript occurs exactly once in each term of an expression or of an equation, it is called a “free index”, for example:

$$a_{ikm} b_m + c_{ik} = d_{ik}, \quad (3.8)$$

where i and k are free indices.

2. If a subscript occurs exactly twice in one term of an expression or of an equation, it is called a “dummy index”. It is to be summed up from 1 to 3 for 3D in the related term. The dummy index may or may not occur exactly twice in any other term.

3. If a subscript occurs more than twice in one term of an expression or of an equation, it is a mistake.

3.1.3 General Remarks on Vectors, Matrices and Tensors

Definition

Often a vector is defined as oriented line. In 3D a vector is written as \underline{a} (see Section 3.1.2):

$$\{\underline{a}\}_i = a_i \quad (i = 1, 2, 3).$$

This is only one part of the definition of a vector. The mathematically correct definition reads as: In 3D vector or tensor of first order is a physical or mathematical variable if and only if it has the following properties:

1. Three numbers a_i are given in a coordinate system (e.g., 1, 2, 3), which define the physical or mathematical variable uniquely
2. The coordinates of a vector a_i and $a_{i'}$, which are defined in two arbitrary coordinate systems 1, 2, 3 and 1', 2', 3', respectively, are related by the equation:

$$\begin{aligned} a_i &= l_{ik'} a_{k'} \\ a_{i'} &= l_{i'k} a_k \end{aligned} \quad (3.9)$$

with $l_{ik'} = \cos \angle(ik')$ as transformation tensor

Scalar variables like temperature, density, etc., are tensors of zero order. Therefore, they are invariant to any spatial transformation.

A matrix is equivalent to a tensor of second order. The definition is equal to the above definition and reads as: In 3D a matrix or tensor of second order is a physical or mathematical variable if and only if it has the following properties:

1. Nine numbers a_i are given in a coordinate system (e.g., 1, 2, 3), which define the physical or mathematical variable uniquely
2. The coordinates of a matrix T_{ik} and $T_{i'k'}$, which are defined in two arbitrary coordinate systems 1, 2, 3 and 1', 2', 3', respectively, are related by the equation:

$$\begin{aligned} T_{ik} &= l_{im'} l_{kn'} T_{m'n'} \\ T_{i'k'} &= l_{mi'} l_{nk'} T_{mn} \end{aligned} \quad (3.10)$$

From these definitions it becomes evident that the number of the transformation tensors $l_{ik'}$, which are needed to transform a tensor from a 1, 2, 3 coordinate system to a 1', 2', 3' coordinate system, gives the order of the tensor. This rule is generally valid for a tensor of n -th order.

Arithmetic Tensor Rules

The first considered tensor operator is the dyadic product or also known as tensor product. A dyadic product of two tensors of the same or different order leads to a tensor, the order of which is the sum of the orders of the two basic tensors. For example, a tensor of second order is obtained from a dyadic product of two tensors of first order which reads as:

$$\underline{\underline{\mathbf{T}}} = \underline{\mathbf{a}} \otimes \underline{\mathbf{b}} = \begin{pmatrix} a_1 b_1 & a_1 b_2 & a_1 b_3 \\ a_2 b_1 & a_2 b_2 & a_2 b_3 \\ a_3 b_1 & a_3 b_2 & a_3 b_3 \end{pmatrix} \longleftrightarrow T_{ij} = a_i b_j \quad (3.11)$$

where $\underline{\mathbf{a}} \otimes \underline{\mathbf{b}} = \underline{\mathbf{a}} \underline{\mathbf{b}}^T$. Further examples are:

$$\begin{aligned} \underline{\mathbf{a}} \otimes \underline{\mathbf{b}} &= \underline{\underline{\mathbf{S}}}, & \longleftrightarrow & a_i b_j = S_{ij}, & (3.12) \\ \underline{\underline{\mathbf{S}}} \otimes \underline{\mathbf{a}} &= \underline{\underline{\underline{\mathbf{G}}}}, & \longleftrightarrow & S_{ij} a_k = G_{ijk}, \\ \underline{\underline{\mathbf{S}}} \otimes \underline{\underline{\mathbf{T}}} &= \underline{\underline{\underline{\underline{\mathbf{H}}}}}, & \longleftrightarrow & S_{ij} T_{kl} = H_{ijkl}, \end{aligned}$$

where the number of underlines corresponds to the order of the tensor.

A further tensor operation is the simple contraction, which is performed by setting two indices equal and using this as a dummy index. The simple contraction is better known as the scalar product of two tensors of first order, where the order of the tensors is reduced by the following rules:

$$\begin{aligned} \underline{\mathbf{a}} \cdot \underline{\mathbf{b}} &= c, & \longleftrightarrow & a_m b_m = c, & (3.13) \\ \underline{\underline{\mathbf{S}}} \cdot \underline{\mathbf{a}} &= \underline{\mathbf{b}}, & \longleftrightarrow & S_{im} a_m = b_i, \\ \underline{\underline{\mathbf{S}}} \cdot \underline{\underline{\mathbf{T}}} &= \underline{\underline{\mathbf{R}}}, & \longleftrightarrow & S_{im} T_{mj} = R_{ij}, \\ \underline{\underline{\underline{\mathbf{H}}}} \cdot \underline{\mathbf{a}} &= \underline{\underline{\mathbf{G}}}, & \longleftrightarrow & H_{ijkm} a_m = G_{ijk}. \end{aligned}$$

In analogy to the simple contraction a double contraction can be defined. The double contraction is also known as the scalar product of two tensors of second order, where

the order of the tensors is reduced by the following rules:

$$\begin{aligned} \underline{\underline{S}} : \underline{\underline{T}} &= c, & \longleftrightarrow & S_{mn} T_{mn} = c, \\ \underline{\underline{H}} : \underline{\underline{S}} &= \underline{\underline{R}}, & \longleftrightarrow & H_{ijmn} S_{mn} = R_{ij}. \end{aligned} \quad (3.14)$$

Next, the inverse tensor of a tensor of second order is treated. The inverse tensor of a second order tensor $\underline{\underline{T}}$ can be written symbolically as $\underline{\underline{T}}^{-1}$ and is defined as:

$$\underline{\underline{T}}^{-1} \cdot \underline{\underline{T}} = \underline{\underline{I}} \quad \longleftrightarrow \quad T_{ik}^{-1} T_{kj} = \delta_{ij}, \quad (3.15)$$

where $\underline{\underline{I}}$ is the identity matrix and δ_{ij} is the Kronecker Delta (see Section 3.1.4). That is, the scalar product of the inverse tensor and the original tensor of second order gives the identity matrix. The inverse tensor of second order follows from the original tensor as:

$$\underline{\underline{T}}^{-1} \quad \longleftrightarrow \quad T_{pi}^{-1} = \frac{1}{\det \underline{\underline{T}}} K_{ip} \quad \text{with} \quad K_{ip} = \frac{1}{2} \varepsilon_{ijk} \varepsilon_{pqr} T_{jp} T_{kr}, \quad (3.16)$$

where ε_{ijk} is the ε -tensor (see Section 3.1.4) and K_{ip} is the co-tensor of the tensor T_{pi} .

With the help of the ε -tensors the cross product of two vectors $\underline{\underline{a}}$ and $\underline{\underline{b}}$ can be written as:

$$\{\underline{\underline{a}} \times \underline{\underline{b}} = \underline{\underline{c}}\}_i = \varepsilon_{imn} a_m b_n = c_i. \quad (3.17)$$

Finally, the following rule holds for the derivatives of a tensor:

$$S_{ij} = \frac{\partial a_i}{\partial b_j}. \quad (3.18)$$

If b_j is the position vector x_j then the derivatives are written as:

$$\frac{\partial a_i}{\partial x_j} = a_{i,j}, \quad (3.19)$$

where “ $_{,j}$ ” is the short cut of $\partial/\partial x_j$.

3.1.4 Kronecker Delta and ε -Tensor

The Kronecker delta (δ_{ij}) is defined as

$$\delta_{ij} = \begin{cases} 0 & \text{for } i \neq j \\ 1 & \text{for } i = j, \end{cases}$$

and δ_{ij} can be obtained from unit vectors (Equation 3.3) as:

$$\delta_{ij} = e_m^i e_m^j. \quad (3.20)$$

A further possibility to derive δ_{ij} is given by the derivatives of the direction vectors x_i :

$$\delta_{ij} = \frac{\partial x_i}{\partial x_j} = x_{i,j}. \quad (3.21)$$

The Kronecker delta is also known as substituting parameter, because the following equality holds:

$$\delta_{im} T_{mj} = T_{im} \delta_{mj} = T_{ij}. \quad (3.22)$$

This means that δ_{mj} replaces the index m by the index j . Furthermore, the following connection between the Kronecker delta and the identity matrix $\underline{\underline{I}}$ holds:

$$\left\{ \begin{array}{ccc} 1 & 0 & 0 \\ 0 & 1 & 0 \\ 0 & 0 & 1 \end{array} \right\}_{ij} = \{\underline{\underline{I}}\}_{ij} = \delta_{ij}. \quad (3.23)$$

The ε -tensor, also named alternating tensor, is a tensor of third order, the components of which are defined as follows:

$$\begin{array}{ll} \varepsilon_{ijk} = 0 & \text{if two or three indices are equal} \\ \varepsilon_{ijk} = 1 & \text{for different indices in even permutation} \\ \varepsilon_{ijk} = -1 & \text{for different indices in odd permutation} \end{array} \quad (3.24)$$

where permutation means how many times the indices i, j, k have to be replaced with each other to obtain the basic sequence of the indices 1, 2, 3. For example:

$$\begin{array}{ll} \varepsilon_{123} = \varepsilon_{231} = \varepsilon_{312} = +1 & \text{(even permutation)} \\ \varepsilon_{132} = \varepsilon_{321} = \varepsilon_{213} = -1 & \text{(odd permutation)} \\ \text{all other } \varepsilon_{ijk} = 0 & \end{array} \quad (3.25)$$

Between the ε -tensor and the Kronecker δ the following relation holds:

$$\varepsilon_{ijm} \varepsilon_{klm} = \delta_{ik} \delta_{jl} - \delta_{il} \delta_{jk}, \quad (3.26)$$

which is known as δ - ε -identity.

3.1.5 Divergence Theorem

In continuum mechanics the total forces acting on a given volume of material consists of body forces (such as gravity forces) and surface forces (such as pressure). In the governing equations for the homogenization problem, these two types of forces are written as volume and surface integrals, respectively. In order to combine the two integrals, it is necessary to be able to express a surface integral as a volume integral or *vice versa*. The following divergence theorem of Gauss is applicable in such cases.

This theorem states that the surface integral of the normal component of a vector \underline{u} over a closed surface S is equal to the integral of the divergence of \underline{u} over the volume V enclosed by the surface:

$$\int_S \underline{u} \cdot \underline{n} \, dS = \int_V \operatorname{div} \underline{u} \, dV \quad \longleftrightarrow \quad \int_S u_i n_i \, dS = \int_V u_{i,i} \, dV, \quad (3.27)$$

where \underline{n} is the outward unit vector normal of the surface S . An example of the divergence theorem is the relation between volume average stresses ($\langle \sigma_{ij} \rangle$) and surface tractions (T_i) of a unit cell:

$$\langle \sigma_{ij} \rangle = \frac{1}{V} \int_V \sigma_{ij}(\underline{x}) \, dV = \frac{1}{2V} \int_S (T_i x_j + T_j x_i) \, dS, \quad (3.28)$$

which can be obtained from the following considerations: If the stresses are rewritten as:

$$\sigma_{ij} = (\sigma_{ik} x_j)_{,k} = \sigma_{ik,k} x_j + \sigma_{ik} x_{j,k} = \sigma_{ik} \delta_{kj} = \sigma_{ij} \quad (3.29)$$

and $\sigma_{ik,k} = 0$ (equilibrium condition without body forces), as well as $\sigma_{ik} n_k = T_i$ (traction vector) are taken into account it follows:

$$\begin{aligned} \frac{1}{V} \int_V \sigma_{ij}(\underline{x}) \, dV &= \frac{1}{2V} \int_V \left((\sigma_{ik} x_j)_{,k} + (\sigma_{jk} x_i)_{,k} \right) \, dV \\ &= \frac{1}{2V} \int_S (\sigma_{ik} x_j n_k + \sigma_{jk} x_i n_k) \, dS = \frac{1}{2V} \int_S (T_i x_j + T_j x_i) \, dS. \end{aligned} \quad (3.30)$$

3.2 Homogenization from the View Point of Standard FEM

3.2.1 Introduction

Periodic micro field approaches analyze the behavior of infinite (two- or three-dimensional) periodic arrangements of the constituents making up a given inhomogeneous material

under the action of far field mechanical loads or uniform temperature fields. A common approach for studying the stress and strain fields in such periodic media is based on partitioning it into periodically repeating unit cells, to which the investigations may be limited without loss of information or generality in the interior of a body, at least for static analysis (for example, a wave cannot pass through a unit cell, it is “locked in”).

Different homogenization concepts are known:

1. Standard finite element based concepts, which are also known as concept of “macroscopic degrees of freedom” (concept of master nodes). There, standard finite element programs are utilized to solve the homogenization problem. Introduction are given in Rammerstorfer and Böhm [1998], Michel et al. [1999], van Rens et al. [1998], and Anthoine [1995].
2. Asymptotic homogenization theory concepts, where a length scale parameter is introduced and expressions containing the linkage between the various length scales are obtained (see Suquet [1987], Hassani and Hinton [1998a], Hassani and Hinton [1998b], Hinton and Soden [1998]).

In this thesis a standard finite element based concept is used, which is based on small deformations and small strains.

3.2.2 Description of a Periodic Medium

Periodic media can be classified by the number of the axes of periodicity. One, two or three axes of periodicity are possible. In this thesis we define two-dimensional periodic media as plane periodic and three-dimensional periodic media as spatially periodic. As mentioned above, numerical analysis methods (finite element method, ...) are applied to solve the homogenization problem. In the case of plane periodic media we must further distinguish between 2D and 3D analysis models. 3D FE-models must be applied if for a plane periodic medium with inhomogeneous material behavior in thickness direction (e.g., a perforated laminate).

A periodic medium is characterized by independent vectors (see Anthoine [1995]), so-called periodicity vectors, $\underline{\mathbf{p}}^k$, where $\{\underline{\mathbf{p}}^k\}_{j=1}^k$ with $j = 1, 2, 3$ (see FIGURE 3.2). k is A, B for plane periodicity, and $k = A, B, C$ for spatial periodicity. For the cases studied here the following holds:

$$\underline{\mathbf{p}}^i \cdot \underline{\mathbf{p}}^k \neq 0 \quad \longleftrightarrow \quad p_j^i p_j^k \neq 0 \quad \text{for} \quad i \neq k, \quad (3.31)$$

that is, the individual vectors in general are not perpendicular to each other. These three independent periodicity vectors have the following properties: The local geometrical and mechanical characteristics of a point \underline{x} of the periodic medium, here defined as $\mathcal{F}(\underline{x})$, are invariant for any translation along a vector

$$\underline{t} = m_A \underline{p}^A + m_B \underline{p}^B + m_C \underline{p}^C \quad (3.32)$$

which leads to

$$\mathcal{F}(\underline{x}) = \mathcal{F}(\underline{x} + \underline{t}), \quad (3.33)$$

where the m_k are integer numbers. FIGURE 3.2 also shows the periodicity vectors for a spatial (left) and plane (right) periodic medium.

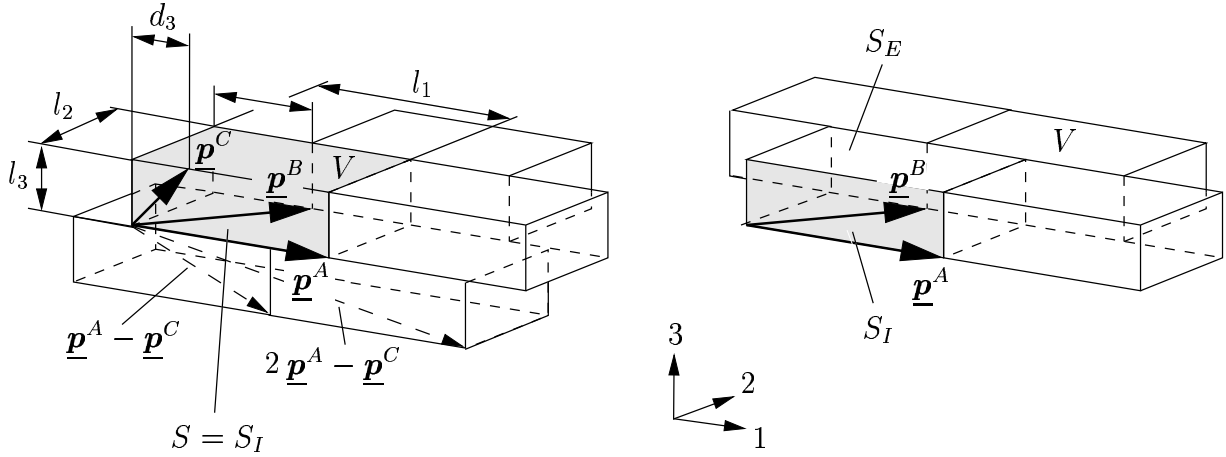


FIGURE 3.2: Spatially periodic media (left) and plane periodic media (right)

As a consequence, it is sufficient to define the mechanical properties of the medium on a small domain V (volume of the unit cell) to be repeated by translation. Based on this information the properties of the whole medium are obtained. In other words if the stresses and strains are known within this small domain, the stresses and strains are known for the whole domain.

In the general case of a three-dimensional spatially periodic medium (FIGURE 3.2, left) the reference frame is composed of the three periodicity vectors

$$\begin{aligned} \underline{p}^A &= l_1 \underline{e}^1 \\ \underline{p}^B &= d_2 \underline{e}^1 + l_2 \underline{e}^2 \\ \underline{p}^C &= d_3 \underline{e}^1 + l_3 \underline{e}^3 \end{aligned} \quad (3.34)$$

where l_i ($i=1, 2, 3$) are the dimensions of the unit cell and d_2, d_3 are the offsets in \underline{e}_2 - and \underline{e}_3 -direction, respectively. $d_2 = d_3 = 0$ gives a rectangular arrangement (orthogonal basic frame). Furthermore it can be seen from FIGURE 3.2 (left) that for a spatially periodic medium the boundary $S = S_I$ of a unit cell can be divided into three, four, or five pairs of identical sectors corresponding to each other.

In the case of plane periodic media (FIGURE 3.2, right) only two periodicity vectors $\underline{p}^A, \underline{p}^B$ must be defined. The boundary surface (S) may be divided into an internal surface (S_I) and an external surface (S_E), where the external boundary S_E is stress-free.

The choice of the unit cell depends strongly on the topology of the investigated medium. Many different shapes of unit cells have been presented up to now. For example, some possible unit cells for a plane hexagonal arrangement are shown in FIGURE 3.3. For this work a parallelepiped is chosen (FIGURE 3.3 center) as the shape of the investigated unit cell. The parallelogram is spanned by the periodicity vectors p_j^k where $k = A, B$ and $j = 1, 2$.

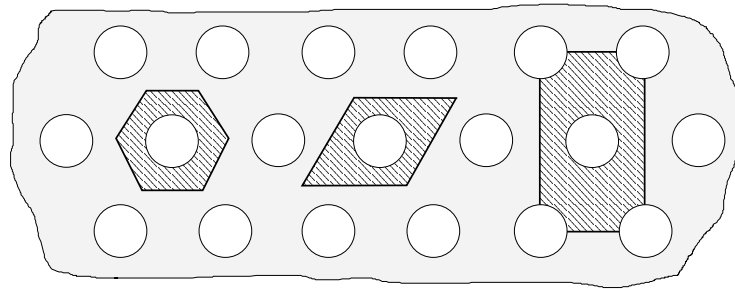


FIGURE 3.3: Possible unit cell shapes for plane hexagonal arrangements of holes

3.2.3 Homogenized Stresses and Strains

In the previous section it was demonstrated how the behavior of a periodic medium can be represented by the behavior of one unit cell. This unit cell is surrounded by the boundary S , where appropriate boundary conditions have to be applied. In mechanical terms, this means that, when passing from one cell to the next:

1. The stress tensor σ_{ij} is continuous on S_I (and zero on S_E)
2. Strains are compatible on S_I , i.e., neither separation nor overlapping occurs

Since passing from one cell to the next (identical), corresponds to passing from one side to the opposite side (denoted by the superscript “+” and “-”, respectively) within the same cell, condition (1) becomes: “Traction vectors T_i are opposite on corresponding sides of S_I ”, because normals n_j are opposite. Such a stress field σ_{ij} is called periodic on S_I , whereas the normal n_j and traction vectors T_i are called anti-periodic on S_I , which reads as:

$$\sigma_{ij}^+ = \sigma_{ij}^-, \quad T_i^+ = -T_i^- \quad \text{und} \quad n_j^+ = -n_j^-. \quad (3.35)$$

To ensure condition (2), it is necessary that the shapes of opposite sides on S_I are identical in the deformed state. In other words, the displacement fields on two opposite sides must be equal up to a “rigid body displacement”. Since such a displacement field $u_i(\underline{\mathbf{x}})$ leads to a periodic strain field, it is called strain-periodic. It can be shown that in general a strain-periodic displacement field $u_i(\underline{\mathbf{x}})$ may always be written in the following form (see Anthoine [1995], Suquet [1987]):

$$\underline{\mathbf{u}}(\underline{\mathbf{x}}) = \underline{\underline{\boldsymbol{\mathcal{E}}}} \cdot \underline{\mathbf{x}} + \underline{\mathbf{u}}^P(\underline{\mathbf{x}}) \quad \longleftrightarrow \quad u_i(\underline{\mathbf{x}}) = \mathcal{E}_{ij} x_j + u_i^P(\underline{\mathbf{x}}) \quad (3.36)$$

for spatial periodicity ($i, j=1, 2, 3$), and as:

$$\begin{aligned} u_i(\underline{\mathbf{x}}) &= \mathcal{E}_{ij} x_j - \chi_{ij} x_j x_3 + u_i^P(\underline{\mathbf{x}}) \\ u_3(\underline{\mathbf{x}}) &= \frac{1}{2} \chi_{mn} x_m x_n + u_3^P(\underline{\mathbf{x}}) \end{aligned} \quad (3.37)$$

for shell-like planar media ($i, j=1, 2$). \mathcal{E}_{ij} is the mean strain tensor and χ_{ij} is the mean curvature tensor. $u_i^P(\underline{\mathbf{x}})$ is a periodic displacement field which takes equal values on opposite sides of S_I . A graphical explanation of Equation (3.36) is given in FIGURE 3.4. There, the constant ($\mathcal{E}_{11} x_1$) and periodic displacements (u_1^P) are shown for the 1-direction.

The curvature tensor in Equation (3.37) is zero in the case of spatially periodic media or as long as the in-plane material behavior of plane periodic media is of interest. In the following the out-of-plane behavior will be disregarded, i.e., χ_{ij} is set to zero, and all given equations are valid for spatial and plane periodicity. It can be shown, by using the divergence theorem, that the mean strain tensor \mathcal{E}_{ij} corresponds to the volume average of the strains $\varepsilon_{ij}(\underline{\mathbf{x}})$ over the unit cell volume V , i.e.:

$$\underline{\underline{\boldsymbol{\mathcal{E}}}} = \langle \underline{\underline{\boldsymbol{\varepsilon}}}(\underline{\mathbf{x}}) \rangle = \frac{1}{V} \int_V \underline{\underline{\boldsymbol{\varepsilon}}}(\underline{\mathbf{x}}) dV \quad \longleftrightarrow \quad \mathcal{E}_{ij} = \langle \varepsilon_{ij}(\underline{\mathbf{x}}) \rangle = \frac{1}{V} \int_V \varepsilon_{ij}(\underline{\mathbf{x}}) dV. \quad (3.38)$$

The proof of Equation (3.38) follows directly if the strains are calculated from the displacements (Equation (3.36)) using $\varepsilon_{ij} = \frac{1}{2}(u_{i,j} + u_{j,i})$ which leads to

$$\varepsilon_{ij}(\underline{\mathbf{x}}) = \mathcal{E}_{ij} + \varepsilon_{ij}^P(\underline{\mathbf{x}}) \quad (3.39)$$

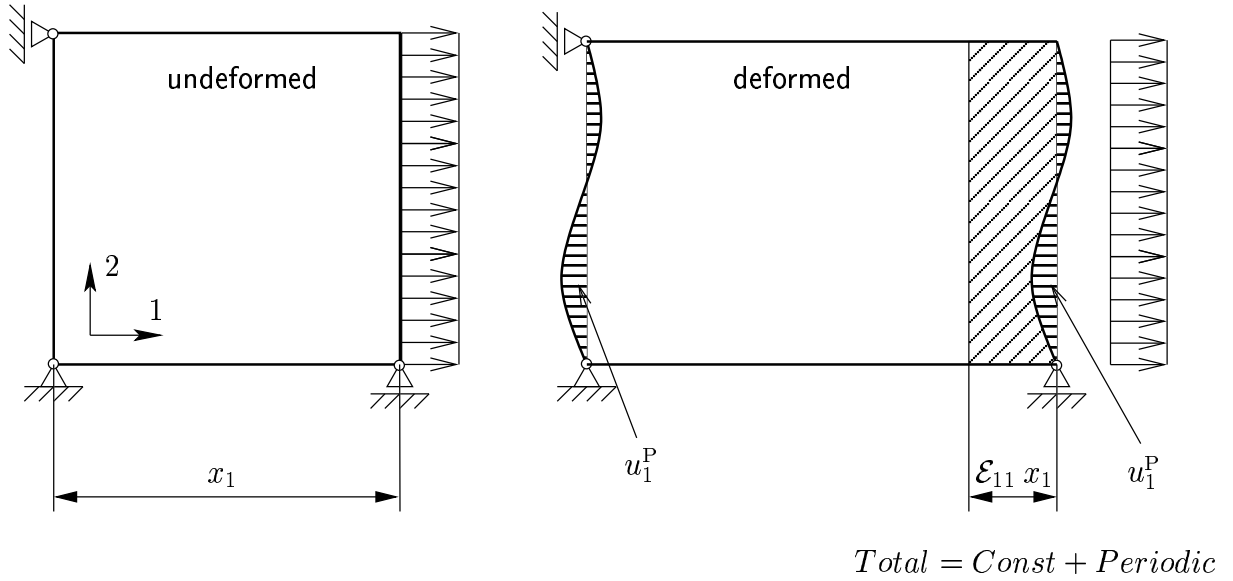


FIGURE 3.4: Basic idea of homogenization

and take into account that the following holds:

$$\langle \varepsilon_{ij}^P(\underline{\mathbf{x}}) \rangle = 0. \quad (3.40)$$

Thus, the proof is given by:

$$\mathcal{E}_{ij} = \langle \varepsilon_{ij}(\underline{\mathbf{x}}) \rangle = \langle \mathcal{E}_{ij} + \varepsilon_{ij}^P(\underline{\mathbf{x}}) \rangle = \langle \mathcal{E}_{ij} \rangle = \mathcal{E}_{ij}. \quad (3.41)$$

In a similar way the homogenized stress tensor can be written as:

$$\underline{\underline{\Sigma}} = \langle \underline{\underline{\sigma}}(\underline{\mathbf{x}}) \rangle = \frac{1}{V} \int_V \underline{\underline{\sigma}}(\underline{\mathbf{x}}) dV \quad \longleftrightarrow \quad \Sigma_{ij} = \langle \sigma_{ij}(\underline{\mathbf{x}}) \rangle = \frac{1}{V} \int_V \sigma_{ij}(\underline{\mathbf{x}}) dV. \quad (3.42)$$

It should be mentioned, that homogenized strains and stresses fulfill the following fundamental equation:

$$\langle \underline{\underline{\sigma}} \rangle : \langle \underline{\underline{\varepsilon}} \rangle = \langle \underline{\underline{\sigma}} : \underline{\underline{\varepsilon}} \rangle \quad \longleftrightarrow \quad \langle \sigma_{ij} \rangle \langle \varepsilon_{ij} \rangle = \langle \sigma_{ij} \varepsilon_{ij} \rangle. \quad (3.43)$$

This equation is known as Hill's Lemma (Hill [1963]), and says that the strain energy density $U = \frac{1}{2} \sigma_{ij} \varepsilon_{ij}$, which is calculated from the homogenized stresses and strains, has to be the same as the averaged strain energy density obtained from the local stresses and strains. The proof of Equation (3.43) is obtained if Equation (3.39) is substituted into Equation (3.43):

$$\Sigma_{ij} \mathcal{E}_{ij} = \langle \sigma_{ij} \rangle \mathcal{E}_{ij} + \langle \sigma_{ij} \varepsilon_{ij}^P \rangle. \quad (3.44)$$

Consequently it is sufficient to prove that $\langle \sigma_{ij} \varepsilon_{ij}^P \rangle = 0$. This proof follows by using the divergence theorem (Equation (3.28)):

$$\langle \sigma_{ij} \varepsilon_{ij}^P \rangle = \frac{1}{V} \int_V \sigma_{ij} (u_{j,i}^P + u_{i,j}^P) dV = \frac{1}{V} \int_S (T_i u_j^P + T_j u_i^P) dS = 0, \quad (3.45)$$

which leads to zero, because corresponding points (in the following denoted with “+” and “-”) on the surface S have anti-periodic traction vectors ($T_i^+ = -T_i^-$) and periodic displacements ($u_i^{P+} = u_j^{P-}$) which gives a vanishing integral on the right hand side of Equation (3.45).

Homogenized Strains and Master Node Displacements

An approximation of the homogenized strains \mathcal{E}_{ij} can be obtained directly from finite element results by taking the volume average:

$$\mathcal{E}_{ij} = \frac{1}{V} \int_V \varepsilon_{ij}(\underline{\mathbf{x}}) dV. \quad (3.46)$$

If the finite element program does not support the volume average of the strains a relation between the homogenized strains and “special” nodal displacements is needed. The required relation follows if Equation (3.36) is written down for two corresponding points $\underline{\mathbf{x}}$ and $\underline{\mathbf{x}} + \underline{\mathbf{t}}$ on S_I :

$$\begin{aligned} u_i(\underline{\mathbf{x}}) &= \mathcal{E}_{ij} x_j + u_i^P(\underline{\mathbf{x}}) \\ u_i(\underline{\mathbf{x}} + \underline{\mathbf{t}}) &= \mathcal{E}_{ij} (x_j + t_j) + u_i^P(\underline{\mathbf{x}} + \underline{\mathbf{t}}) \end{aligned} \quad (3.47)$$

which leads to:

$$u_i(\underline{\mathbf{x}} + \underline{\mathbf{t}}) - u_i(\underline{\mathbf{x}}) = \mathcal{E}_{ij} t_j, \quad (3.48)$$

because $u_i^P(\underline{\mathbf{x}}) = u_i^P(\underline{\mathbf{x}} + \underline{\mathbf{t}})$. Equation (3.48) is very important and describes the displacement boundary conditions of a unit cell. The next point is, that in a standard finite element code the homogenized strains \mathcal{E}_{ij} cannot be applied directly. The required equation follows from the assumption that:

- $\underline{\mathbf{x}}$ in Equation (3.48) is set to zero ($\underline{\mathbf{x}} = \underline{\mathbf{0}}$). That means that the origin of the periodicity vectors is set to the origin of the 1, 2, 3 coordinate system (see FIGURE 3.5). From this definition it follows directly that $\underline{\mathbf{t}} = \underline{\mathbf{p}}^k$ or in more detail $\underline{\mathbf{t}} = \underline{\mathbf{p}}^1$, $\underline{\mathbf{t}} = \underline{\mathbf{p}}^2$ and $\underline{\mathbf{t}} = \underline{\mathbf{p}}^3$ for corresponding surfaces.

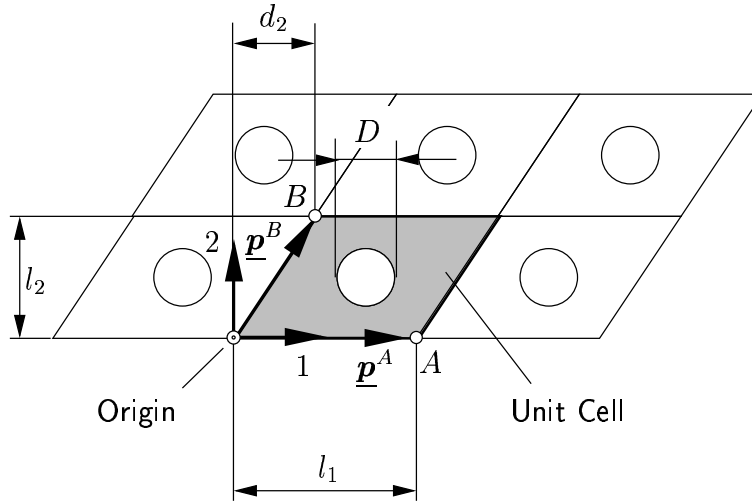


FIGURE 3.5: Origin of the 1, 2, 3 coordinate system and of the periodicity vectors

- In a second step the origin of the 1, 2, 3 coordinate system is fixed and it follows that $u_i(\underline{\mathbf{0}}) = \underline{\mathbf{0}}$.

By inserting these two assumptions into Equation (3.48) one obtains the following set of equations:

$$\underline{\mathbf{u}}(\underline{\mathbf{p}}^k) = \underline{\underline{\boldsymbol{\varepsilon}}} \cdot \underline{\mathbf{p}}^k = \underline{\mathbf{u}}^k \quad \longleftrightarrow \quad u_i(\underline{\mathbf{p}}^k) = \varepsilon_{ij} p_j^k = u_i^k \quad (k = A, B, C), \quad (3.49)$$

which represent a relation between the homogenized strains ε_{ij} and the displacements of characteristic nodes $u_i(\underline{\mathbf{p}}^1)$, $u_i(\underline{\mathbf{p}}^2)$, $u_i(\underline{\mathbf{p}}^3)$. These nodes are the end nodes of the periodicity vectors A , B , and C and are usually denoted as master nodes, because they control the mean displacement of the unit cell. Equations (3.49) specify, at given homogenized strains ε_{ij} , how the master nodes have to be translated in order to yield the homogenized strains ε_{ij} . These equations allow to simulate a strain-controlled loading of the unit cell.

If the unit cell is loaded under stress-control, i.e., Σ_{ij} are given, and homogenized strains ε_{ij} are calculated using master node displacements from the finite element analyses Equation (3.49) cannot be used directly and has to be transformed accordingly. Before, the transformation Equation (3.49) is rewritten as:

$$\underline{\underline{\mathbf{U}}} = \underline{\underline{\boldsymbol{\varepsilon}}} \cdot \underline{\underline{\mathbf{P}}} \quad \longleftrightarrow \quad U_{ij} = \varepsilon_{im} P_{mj}, \quad (3.50)$$

where the three Equations (3.49) are put into a single expression. U_{ij} and P_{mj} are generalized master node displacements and generalized periodicity vectors, respectively,

and can be written in extended form as:

$$\begin{pmatrix} u_1^A & u_1^B & u_1^C \\ u_2^A & u_2^B & u_2^C \\ u_3^A & u_3^B & u_3^C \end{pmatrix} = \begin{pmatrix} \mathcal{E}_{11} & \mathcal{E}_{12} & \mathcal{E}_{13} \\ \mathcal{E}_{21} & \mathcal{E}_{22} & \mathcal{E}_{23} \\ \mathcal{E}_{31} & \mathcal{E}_{32} & \mathcal{E}_{33} \end{pmatrix} \cdot \begin{pmatrix} p_1^A & p_1^B & p_1^C \\ p_2^A & p_2^B & p_2^C \\ p_3^A & p_3^B & p_3^C \end{pmatrix} \quad (3.51)$$

The required relation between master node displacements and homogenized strains follows directly from Equation (3.50) by taking the inverse:

$$\underline{\underline{\boldsymbol{\varepsilon}}} = \underline{\underline{\mathbf{U}}} \cdot \underline{\underline{\mathbf{P}}}^{-1} \quad \longleftrightarrow \quad \mathcal{E}_{lk} = U_{li} P_{ik}^{-1}, \quad (3.52)$$

with

$$P_{ik}^{-1} = \frac{1}{2 \det(P_{ik})} \varepsilon_{krs} \varepsilon_{itu} P_{rt} P_{su} \quad (3.53)$$

and

$$\det(P_{ik}) = \varepsilon_{ijk} P_{i1} P_{j2} P_{k3} = \varepsilon_{ijk} p_i^A p_j^B p_k^C = V \quad (3.54)$$

(V is the volume of the unit cell). Note that the homogenized strain tensor defined in Equation (3.52) could be unsymmetrical, because if the indize l and k are swapped $\mathcal{E}_{lk} \neq \mathcal{E}_{kl}$, where $\mathcal{E}_{kl} = P_{ki}^{-1} U_{il}$. From the engineering point of view that means: For a given unsymmetrical generalized periodicity tensor P_{ik} (describes the geometry of the unit cell) and an arbitrarily choosen unsymmetrical generalized master node displacement tensor U_{li} (describes the deformation of the unit cell) \mathcal{E}_{lk} might be unsymmetrical, which is the case if the generalized master node displacement tensor contains rigid body movements. Therefore, Equation (3.52) is rewritten as:

$$\underline{\underline{\boldsymbol{\varepsilon}}} = \frac{1}{2} (\underline{\underline{\mathbf{U}}} \cdot \underline{\underline{\mathbf{P}}}^{-1} + (\underline{\underline{\mathbf{P}}}^{-1})^T \cdot \underline{\underline{\mathbf{U}}}^T) \quad \longleftrightarrow \quad \mathcal{E}_{lk} = \frac{1}{2} (U_{li} P_{ik}^{-1} + P_{ki}^{-1} U_{il}) \quad (3.55)$$

to reach a symmetrical strain tensor.

The proof of Equation (3.55) starts with the meso-scopic displacement field given in Equation (3.36). First the displacement field is rewritten in terms of meso-scopic displacements (denoted with the superscript "m") and macro-scopic displacements (denoted with the superscript "M"):

$$\text{Meso: } u_i^m = \mathfrak{E}_{ik}^M{}^0 x_k + (u_i^P)^m \quad \text{Macro: } u_i^M = \mathfrak{E}_{ik}^M{}^0 x_k, \quad (3.56)$$

where instead of the macro-scopic homogenized strains \mathcal{E}_{ik} a new tensor \mathfrak{E}_{ik}^M is introduced. Furthermore, the superscript "0" is added to the position vector x_k meaning it is

the position vector of the undeformed state. With these definitions the meso-scopic and macro-scopic deformation gradients follows as (see Mang and Hofstetter [2000]):

$$\text{Meso: } {}^t_0X_{ij}^m = \left(\delta_{ij} + \frac{\partial u_i^m}{\partial x_j} \right) \quad \text{Macro: } {}^t_0X_{ij}^M = \left(\delta_{ij} + \frac{\partial u_i^M}{\partial x_j} \right), \quad (3.57)$$

where the superscript “ t ” indicated the deformed state at time t . Inserting Equation (3.56) into Equation (3.57) gives:

$$\text{Meso: } {}^t_0X_{ij}^m = \left(\delta_{ij} + \mathfrak{E}_{ij}^M + \frac{\partial(u_i^P)^m}{\partial x_j} \right) \quad \text{Macro: } {}^t_0X_{ij}^M = \left(\delta_{ij} + \mathfrak{E}_{ij}^M \right). \quad (3.58)$$

The Green-Lagrange strain tensor is then obtained from the deformation gradients as (see Bathe [1996]):

$$\underline{\underline{\varepsilon}}^{(m,M)} = \frac{1}{2} \left(({}^t_0\underline{\underline{\mathbf{X}}}^{(m,M)})^T \cdot {}^t_0\underline{\underline{\mathbf{X}}}^{(m,M)} - \underline{\underline{\mathbf{I}}} \right) \longleftrightarrow \varepsilon_{ij}^{(m,M)} = \frac{1}{2} \left({}^t_0X_{ki}^{(m,M)} {}^t_0X_{kj}^{(m,M)} - \delta_{ij} \right) \quad (3.59)$$

If the macro-scopic deformation gradient Equation (3.58) is inserted into Equation (3.59) and the higher order strain terms are neglected the linearized strains follow for the case of macro-scopic strain quantities as:

$$\varepsilon_{ij}^M = \mathcal{E}_{ij} = \frac{1}{2} \left(\mathfrak{E}_{ij}^M + \mathfrak{E}_{ji}^M \right), \quad (3.60)$$

where $\mathfrak{E}_{ij}^M = U_{ik} P_{kj}^{-1}$. Equation (3.60) proofs Equation (3.55). Furthermore, it is obvious that $\mathcal{E}_{ij} = \mathfrak{E}_{ij}^M$ if $\mathfrak{E}_{ij}^M = \mathfrak{E}_{ji}^M$, i.e., if \mathfrak{E}_{ij}^M is a symmetrical tensor.

Based on these considerations the question arises, if Equation (3.50) also should be rewritten. However, in this equations a symmetrical strain tensor is given. Therefore, a modification of these equations is not necessary.

For numerical implementation the periodicity vectors from Equation (3.34) are substituted into Equation (3.50) and Equation (3.55), and the following matrices are obtained:

$$\underline{\underline{\mathbf{U}}} = \begin{pmatrix} \mathcal{E}_{11} l_1 & \mathcal{E}_{12} l_2 + d_2 \mathcal{E}_{11} & \mathcal{E}_{13} l_3 + d_3 \mathcal{E}_{11} \\ \mathcal{E}_{21} l_1 & \mathcal{E}_{22} l_2 + d_2 \mathcal{E}_{21} & \mathcal{E}_{23} l_3 + d_3 \mathcal{E}_{21} \\ \mathcal{E}_{31} l_1 & \mathcal{E}_{32} l_2 + d_2 \mathcal{E}_{31} & \mathcal{E}_{33} l_3 + d_3 \mathcal{E}_{31} \end{pmatrix} \quad (3.61)$$

$$\underline{\underline{\boldsymbol{\varepsilon}}} = \begin{pmatrix} \frac{u_1^A}{l_1} & \frac{1}{2} \left(\frac{u_2^A}{l_1} + \frac{u_1^B}{l_2} - \frac{u_1^A d_2}{l_1 l_2} \right) & \frac{1}{2} \left(\frac{u_3^A}{l_1} + \frac{u_1^C}{l_3} - \frac{u_1^A d_3}{l_1 l_3} \right) \\ & \frac{u_2^B}{l_2} - \frac{u_2^A d_2}{l_1 l_2} & \frac{1}{2} \left(\frac{u_3^B}{l_2} - \frac{u_3^A d_2}{l_1 l_2} + \frac{u_2^C}{l_3} - \frac{u_2^A d_3}{l_1 l_3} \right) \\ \text{sym.} & & \frac{u_3^C}{l_3} - \frac{u_3^A d_3}{l_1 l_3} \end{pmatrix}. \quad (3.62)$$

Equation (3.61) is used for strain-controlled loading, where \mathcal{E}_{ij} is given and the master node displacements are calculated and used as loading for the finite element analysis. Equation (3.62) is used for stress-controlled loading, where the master node displacements are given (results from the finite element analysis) and the homogenized strains are computed. For a more detailed description see Section 3.2.4.

Homogenized Stresses and Master Node Forces

In analogy to the previous section the homogenized stresses (Σ_{ij}) can be computed from the volume average of the local stresses ($\sigma_{ij}(\underline{\mathbf{x}})$):

$$\Sigma_{ij} = \frac{1}{V} \int_V \sigma_{ij}(\underline{\mathbf{x}}) dV. \quad (3.63)$$

Another possibility are relations between homogenized stresses and master node forces. The starting point of the derivations is Equation (3.42). Then the application of the divergence theorem (Equation (3.28)) gives:

$$\Sigma_{ij} = \frac{1}{2V} \int_{S_I} (T_i x_j + T_j x_i) dS_I. \quad (3.64)$$

First, the internal surfaces S_I are split into two corresponding surfaces, S_I^{k-} and S_I^{k+} , respectively (k stands for the considered direction of the periodicity vector p_i^k). The corresponding direction vectors are denoted as x_i^k and $x_i^k + p_i^k$, respectively. If these definitions are substituted into Equation (3.64) it follows:

$$\Sigma_{ij} = \frac{1}{2V} \int_{S_I^{k+}} (T_i^{k+} (x_j^k + p_j^k) + T_j^{k+} (x_i^k + p_i^k)) dS_I^{k+} + \frac{1}{2V} \int_{S_I^{k-}} (T_i^{k-} x_j^k + T_j^{k-} x_i^k) dS_I^{k-}. \quad (3.65)$$

Using Equation (3.35) one ends up with:

$$\Sigma_{ij} = \frac{1}{2V} \int_{S_I^{k+}} (T_i^{k+} p_j^k + T_j^{k+} p_i^k) dS_I^{k+}. \quad (3.66)$$

There, the tensors p_i^k are independent of location and can be extracted from the integral in Equation (3.66). If the remaining integral is rewritten as:

$$\int_{S_I^{k+}} T_i^{k+} dS_I^{k+} = F_i^{k+}, \quad (3.67)$$

where F_i^{k+} are nodal forces at an arbitrary location on S_I^{k+} , Equation (3.66) leads to:

$$\Sigma_{ij} = \frac{1}{2V} (F_i^{k+} p_j^k + F_j^{k+} p_i^k). \quad (3.68)$$

So far, the location of the load introduction of the force F_i^{k+} has not been defined. In this work F_i^{k+} is chosen as the force in the corresponding master node, because master nodes are the only active boundary nodes in the finite element model. The forces are denoted as F_i^k in the following. The introduction of a generalized master node force $\underline{\underline{F}}$ yields:

$$\underline{\underline{\Sigma}} = \frac{1}{2V} (\underline{\underline{F}} \cdot \underline{\underline{P}}^T + \underline{\underline{P}} \cdot \underline{\underline{F}}^T) \quad \longleftrightarrow \quad \Sigma_{ij} = \frac{1}{2V} (F_{im} P_{mj} + P_{jm} F_{mi}) \quad (3.69)$$

with

$$\underline{\underline{F}} = \begin{pmatrix} F_1^A & F_1^B & F_1^C \\ F_2^A & F_2^B & F_2^C \\ F_3^A & F_3^B & F_3^C \end{pmatrix}, \quad (3.70)$$

where the symmetry of Σ_{ij} is evident. For numerical implementation the periodicity vectors from Equation (3.34) are inserted into Equation (3.69), which leads to:

$$\underline{\underline{\Sigma}} = \frac{1}{2V} \begin{pmatrix} 2(F_1^A l_1 + F_1^B d_2 + F_1^C d_3) & F_2^A l_1 + F_1^B l_2 + F_2^B d_2 + F_2^C d_3 & F_3^A l_1 + F_1^C l_3 + F_3^B d_2 + F_3^C d_3 \\ & 2F_2^B l_2 & F_3^B l_2 + F_2^C l_3 \\ \text{sym.} & & 2F_3^C l_3 \end{pmatrix}. \quad (3.71)$$

The inverse expression of Equation (3.69) is of the form:

$$\underline{\underline{F}} = V \underline{\underline{\Sigma}} \cdot (\underline{\underline{P}}^T)^{-1} \quad \longleftrightarrow \quad F_{ij} = V \Sigma_{im} P_{mj}^{-1}. \quad (3.72)$$

The proof follows directly if Equation (3.72) is inserted into Equation (3.69), i.e.:

$$\underline{\underline{\Sigma}} = \frac{1}{2V} \left(V \underline{\underline{\Sigma}} \cdot (\underline{\underline{P}}^T)^{-1} \cdot \underline{\underline{P}}^T + (V \underline{\underline{\Sigma}} \cdot (\underline{\underline{P}}^T)^{-1} \cdot \underline{\underline{P}}^T)^T \right), \quad (3.73)$$

and by taking into account that

$$\begin{aligned} (\underline{\underline{P}}^T)^{-1} \cdot \underline{\underline{P}}^T &= \underline{\underline{I}} \\ \underline{\underline{\Sigma}} &= \underline{\underline{\Sigma}}^T. \end{aligned}$$

The equation required for the implementation is obtained by using Equation (3.34) in conjunction with Equation (3.72):

$$\underline{\underline{F}} = \begin{pmatrix} \Sigma_{11} l_2 l_3 - \Sigma_{12} l_3 d_2 - \Sigma_{13} l_2 d_3 & \Sigma_{12} l_1 l_3 & \Sigma_{13} l_1 l_2 \\ \Sigma_{12} l_2 l_3 - \Sigma_{22} l_3 d_2 - \Sigma_{23} l_2 d_3 & \Sigma_{22} l_1 l_3 & \Sigma_{23} l_1 l_2 \\ \Sigma_{13} l_2 l_3 - \Sigma_{23} l_3 d_2 - \Sigma_{33} l_2 d_3 & \Sigma_{23} l_1 l_3 & \Sigma_{33} l_1 l_2 \end{pmatrix}. \quad (3.74)$$

Finally, some remarks with respect to uniqueness of the above equations are made. Equation (3.71) describes the relation between six independent homogenized stresses ($\Sigma_{11}, \Sigma_{12}, \Sigma_{13}, \Sigma_{22}, \Sigma_{23}, \Sigma_{33}$) and nine master node forces ($F_1^A, F_2^A, F_3^A, F_1^B, F_2^B, F_3^B, F_1^C, F_2^C, F_3^C$). Moreover, Equation (3.71) does not contain the three master node forces of the fixed origin. In sum, twelve master node forces are related to six independent homogenized stresses. Uniqueness is reached by introducing the equilibrium conditions:

$$\sum_i F_i = 0 \quad \sum_i M_{i0} = 0 \quad (i = 1, 2, 3). \quad (3.75)$$

Equilibrium is, of course, implicitly fulfilled by the finite element model, because Equation (3.71) is utilized at strain-controlled loading. There, the master node displacements are given and the corresponding master node forces are computed by solving the finite element problem. These six Equations (3.75) reduce the twelve dependent master node forces in Equation (3.71) to six independent master node forces.

3.2.4 Summary of the Homogenization Problem

The homogenized constitutive law for a perforated laminate in terms of classical lamination theory can be written as (see Section 2.2):

$$\begin{pmatrix} \underline{\mathbf{N}}^h \\ \underline{\mathbf{M}}^h \end{pmatrix} = \begin{pmatrix} \underline{\underline{\mathbf{A}}}^h & \underline{\underline{\mathbf{B}}}^h \\ \underline{\underline{\mathbf{B}}}^h & \underline{\underline{\mathbf{D}}}^h \end{pmatrix} \begin{pmatrix} \underline{\underline{\boldsymbol{\varepsilon}}}^h \\ \underline{\underline{\boldsymbol{\chi}}}^h \end{pmatrix} \quad (3.76)$$

with $\underline{\mathbf{N}}^h, \underline{\mathbf{M}}^h, \underline{\underline{\boldsymbol{\varepsilon}}}^h, \underline{\underline{\boldsymbol{\chi}}}^h$ being the generalized stress resultants and strain quantities for layered plates. The aim of stiffness investigations is to determine the homogenized plate stiffness matrices $\underline{\underline{\mathbf{A}}}^h, \underline{\underline{\mathbf{B}}}^h$ and $\underline{\underline{\mathbf{D}}}^h$. Following Section 3.2, periodic boundary conditions (BCs) have to be applied on the boundaries of an appropriate finite element unit cell (as shown in FIGURE 3.5) which read as (see Equation (3.48)):

$$u_i(\underline{\mathbf{x}} + \underline{\mathbf{p}}^k) - u_i(\underline{\mathbf{x}}) = \mathcal{E}_{ij} p_j^k \quad (k = A, B, C), \quad (3.77)$$

in order to ensure that for each undeformed and deformed configuration the translated unit cells fit to each other. Considering periodic BCs, the displacement field within the unit cell is completely defined by the displacements of characteristic points, so called master nodes (A and B in FIGURE 3.5). Consequently, the distributed loads acting along the boundary of the unit cell are condensed into concentrated nodal forces at the master

nodes. For example, for the special case of a symmetric lay-up and in-plane loading conditions, to which the results presented here are restricted, the following holds:

$$\begin{pmatrix} u_1^A & u_1^B \\ u_2^A & u_2^B \end{pmatrix} = \begin{pmatrix} \mathcal{E}_{11} & \mathcal{E}_{12} \\ \mathcal{E}_{21} & \mathcal{E}_{22} \end{pmatrix} \cdot \begin{pmatrix} p_1^A & p_1^B \\ p_2^A & p_2^B \end{pmatrix} \quad (3.78)$$

or in compact form:

$$\underline{\underline{\mathbf{U}}} = \underline{\underline{\boldsymbol{\varepsilon}}} \cdot \underline{\underline{\mathbf{P}}}, \quad (3.79)$$

where $\underline{\underline{\mathbf{U}}}$ is the generalized master node displacement tensor, $\underline{\underline{\boldsymbol{\varepsilon}}}$ is the homogenized strain and $\underline{\underline{\mathbf{P}}}$ is the generalized periodicity tensor containing the unit cell geometry l_1, l_2 and d_2 . The homogenized stress $\underline{\underline{\boldsymbol{\Sigma}}}$ can be obtained from (see Equation (3.69))

$$\underline{\underline{\boldsymbol{\Sigma}}} = \frac{1}{2V} \left(\underline{\underline{\mathbf{F}}} \cdot \underline{\underline{\mathbf{P}}}^T + (\underline{\underline{\mathbf{F}}} \cdot \underline{\underline{\mathbf{P}}}^T)^T \right). \quad (3.80)$$

where $\underline{\underline{\mathbf{F}}} = [(F_1^A, F_2^A)^T (F_1^B, F_2^B)^T]$ is the generalized master node force tensor. V is the volume of the unit cell and “ \cdot ” stands for the dot product. That means if $\underline{\underline{\boldsymbol{\varepsilon}}}$ is given (strain-controlled loading) $\underline{\underline{\mathbf{U}}}$ follows from Equation (3.79), $\underline{\underline{\mathbf{F}}}$ is calculated by using FE-analyses and $\underline{\underline{\boldsymbol{\Sigma}}}$ is computed from Equation (3.80). Finally, $\underline{\underline{\mathbf{N}}}^h = t^{\text{lam}} (\Sigma_{11}, \Sigma_{22}, \Sigma_{12})^T$ ($t^{\text{lam}} \dots$ laminate thickness) and $\underline{\underline{\boldsymbol{\varepsilon}}}^h = (\mathcal{E}_{11}, \mathcal{E}_{22}, 2\mathcal{E}_{12})^T$ are substituted into Equation (3.76), and $\underline{\underline{\mathbf{A}}}^h$ is obtained. The equations for stress-controlled loading look similarly and read as (see Equation (3.72) and Equation (3.55)):

$$\underline{\underline{\mathbf{F}}} = V \underline{\underline{\boldsymbol{\Sigma}}} \cdot (\underline{\underline{\mathbf{P}}}^T)^{-1} \quad (3.81)$$

$$\underline{\underline{\boldsymbol{\varepsilon}}} = \frac{1}{2} \left(\underline{\underline{\mathbf{U}}} \cdot \underline{\underline{\mathbf{P}}}^{-1} + (\underline{\underline{\mathbf{U}}} \cdot \underline{\underline{\mathbf{P}}}^{-1})^T \right). \quad (3.82)$$

A mathematical view of the homogenization problem described above is given in the following. In order to calculate σ_{ij} and u_i anywhere within the reference unit cell, equilibrium conditions and constitutive relationships must be added to the above equations so that the problem to be solved is:

$$\begin{aligned} \sigma_{ij,j} &= 0 \quad \text{on } V && \text{(equilibrium, no body forces)} \\ d\sigma_{ij} &= C_{ijkl} d\varepsilon_{kl} && \text{(constitutive law)} \\ T_i &\text{ anti-periodic on } S_I && (\sigma_{ij} \text{ periodic on } S_I) \\ T_i &= 0 \quad \text{on } S_E && \text{(only for plane periodicity)} \\ u_i - E_{ij} x_j &\text{ periodic on } S_I \\ \langle \sigma_{ij} \rangle &= \Sigma_{ij} \quad \text{given} && \text{(stress-controlled loading)} \\ \text{or} \\ \langle \varepsilon_{ij} \rangle &= E_{ij} \quad \text{given} && \text{(strain-controlled loading)} \end{aligned} \quad (3.83)$$

Chapter 4

Determination of Material Properties

This chapter is focussed on the determination of various material properties under static loading conditions. The first part deals with stiffness and strength investigations of non-perforated and perforated laminates in order to obtain in-plane material properties. In the second part, out-of-plane (inter-laminar) shear strengths are determined from numerical and experimental investigations of short-beam-shear and double-lap-shear specimens. Both parts are done in combination with acoustic emission testing. Thus, first ply failure strength values are obtained additionally.

4.1 Tensile Test Specimen

The first challenge of the experimental work is the choice of a proper specimen geometry to obtain the in-plane tensile properties E_l , E_q , G_{lq} , $R_{ll}^{(+)}$, $R_{qq}^{(+)}$, and R_{ql} of the investigated composite material. An overview of several standardized tensile test methods is given in ASM-Handbook [2002]. The various methods can be summarized as follows:

- ASTM D 3039: “Standard test method for tensile properties of polymer matrix composites”. The specimen is usually a straight sided and flat coupon with or without tabs on both ends (see FIGURE 4.3). Tabs are needed for load introduction into the gage region, while the design of end tabs remains somewhat of an art. Therefore, they are not standardized. The use of soft and ductile tab materials is suggested. If the tabs tend to debond it is recommended not to use tabs. Many laminates (mostly non uni-directional) can be tested successfully without tabs.

- ASTM D 638: “Standard test method for tensile properties of plastics”. The specimens looks like a “dog-bone” (see FIGURE 4.1 top). Therefore, it has the nickname “dog-bone” coupon. The specimen has a straight sided gage section and an increased width at the end of the gage sections, where the width increase is usually realized using a constant radius. Tabs are not needed in the grip regions. While the ASTM D 638 coupon configuration has been used successfully for fabric-reinforced composites and for general non uni-directional laminates, some material systems remain sensitive to the stress concentration at the radius.

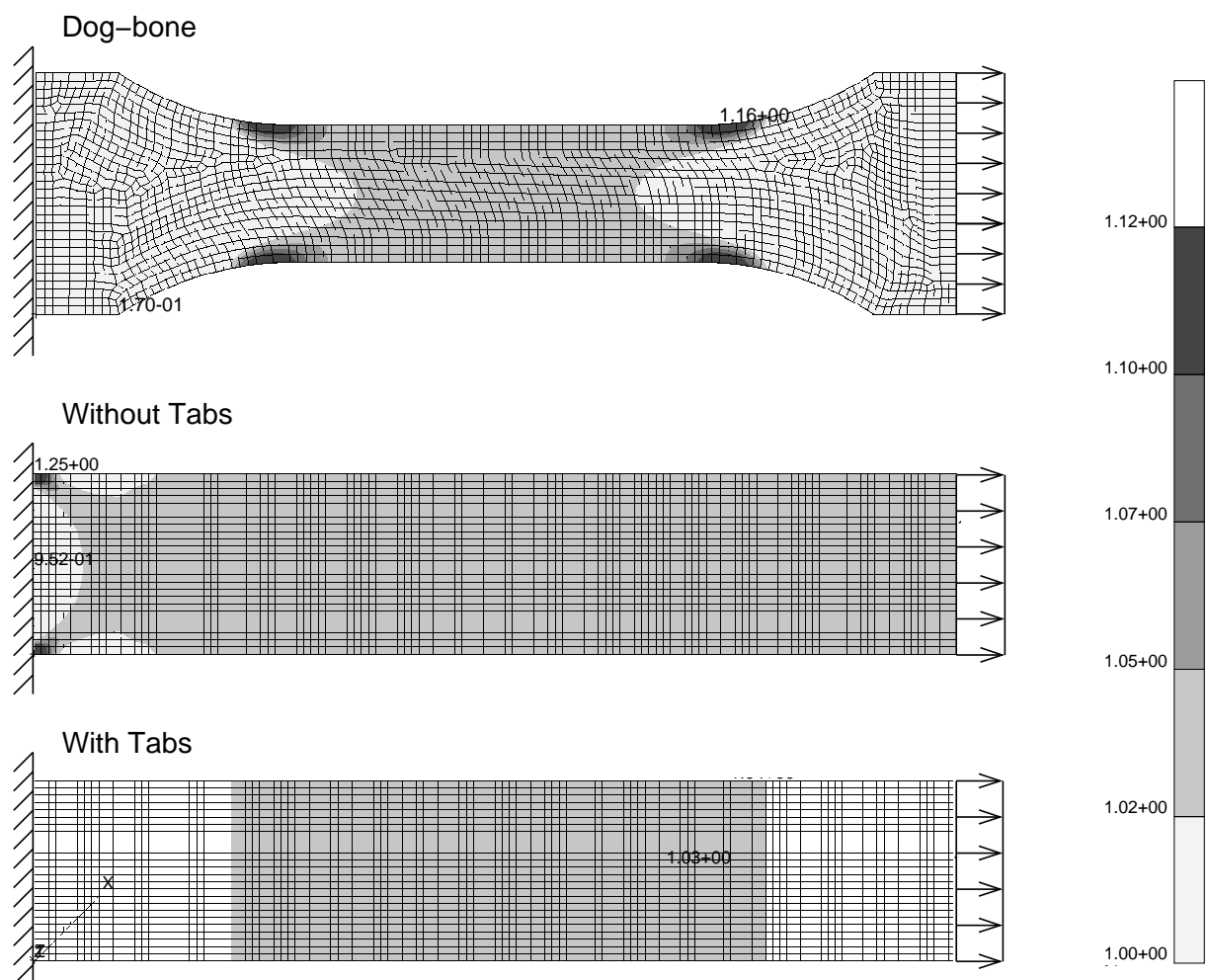


FIGURE 4.1: Risk parameter for a dog-bone coupon (top), a coupon without tabs (center), and for a coupon with tabs (bottom)

Following the guidelines above, all three coupon types may be utilized for the testing of non-perforated and perforated woven fabric laminates. In order to find the most suitable specimen shape the risk parameter is calculated for all three types, where the gage length and gage cross section, as well as the applied load are constant in all three cases. Results for the investigated perforated laminate are displayed in FIGURE 4.1. The evaluation procedure and material parameters are described in more detail in Section 4.3 and Section 5.1, respectively. Various boundary conditions are chosen on the two edges. On the left hand side of the coupon the displacements are fully constraint (fixed). On the right hand side of the specimen's edge nodal forces are applied. These boundary conditions are two extreme cases. The real boundary conditions and real risk parameter are somewhere in between. The specimens are loaded such, that the risk parameter in the gage region is approximately one. Furthermore, the risk parameter is only shown within the perforated regions without tabs. Glass fiber reinforced woven fabric tabs are used and are oriented at 45° with respect to the longitudinal axis of the specimen. The differences between the risk parameters in the gage section and the maximum risk parameter are 1%, 21% and 13% for the coupon with tabs, without tabs and the dog-bone specimen, respectively. The dog-bone coupon (FIGURE 4.1 top) shows stress concentrations at the radius, while the coupons without tabs (FIGURE 4.1 center) have a critical region at the fixed boundary due to the constrained Poisson effect. The coupon with tabs (FIGURE 4.1 bottom) is practically homogeneously loaded. Based on these results the coupon with tabs is considered to be the most proper one.

The final geometry used, which follows the requirement of a homogeneously loaded specimen, is shown in FIGURE 4.2 for a perforated coupon and in FIGURE 4.3 for a non-perforated coupon. The width of the specimens is different in the two cases, in order to fulfill the homogenization assumption as much as possible. Approximately 11 holes are within the width of a specimen in the investigated perforated case. The tab regions are staggered in two steps, where a rule of thumb is that the staggered tab region (without the grip region) should be approximately equal to the width of the specimen. Additional tabs are applied at the grips. The length of the gage region is chosen to be the same for the perforated and non-perforated coupons and has a value of 150 mm.

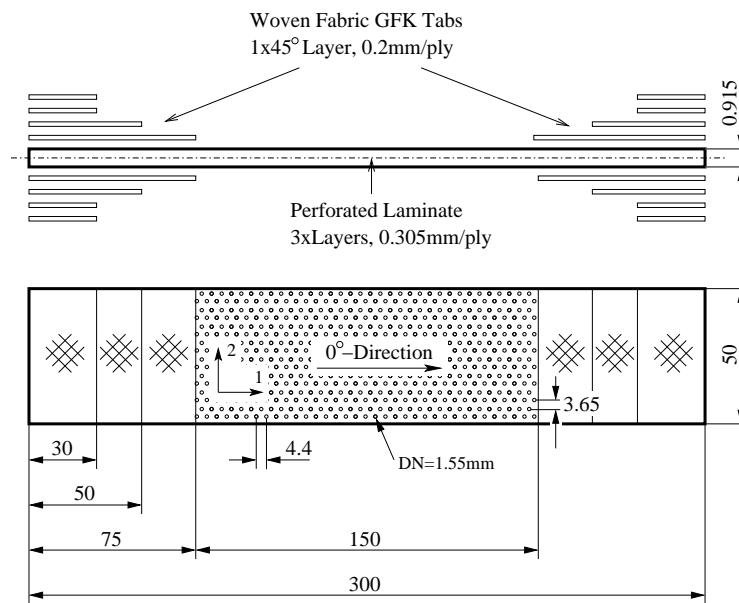


FIGURE 4.2: Geometry and layup of a perforated CFR woven fabric test coupon

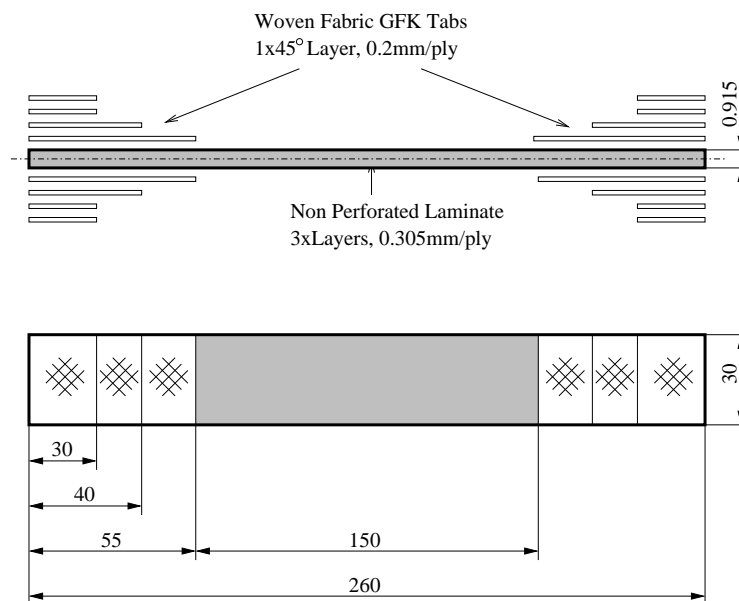


FIGURE 4.3: Geometry and layup of a non-perforated CFR woven fabric test coupon

4.2 Experimental Setup and Procedure

A 50 kN tensile/compression testing machine in combination with an acoustic emission monitoring system are used for the experimental investigations of the perforated and

non-perforated composite specimens. FIGURE 4.4 shows the test setup, and FIGURE 4.5 shows a detail of a clamped specimen. The three main parts of the test setup are:

1. Mechanical testing equipment (see TABLE 4.1)
2. Acoustic emission testing equipment (see TABLE 4.2)
3. Multi-sensor (see TABLE 4.1)

The two acoustic emission sensors are attached to the specimen at a distance of 15 mm from the tabs, where the distance between the two sensors is 120 mm. The sensors are outside the multi-sensors to reach a large sensor separation compared to the width of the test (see Section 2.4.3). For the strain measurements the multi-sensor distance (gage length) is 80 mm.

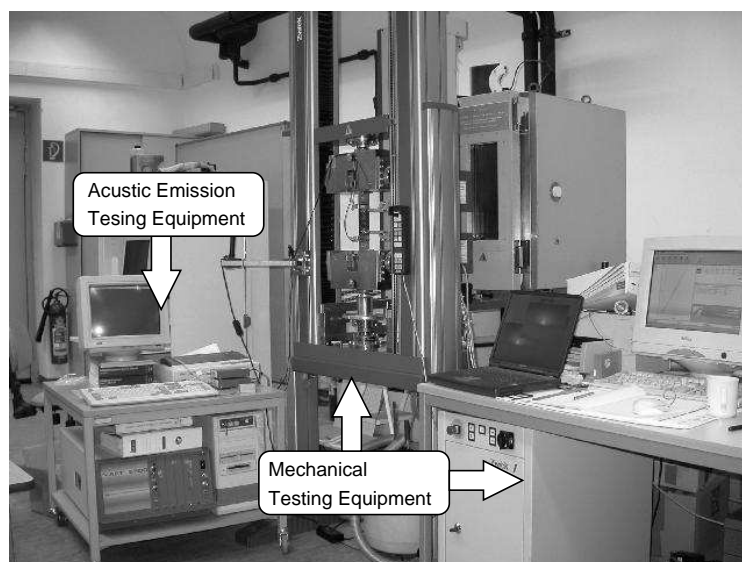


FIGURE 4.4: Test setup for stiffness and strength investigations of perforated and non-perforated laminates

The following test procedure is carried out: After the specimen is fixed in the grips, the acoustic emission sensors are attached, a pre-load of 200 N is applied, and the acoustic emission calibration procedure is performed (determination of the wave velocity of the tested laminate). In the strain-controlled loading step the displacement is increased at a constant crosshead speed of 5 mm/min. All acoustic emission events, the measured

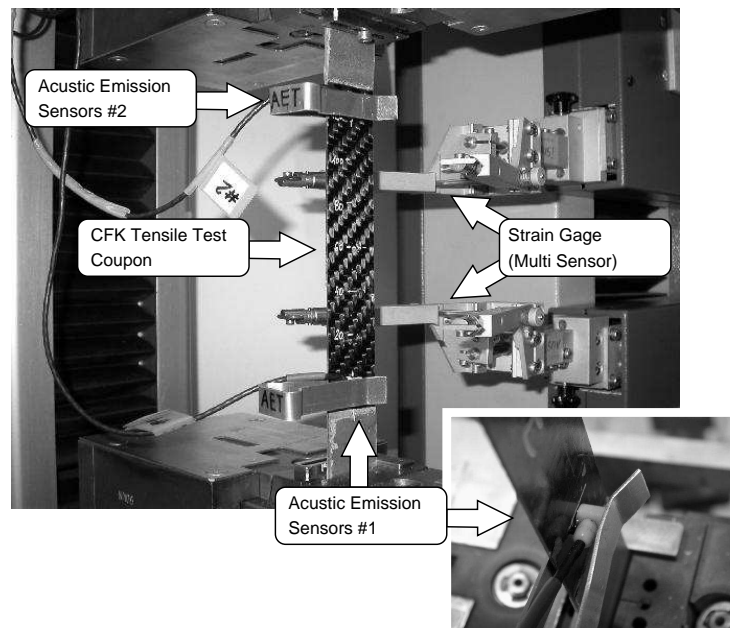


FIGURE 4.5: Detail of the test setup for the stiffness and strength investigations

TABLE 4.1: Specifications of the mechanical testing equipment and multi-sensor (strain gage)

Testing Machine	
Model	Zwick Z050/TH3A
Maximum Force	50 kN
Cross Head Speed	0.001 - 500 mm/min
Force Resolution	0.1 N
Strain Gage	
Model	Zwick Multi-sensor
Measure Range	10 mm - 740 mm
Accuracy	EN10002-4: Class 1
Resolution	0.2 μm

strain, and the applied load are recorded simultaneously as a function of time up to the ultimate load.

Tests are performed on various 2/2 twill weave CFR woven fabric laminates. A 2/2 twill weave is a weave that consists of one or more warp tows running over and under two fill tows. The result is a more pliable and drapable fabric than that produced by

TABLE 4.2: Specifications of the acoustic emission testing equipment

Mainframe	
Model	AET 5500 Monitoring System
Threshold	0.3 mA (automatic)
Main Amplifier	7.2 times Pre-amplification
Sensors	
Model	MAC 300 L
Resonant Frequ.	300 kHz
Pre-amplifier	
Model	AET 140B
Amplification	Gain: 40 dB
Filter	Flat frequency between 1 kHz and 2 MHz

either plain-weave or basket-weave, but not as pliable as satin. FIGURE 4.6 shows a 2/2 twill weave woven fabric laminate, as well as the smallest periodic part (unit cell).

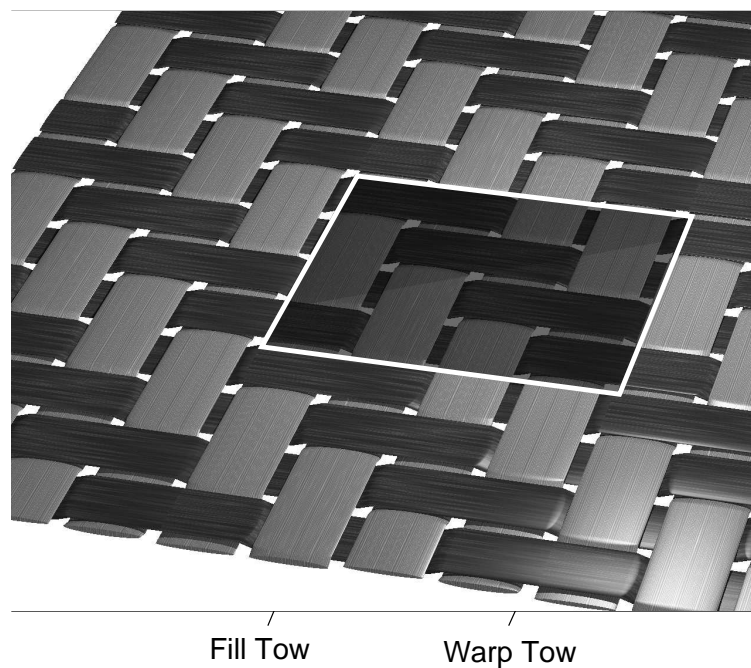


FIGURE 4.6: 2/2 twill weave woven fabric laminate

The investigated 2/2 twill weave CFR woven fabric laminates are listed in TABLE 4.3, where “cutting directions” refers to how the specimen is oriented relative to a global laminate coordinate system. The cutting directions and the coordinate system are shown

TABLE 4.3: Investigated 2/2 twill weave CFR woven fabric specimens

Lay-up	Type	Cutting Direction
[0/0/0]	non-perforated	0°
[0/0/0]	non-perforated	90°
[0/0/0]	non-perforated	45°
[0/45/90]	non-perforated	0°
[0/45/90]	non-perforated	90°
[0/45/90]	non-perforated	45°
[0/45/90]	perforated	0°
[0/45/90]	perforated	90°
[0/45/90]	perforated	45°

in FIGURE 4.7, where the global coordinate system and the unit cell coordinate system coincide.

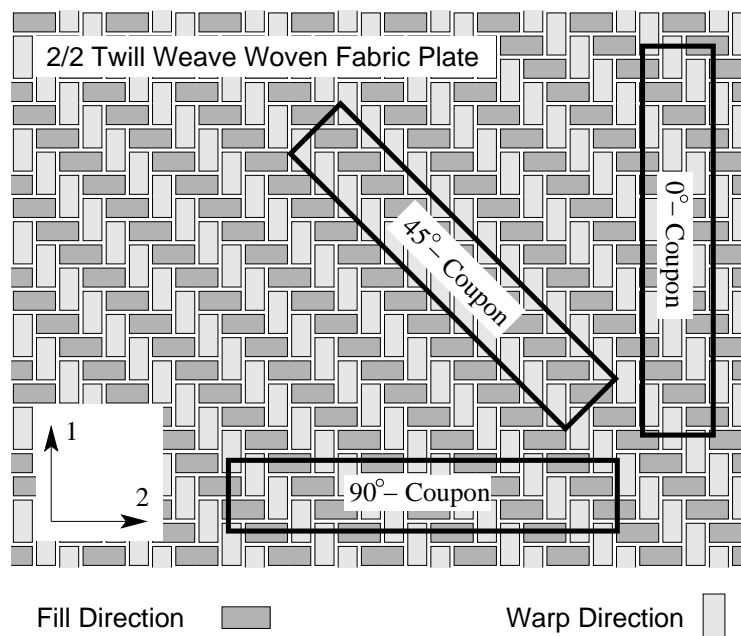


FIGURE 4.7: Cutting direction of 2/2 twill weave CFR woven fabric coupons

First, non-perforated [0/0/0] laminates are investigated to obtain single ply properties. Next, non-perforated [0/45/90] laminates are tested. These experimental results are compared to CLT results (see Section 4.3 and Section 4.4), which use the material values from the [0/0/0] test. Finally, perforated specimens are tested and compared in Section 5.5 to numerical results. At least six samples of carbon fiber reinforced woven fabrics laminates are tested for each test series (i.e., lay-up, type and cutting direction).

4.3 Stiffness Determination of Non-perforated and Perforated Laminates

In this section the focus is lied on the determination of the ply engineering moduli E_l , E_q , G_{lq} and effective engineering moduli $E_1 (=E_{0^\circ})$, $E_2 (=E_{90^\circ})$, G_{12} of a laminate. The Poisson number was not measured, because of the fact that reliable values can hardly be obtained for CFR woven fabric plies. The shear modulus G_{lq} is obtained from measurements on a tensile coupon cut under 45° from a composite plate by using Equation (4.1):

$$\frac{1}{E_\theta} = \frac{1}{E_l} \cos^4 \theta + \left(-\frac{2\nu_{lq}}{E_l} + \frac{1}{G_{lq}}\right) \sin^2 \theta \cos^2 \theta + \frac{1}{E_q} \sin^4 \theta, \quad (4.1)$$

where for $\theta = 45^\circ$ the modulus E_{45° is measured, and G_{lq} can be computed.

4.3.1 Gage Length Effect

The measured engineering moduli of a coupon may depend, among other things, on:

- Cross head speed
- Range of strains for the determination of the engineering moduli
- Gage length

The cross head speed is chosen to be constant with 5.0 mm/min, which corresponds to an internal fracture standard, which says that fracture has to occur within 60-90 seconds after the start of loading. Compared to ASTM D-3039M-00, where the cross head speed is suggested as 0.5 mm/min, the speed used is ten times higher. For the current application the fracture standard seems to be more suitable.

The lower and the upper strains for the modulus determination are 0.1 and 0.5 %, respectively, where the material behavior is approximately linear up to a strain of 0.5 %. The maximum strain value correspond to a typical strain allowable in the aerospace industry. The lower end of the strain range is necessary due to non-linear effects of the used wedge grips at low loads.

A very important parameter is the strain gage length. Therefore, experimental investigations are done on two different perforated [0/45/90] tensile test coupons, where the gage length is varied between 10 and 100 mm in steps of at least 5 mm. The tests are performed twice at each measuring point. Two experiments are done on each coupon, where the coupon is slightly moved in the width direction by approximately half a unit cell length after the first measurements from 10 - 100 mm. The test setup for studying the influence of the gage length is shown in FIGURE 4.8. During these investigations the perforated tensile coupon is not destroyed and is subjected to strains between 0.1 and 0.5 %.

The experimental results are shown on the left hand side of FIGURE 4.9 and FIGURE 4.10. In both pictures a large error appears for a gage length less then 50 mm. Obviously, the error increases when the gage length decreases. In order to show that the source of this error comes mainly from the violation of the homogenization assumptions (i.e., the macro scale have to be much larger than the micro scale), 3D unit cell calculation are performed (as described in Section 5.5), and the numerical computed engineering moduli in dependence of the gage length are obtained. The results are shown on the right hand side of FIGURE 4.9 and FIGURE 4.10, where in both cases the true size, the measuring line (Line A), and the orientation of the unit cells are sketched, too. The numerical calculations are performed along the Line A on discrete nodal points. Very good agreement and explanation of the measuring error is found. It can be seen that the strain gage length has to be at least 50 mm (which is approximately 10 - 15 times the length of a unit cell) in order to get reliable results for the engineering moduli.

It can also be seen in FIGURE 4.9 and FIGURE 4.10 that for some measuring points with a gage length less than 50 mm show a very good agreement with the effective engineering moduli. This behavior can be explained by the fact, that the measurements give the effective engineering moduli if the gage length is a multiple of a unit cell length or if it is large in comparison with the unit cell length.

In the current investigations we choose a strain gage length of 80 mm, where at least 18 unit cells are within the gage length. Numerical calculations along a line between the

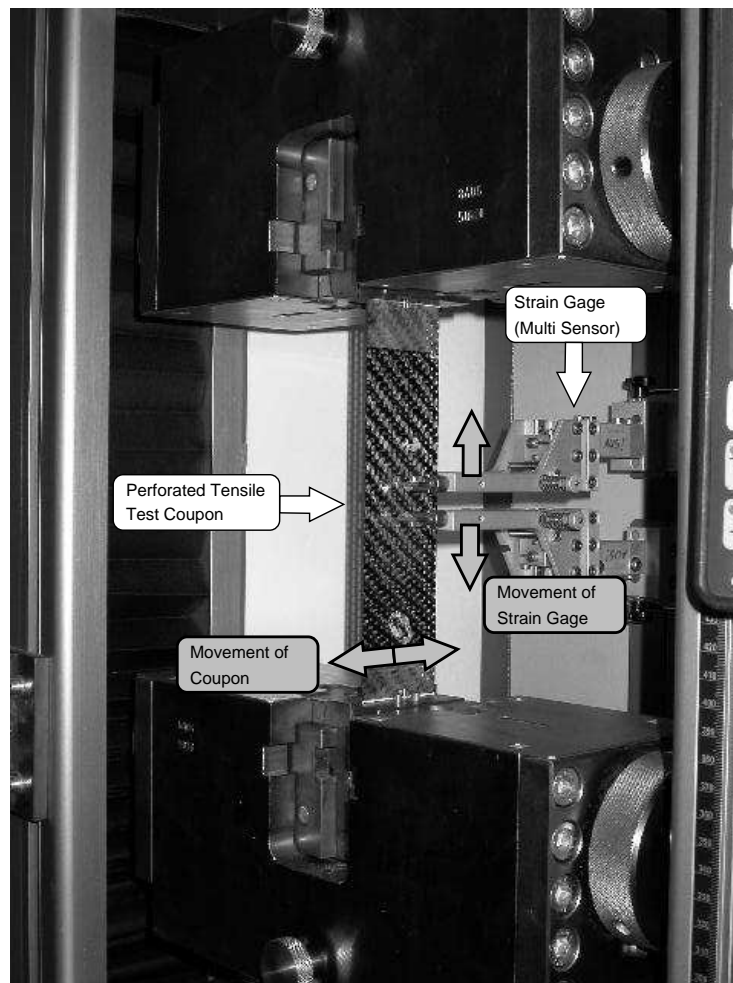


FIGURE 4.8: Test setup for the measurement up the gage length influence

holes (Line B in FIGURE 4.11) give much smaller errors. Therefore, they are not shown in FIGURE 4.9 and FIGURE 4.10.

The explanation for the homogenization error is given in FIGURE 4.11. The figure on the top shows the periodic and homogenized displacements within a unit cell, as well as the sum of both displacements, which corresponds to Equation (3.36), where it is assumed that the displacement field of a homogenized media can be split into two parts, a periodic (fluctuating) and a constant part. If the strains are computed from these displacement fields, they fluctuate also (FIGURE 4.11 bottom), where the amplitude of the fluctuation becomes smaller with an increasing strain gage length. For large gage length the strains approach to constant homogenized strain. These numerical results

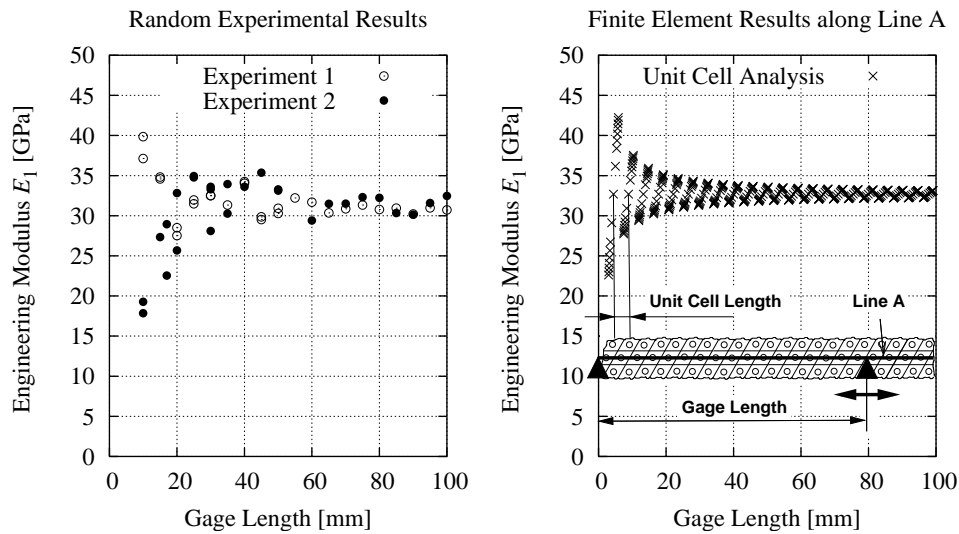


FIGURE 4.9: Comparison of experimentally (left) and numerically (right) obtained engineering moduli E_1 in dependence of the gage length

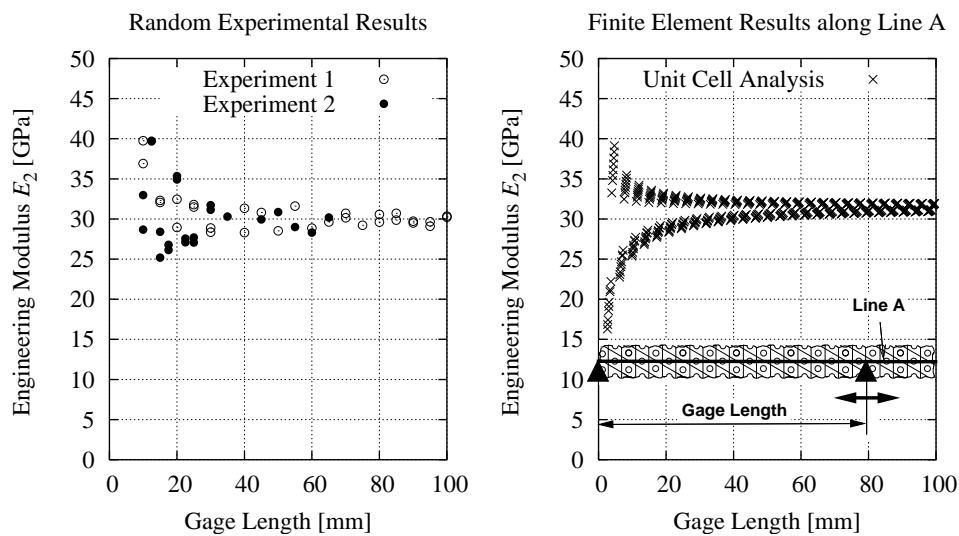


FIGURE 4.10: Comparison of experimentally (left) and numerically (right) obtained engineering moduli E_2 in dependence of the gage length

explain the large tested errors in determining engineering moduli by using low strain gage lengths.

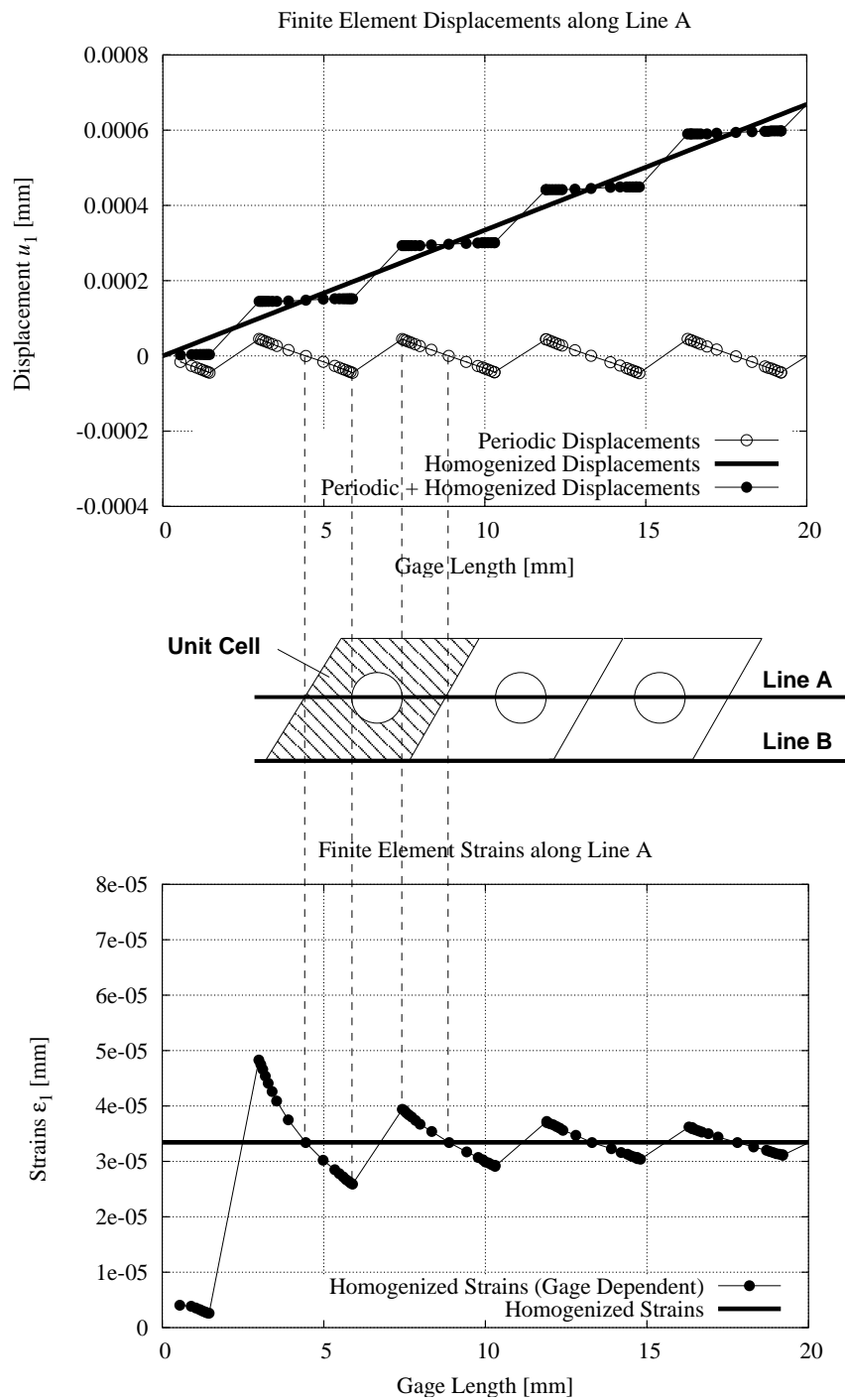


FIGURE 4.11: Homogenized and periodic displacements, as well as sum of both (top). Local gage dependent and homogenized strains (bottom)

4.3.2 Measured Stiffness of Non-perforated Laminates

The obtained effective engineering moduli for the non-perforated specimens are shown in TABLE 4.4, s_E is the standard deviation. The shear modulus is obtained from Equation (4.1), where the Poisson number of the ply is taken from previous tests (Pahr [2000]) as 0.03.

TABLE 4.4: Measured effective engineering moduli of a [0/0/0] and a [0/45/90] non-perforated CFR woven fabric laminate

Lay-up	Cutting Direction	E (GPa)	s_E (GPa)	G (GPa)
0/0/0	0°	59.78	3.0	
0/0/0	90°	61.02	1.9	
0/0/0	45°	14.3	0.7	3.98
0/45/90	0°	47.92	1.2	
0/45/90	90°	48.45	1.8	
0/45/90	45°	36.38	1.0	13.03

The effective stiffness values for the [0/45/90] laminate in TABLE 4.4 should be obtainable from the [0/0/0] stiffness values using Classical Lamination Theory (CLT), where in the case of a [0/0/0] laminate $E_1 = E_l$, $E_2 = E_q$, and $G_{12} = G_{lq}$. A comparison of these stiffness values is shown in FIGURE 4.12 and denoted as “Test” and “0/0/0+CLT”, respectively. Additionally, modified stiffness results are also shown in FIGURE 4.12 (denoted as “mod. 0/0/0+CLT”) which are discussed later. In FIGURE 4.12 three different values for the engineering moduli are compared. The white bars are the engineering moduli based on tests of [0/45/90] laminates, where the error-bars correspond to the standard deviation. The light gray bars use tested moduli from a [0/0/0] laminate, where the stiffness of the [0/45/90] laminate is calculated by using CLT. It is evident that the effective Young’s moduli of the laminate, E_1 and E_2 , are overestimated, whereas the shear modulus of the laminate G_{12} is underestimated by the CLT results. The CLT results are, especially in the case of the modulus E_1 , outside the error-bars. Hence, this error can not be explained by the standard deviation only.

A possible explanation is based on geometrically non-linear bending-stretching effects as shown in FIGURE 4.13. On this point it is emphasized that also other effects might affect the engineering moduli. Only detailed 3D unit cell analyses of woven fabrics on the meso-scale (modeling of roving/tows in matrix material) can verify the fol-

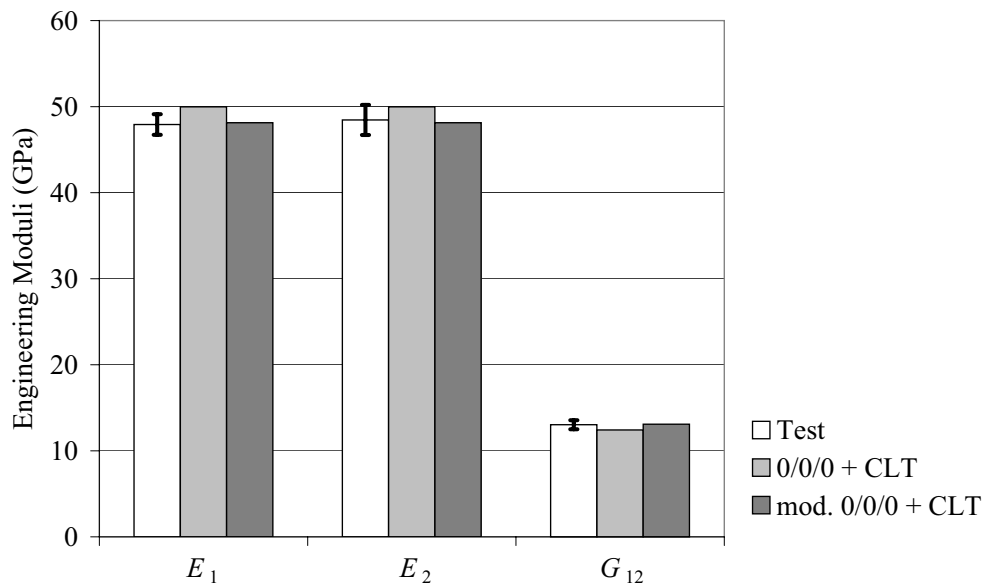


FIGURE 4.12: Comparison of effective engineering moduli of a [0/45/90] CFR woven fabric laminate: Obtained from tests, from experiments on [0/0/0] laminates in combination with CLT, and from modified [0/0/0] laminate values

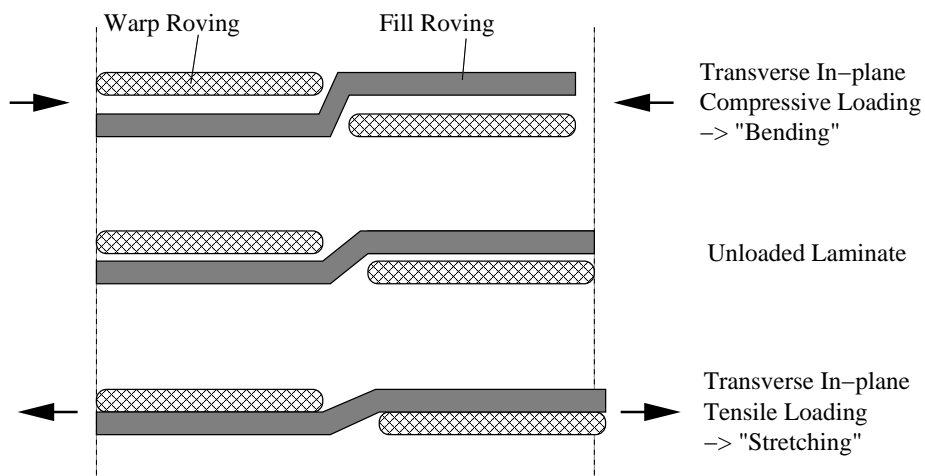


FIGURE 4.13: Bending-stretching effects of woven fabric laminates

lowing assumptions and/or make other effects visible. These studies are not done in this work. Furthermore, studies explaining the above measured effect are not found in the literature.

In FIGURE 4.13 a cross section of a generic woven fiber composite can be seen. The top picture shows the bending of the fill tow, and the bottom picture shows the stretching of the same tow. These effects mainly come from the transverse in-plane loading of the load bearing layers. It is believed that these geometrically non-linear effects, beside others, are responsible for the influence on the Young's moduli and shear modulus, which can be explained as follows:

1. In our case the stretching of the tow mainly influences (increases) the shear modulus, because the ratio of the transverse in-plane tensile stresses to the shear stresses is higher in the case of a [0/45/90] laminate than in a [0/0/0] laminate. For example, $\sigma_{ll}/\sigma_{lq}=1$ for a [0/0/0] tensile coupon cut under 45° and $\sigma_{ll}/\sigma_{lq}=2.27$ for the two outside layers of a [0/45/90] laminate also cut under 45°. The two outside layers (which lie under 45° to the loading direction in the case of a laminate cutted under 45°) are mainly responsible for the measured modulus (E_{45}) and, therefore, for the effective shear stiffness. That is, tow stretching increases the shear modulus. Thus, the effective shear modulus of a [0/45/90] laminate in FIGURE 4.12 is higher than the calculated effective shear modulus obtained from the tests of a [0/0/0] laminate by using CLT.
2. The bending of the tows in this special case influences (decreases) the Young's moduli, because transverse in-plane compressive stresses are evident in the 0° and 90° layers of a [0/45/90] coupon (cut under 0° or 90°). These stresses are zero for a [0/0/0] laminate under 0° and 90° loading. That is, tow bending decreases the Young's moduli. Thus, the measured Young's moduli (E_1 and E_2) of a [0/45/90] laminate are smaller than those obtained from CLT.

These two statements can also be understood from the engineering point of view. Tow bending in general helps, in the case of longitudinal tensile stresses and transverse in-plane compressive stresses within a layer, the elongation in longitudinal direction. For shear stresses in the presence of longitudinal and transverse in-plane tensile stresses (stretching in two directions) it can be visualized that the shearing is more constrained if the tensile stresses are higher. Furthermore, effects of adjacent plies might play a role and, additionally, increase or decrease the effective engineering moduli.

The question arises at this point of how the ply material parameters would have to be modified to obtain the effective material behavior of a [0/45/90] laminate from CLT. The dark gray bars in FIGURE 4.12 show these results with slightly modified engineering

moduli for a ply. A very good agreement with the tested moduli (white bar) appears. The tested and modified in-plane engineering moduli of the [0/0/0] laminate are shown in TABLE 4.5, where these results go hand in hand with the above bending-stretching considerations.

TABLE 4.5: Measured and modified non-perforated engineering moduli of a CFR woven fabric ply used for investigations of non-perforated [0/45/90] woven laminates

Parameter	Tested	Modified
E_l (GPa)	59.78	57.0
E_q (GPa)	61.02	57.0
G_{lq} (GPa)	3.98	5.8
ν_{lq} (GPa)	0.03*	0.03*

* ... taken from previous tests

Finally it should be remarked that the Young's moduli depend on the ratio σ_{qq}/σ_{ll} and the G -modulus is influenced by the ratio σ_{ll}/σ_{lq} . Strictly speaking the effective material parameters are only valid for one lay-up and topology, i.e., if the laminate is perforated the above ratios are different and the individual plies behave differently. Practically, this effect cannot be taken into account. However, in this work these effects are not neglected but other modified ply material values for the perforated laminate are used as presented in the following.

4.3.3 Measured Stiffness of Perforated Laminates

The tested effective stiffness values of the perforated [0/45/90] laminate are summarized in TABLE 4.6. A considerable decrease of the moduli is apparent if the values

TABLE 4.6: Measured effective engineering moduli of a perforated [0/45/90] CFR woven fabric laminate

Lay-up	Cutting Direction	E (GPa)	s_E (GPa)	G (GPa)
0/45/90	0°	31.04	1.28	
0/45/90	90°	29.81	1.30	
0/45/90	45°	22.56	0.55	8.06

are compared to the moduli of the non-perforated composite in TABLE 4.4. A graphic

comparison of the measured effective engineering moduli of the [0/45/90] CFR woven fabric laminate is shown in FIGURE 4.14. There, it can be seen that the perforations degrade the stiffness significantly. The measured effective engineering moduli of the perforated laminate are approximately 62 - 65 % of the measured effective engineering moduli of the same non-perforated material. This drop down is substantial compared to the non-perforated area, which is 88.4%, for the investigated perforated laminate. In this case the area fraction (88.4%) and the volume fraction of the perforated laminate are equal. Thus, the above results show that the rule of mixture (ROM) cannot be applied for stiffness predictions of perforated laminates.

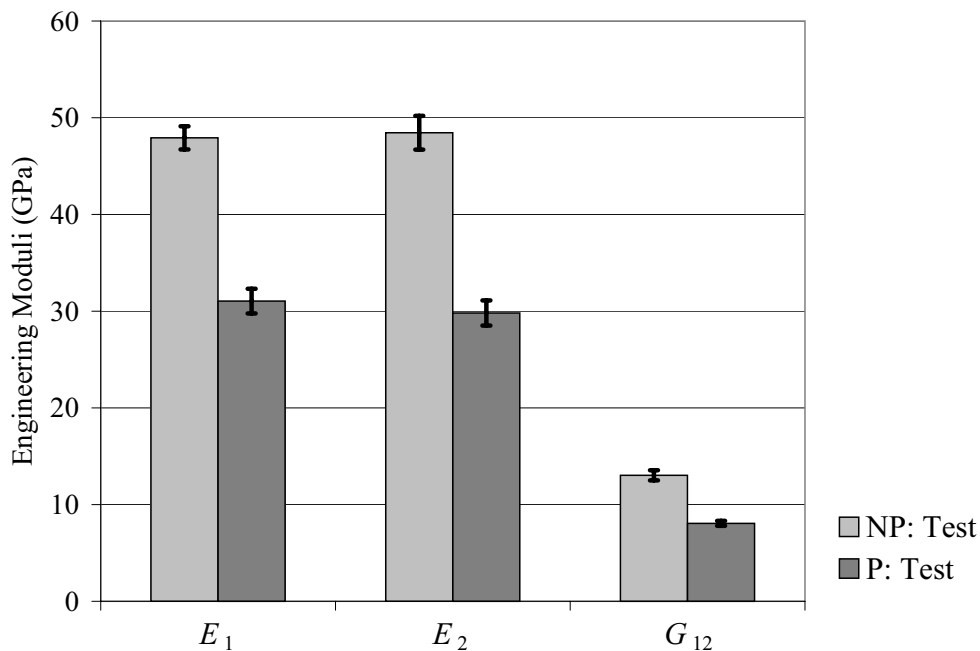


FIGURE 4.14: Comparison of measured effective engineering moduli of a non-perforated and a perforated [0/45/90] CFR woven fabric laminate

For the unit cell analysis ply material parameters are needed. The modified moduli in TABLE 4.5 cannot be used directly. The reason for this is explained in Section 4.3.2. A possible evaluation procedure is given TABLE 4.7 and in TABLE 4.8. There, in both tables the effective engineering moduli of the non-perforated [0/45/90] laminate are taken from TABLE 4.5. The engineering moduli for the non-perforated [0/0/0] laminate are based on test results (TABLE 4.4), where the the Young's moduli are averaged over the 0° and 90° -direction. The ratios σ_{ll}/σ_{lq} and σ_{qq}/σ_{ll} are computed with CLT. In TABLE 4.7 the

TABLE 4.7: Evaluation of the shear modulus for various σ_{ll}/σ_{lq} ratios of CFR woven fabric laminates

Lay-up	Loading	Influencing Param.	G (GPa)
NP-0/45/90	Tensile 45°	$\sigma_{ll}/\sigma_{lq} = 2.27$	5.8
NP-0/0/0	Tensile 45°	$\sigma_{ll}/\sigma_{lq} = 1.00$	3.98
NP-0/0/0	Pure Shear	$\sigma_{ll}/\sigma_{lq} = 0.00$	2.55

shear modulus for pure shear loading is obtained by a simple linear regression. This is based, as mentioned above, on the assumption that only the σ_{ll}/σ_{lq} ratio influences the shear modulus and that the influence depends linearly on the σ_{ll}/σ_{lq} ratio. These results show that the shear modulus may lie between 2.55 and 5.8 GPa in the perforated case and depends strongly on the ratio σ_{ll}/σ_{lq} . Therefore, a mean value of 4.0 GPa is chosen for the shear modulus in all unit cell calculations. A validation of this assumption is carried out in Section 5.5.3. In TABLE 4.8 the ratio σ_{qq}/σ_{ll} for the third lay-up is obtained

TABLE 4.8: Evaluation of the modified Young's modulus of a perforated [0/0/0] CFR woven fabric laminate

Lay-up	Loading	Influencing Param.	E (GPa)
NP-0/45/90	Tensile	$\sigma_{qq}/\sigma_{ll} = 0.153$	57.0
NP-0/0/0	Tensile	$\sigma_{qq}/\sigma_{ll} = 0.000$	60.4
P-0/45/90	Tensile	$\sigma_{qq}/\sigma_{ll} = 0.127$	57.6

from CLT with effective single ply stiffness values from a unit cell analysis. Finally, the modified engineering moduli for the perforated laminate are summarized in TABLE 4.9.

TABLE 4.9: Modified engineering moduli of a non-perforated CFR woven ply used for investigations of perforated [0/45/90] laminates

Parameter	Modified
E_l (GPa)	57.6
E_q (GPa)	57.6
G_{lq} (GPa)	4.0
ν_{lq} (GPa)	0.03*

* ... taken from previous tests

4.4 Strength Determination of Non-perforated and Perforated Laminates

Comparison of Measured FPF and Ultimate Strength Values

TABLE 4.10 shows a summary of the measured effective non-perforated and perforated first ply failure strengths, the ultimate strengths, and the corresponding standard deviations. The evaluation procedures and comparisons of the individual test results are

TABLE 4.10: Experimental effective strength values in MPa of non-perforated and perforated [0/0/0] and [0/45/90] CFR woven fabric laminates

Lay-up	Cutting Dir.	Type	R_{FPF}	s_{FPF}	R_{ult}	s_{ult}
0/0/0	0°	non-perforated	445	22	609	25
0/0/0	90°	non-perforated	460	10	638	15
0/0/0	45°	non-perforated	145	9	210	11
0/45/90	0°	non-perforated	310	27	495	15
0/45/90	90°	non-perforated	340	12	471	11
0/45/90	45°	non-perforated	195	33	407	7
0/45/90	0°	perforated	155	12	289	17
0/45/90	90°	perforated	155	10	254	22
0/45/90	45°	perforated	87	5	206	6

given in the following, where the effective strengths are denoted with R_{0° , R_{90° , and R_{45° for tensile test coupons cut under 0°, 90°, and 45°, respectively.

A bar chart of the strength values listed in TABLE 4.10 is shown in FIGURE 4.15. The reduction in the FPF strength and ultimate failure strength due to the perforation is 45.6 to 50.0% and 50.6% to 58.4 %, respectively, for the various loading directions. The reductions in strength are higher than the stiffness reduction shown in Section 4.3.3. It should be remarked again that a perforation area of only 11.6% leads to a strength decrease of approximately 50%!

The ratios of first ply failure to ultimate failure strength values of the perforated and non-perforated laminate are shown in FIGURE 4.16. On one hand it can be seen that the ratio is less in the non-perforated case than in the perforated case. On the other hand a significant difference between the FPF strength values and the ultimate strength values

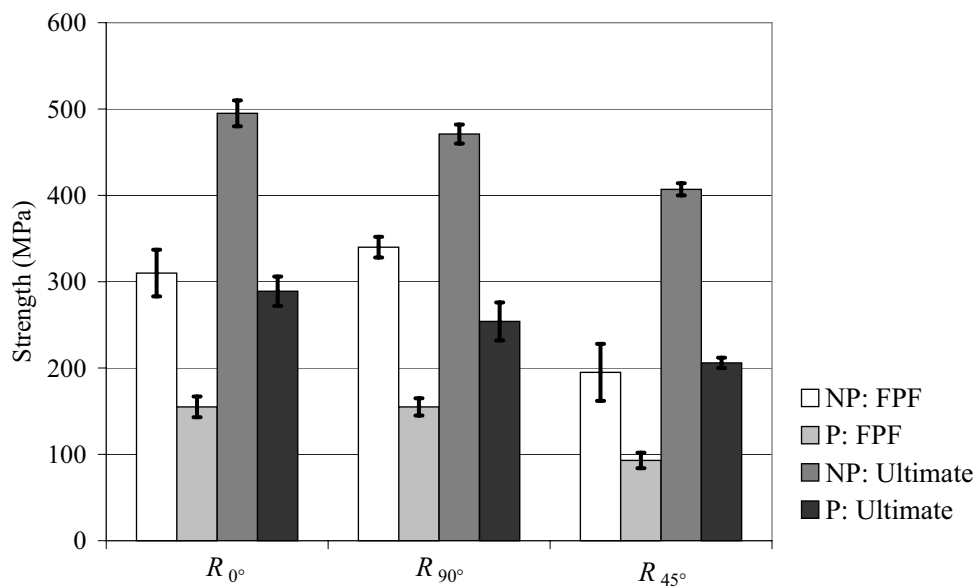


FIGURE 4.15: Comparison of tested first ply failure strengths and ultimate failure strengths of non-perforated and perforated [0/45/90] CFR woven fabric laminates

is evident, where the difference lies between 45 and 72%.

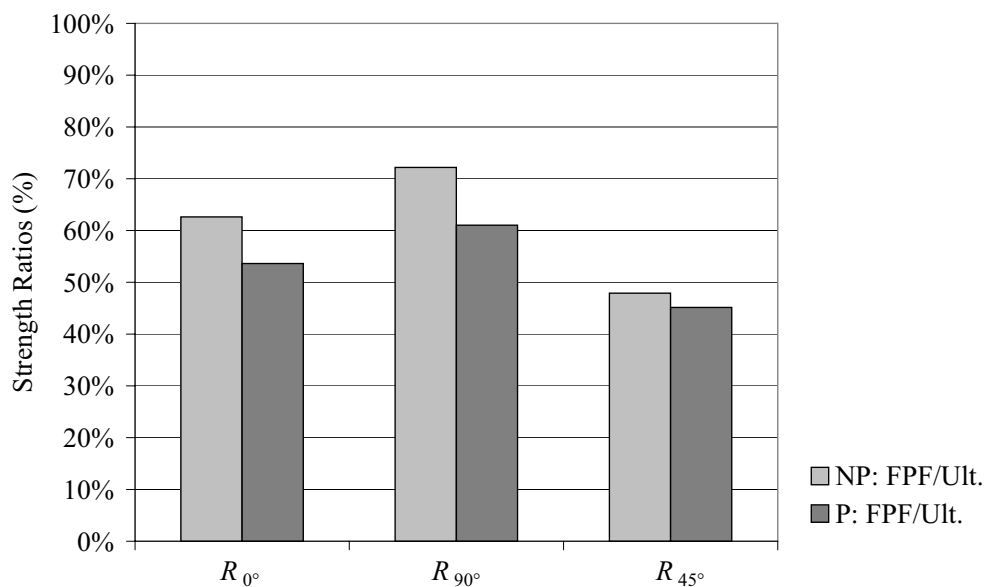


FIGURE 4.16: Difference of tested first ply failure strengths and ultimate failure strengths of non-perforated and perforated [0/45/90] CFR woven fabric laminates

Determination of First Ply Failure Strength Values from AE Results

The first ply failure strengths are obtained from acoustic emission measurements. Typical acoustic emission results are shown in FIGURE 4.17, FIGURE 4.18, and FIGURE 4.19 for the non-perforated [0/0/0], the non-perforated [0/45/90], and the perforated [0/45/90] CFR woven fabric laminate, respectively. The two top pictures in each figure are related to coupons cut under 0° , for the two pictures in the center the coupons are oriented at 90° , and the two bottom pictures are based on tests of coupons cut at 45° from a laminated CFR woven fabric plate (see FIGURE 4.7). On the left hand side the stress-strain curves, the events, and the logarithm of the sum of all events are plotted. In these figures arrows show the strain level where first ply failure starts within the specimens. Single events are disregarded, i.e., the start of first ply failure is reached when approximately 5-10 events occur within a time window of one second. The first ply failure values in FIGURE 4.17, FIGURE 4.18, and FIGURE 4.19 are slightly different from that in TABLE 4.10, because the strength values in TABLE 4.10 are the mean value of six test series. The pictures on the right hand side of FIGURE 4.17, FIGURE 4.18, and FIGURE 4.19 show the peak amplitude over the applied stress. These figures are also well suited for the determination of the first ply failure strength, where in this case the first ply failure strengths are obtained directly.

Comparison of Tested and Computed FPF Strength values for Non-perforated Laminates

A comparison of measured and computed first ply failure strengths of a non-perforated [0/45/90] CFR woven fabric laminate is shown in FIGURE 4.20. The error-bars of the measured strength values correspond to the standard deviation. The computed strengths are based on various failure theories (Tsai-Wu, Tsai-Hill, and maximum stress), where in the case of the Tsai-Wu criterion the interaction parameter K is chosen as 0.0 and -0.5 and the difference of the predicted strength values is indicated with error-bars. The FPF strength values of the single ply are taken from the test of the [0/0/0] laminate, where $R_{ll}^{(+)}$ and $R_{qq}^{(+)}$ are averaged, and the mean value is taken. A large scatter of the predicted and measured strength values is visible, and it is evident that the strength predictions can differ considerable if the same input parameters are used for each failure criterion.

The errors of the various numerically obtained results compared to the measured

values are shown in TABLE 4.11. The Tsai-Hill criterion underestimates the FPF strength

TABLE 4.11: Error of numerically obtained first ply failure strengths of a non-perforated [0/45/90] CFR woven fabric laminate

Tsai-Hill	Tsai-Wu $K=-0.5$	Tsai-Wu $K=0.0$	Max. Stress
-8.4%	4.8%	14.5%	23.2%
-16.5%	-4.4%	4.4%	12.4%
-17.9%	2.6%	21.0%	48.7%

of the laminate, whereas the Tsai-Wu criterion with $K=0.0$ and the maximum stress criterion overestimate the FPF strength. The Tsai-Wu criterion with $K=-0.5$ is identified as the most accurate one for FPF strength prediction for this material system, the error being less than 4.8% for all cases studied.

Fracture Patterns of Perforated and Non-perforated Laminates

The fracture patterns of a non-perforated and a perforated coupon are shown in FIGURE 4.21. It can be seen that all possible failure modes, which mainly come from the nature of a woven fabric laminate, are active. In the case of the non-perforated coupon the macro-crack runs perpendicularly to the loading direction. The middle layer (45° layer) is pulled out for some millimeters. The crack path in the perforated specimen is different from that of the non-perforated laminate. There, the crack “jumps” from hole to hole, and a zigzag fracture line is visible. Furthermore, the tow pull out of the 45° layer is less pronounced than in the previous case. Finally, it should be mentioned that, based on these fracture patterns, no reliable statements regarding the first ply failure mode can be given, because a complex progressive damage process follows the first ply failure mode, and the visible ultimate failure modes may be totally different from the FPF modes.

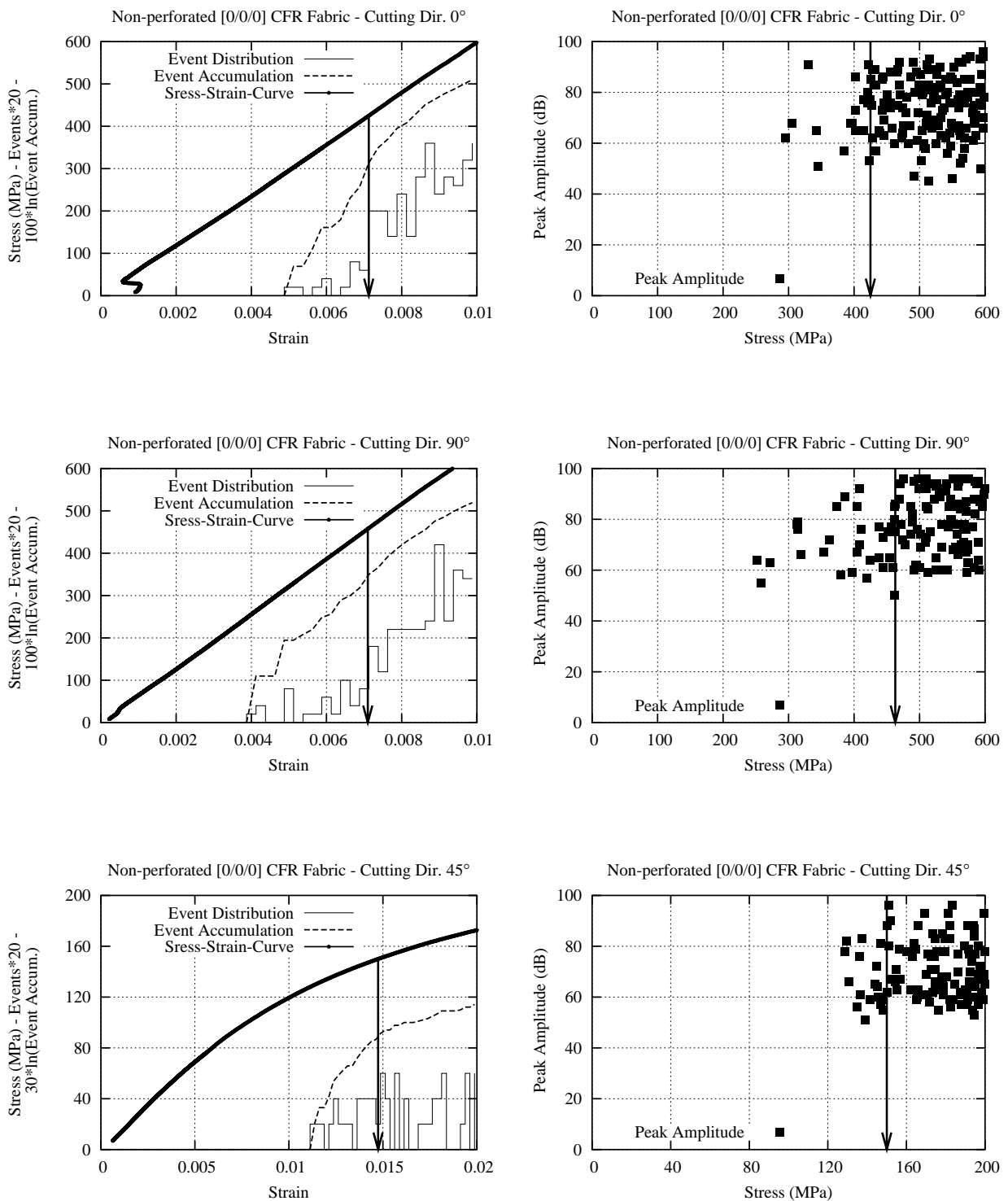


FIGURE 4.17: Acoustic emission results for a non-perforated [0/0/0] CFR woven fabric laminate. The cutting direction is 0° (top), 90° (center), and 45° (bottom)

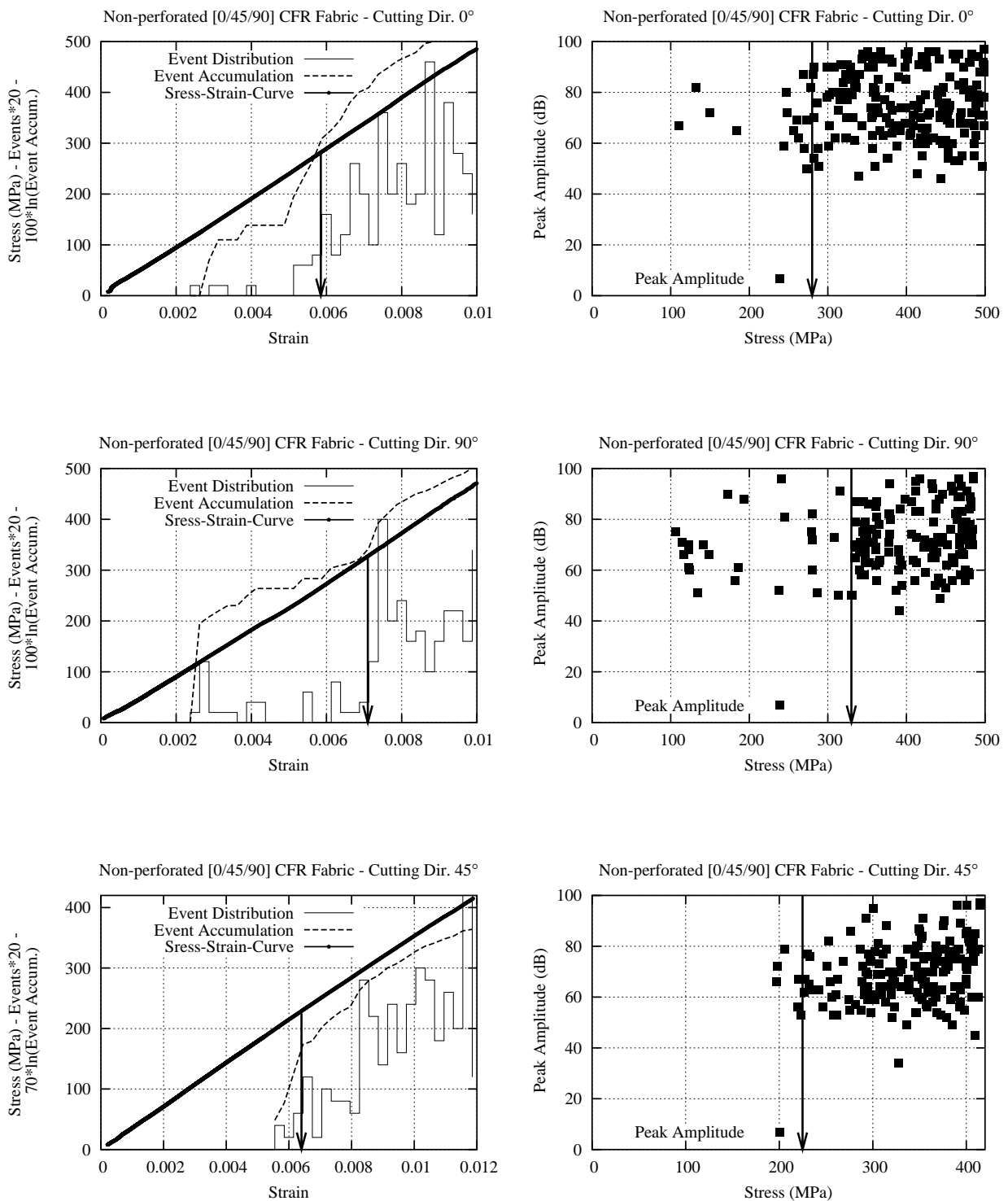


FIGURE 4.18: Acoustic emission results for a non-perforated [0/45/90] CFR woven fabric laminate. The cutting direction is 0° (top), 90° (center), and 45° (bottom)

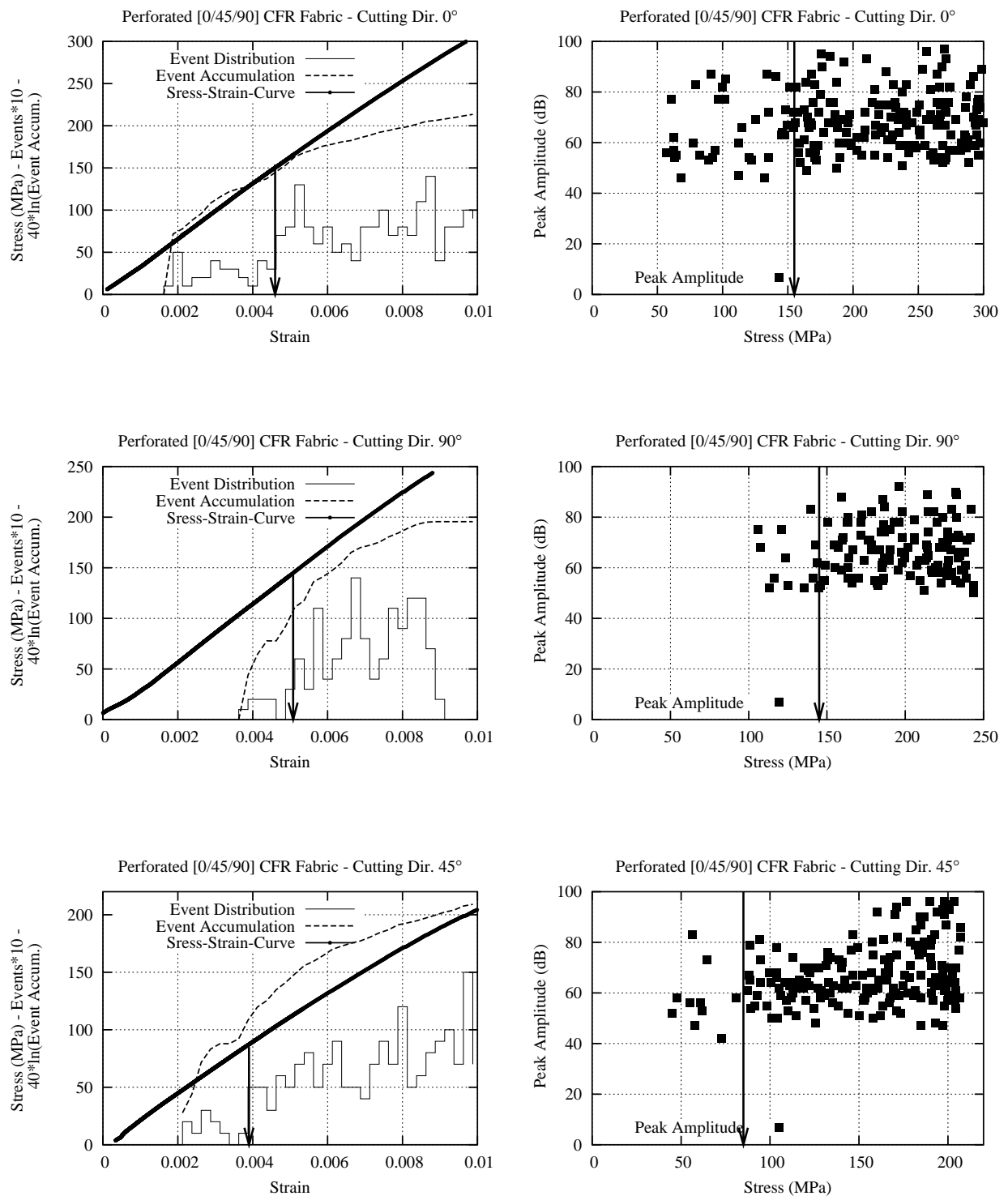


FIGURE 4.19: Acoustic emission results for a perforated [0/45/90] CFR woven fabric laminate. The cutting direction is 0° (top), 90° (center), and 45° (bottom)

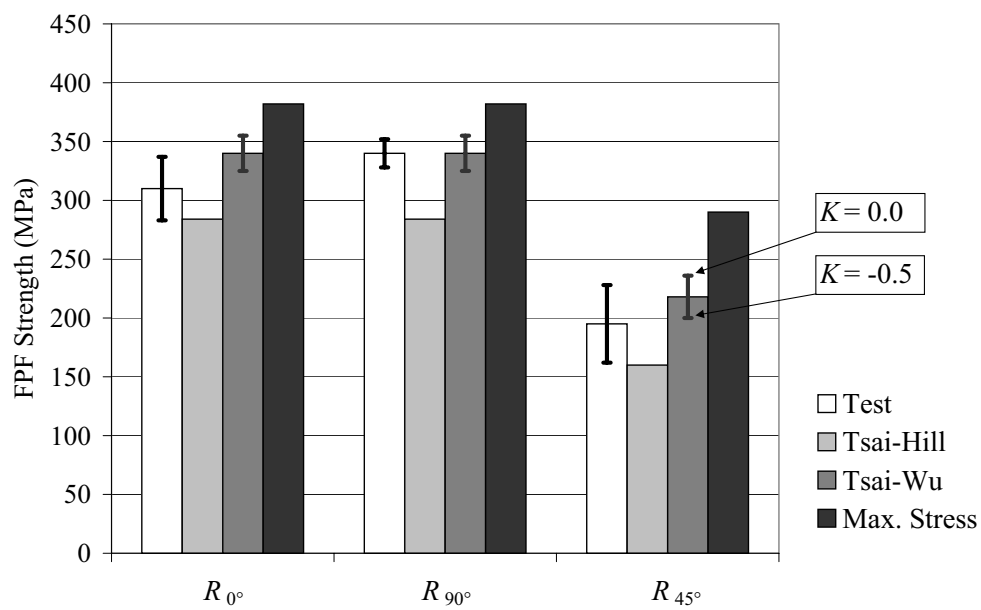


FIGURE 4.20: Comparison of measured first ply failure strengths of a non-perforated [0/45/90] CFR woven fabric laminate with predictions from various failure theories

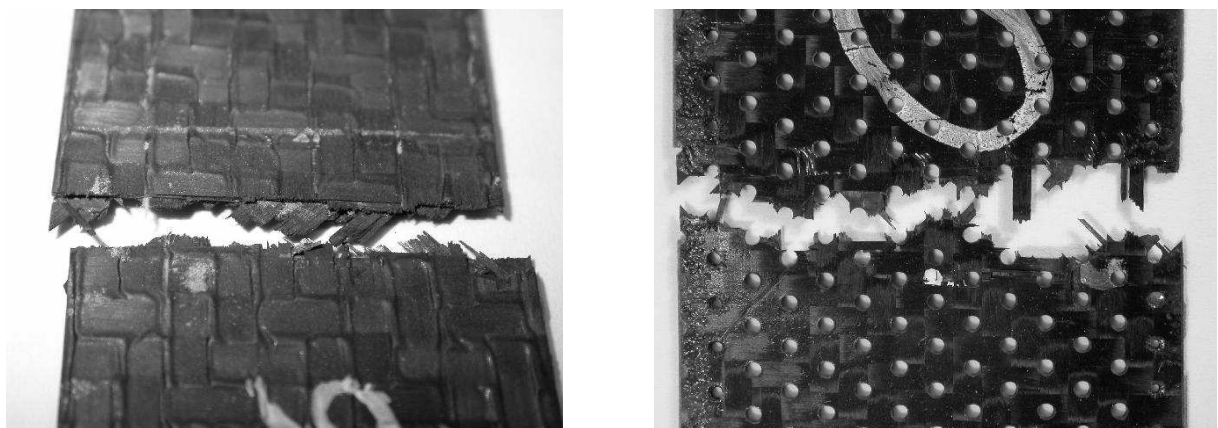


FIGURE 4.21: Typical fracture patterns of non-perforated (left) and perforated (right) CFR [0/45/90] woven fabric coupons

4.5 Determination of Inter-laminar Shear Strength

Delamination (the failure at the interface between different layers) is one of the most critical failure mechanisms of laminates. The resistance against delamination is characterized by the inter-laminar shear strength (ILSS). The inter-laminar shear strength is defined as the shear stress at failure where the plane of fracture is located between the layers of reinforcement of a composite structure (ASTM D 3846-94). Different experimental arrangements have been established for estimating the ILSS of anisotropic materials or material combinations. The most common methods for the determination of the ILSS are the short-beam-shear test (ASTM D-2344-00), the four-point shear test, the Iosipescu test (ASTM D-5379-98), the tensile test (ASTM D-3518-94), and the double notch shear test (ASTM D-3846-94). A new apparatus for the determination of the ILSS of flat and curved composite material is the compression shear device (CSD) (see Rosselli and Santare [1997], Schneider et al. [2001]).

An important contribution to an assessment of the three-dimensional material properties could be a testing method for the ILSS, which allows to measure the static ILSS, as well as the fatigue strength under inter-laminar stresses. The above mentioned Iosipescu test method has been examined extensively and was found to be a highly effective and reliable method for predicting the static ILSS (Adams and Lewis [1997], Schneider et al. [2001]). However, measuring the fatigue strength by this method is difficult.

Unlike the Iosipescu shear test, the double notch shear test method does not require an extensive set-up or fixture, the specimen geometry is simple, and investigations of the fatigue strength can be performed (Shokrieh and Lessard [1998]). One of the drawbacks of the double notch (single-lap) shear test is the bending moment created by the unsymmetric specimen shape. Clamps are used to eliminate this unwanted loading, but this fixation might have an influence on the measured ILSS. Therefore, another notched ILS-specimen, the so-called double-lap-shear (DLS) specimen, was introduced (FIGURE 4.23), which has a symmetric shape and, therefore, avoids the above drawback (Rosenkranz et al. [2001]).

This section presents investigations of the DLS specimen and its suitability for an accurate assessment of the static ILSS. Based on these results it can be decided whether or not the DLS-method is appropriate for fatigue strength predictions. Results obtained from the double-lap-shear test are compared to those obtained from the short-beam-shear test. Many investigators discussed the SBS-method (e.g., Adams and Lewis [1995],

Adams and Lewis [1997], Schneider et al. [2001]) and described certain problems with the determination of the ILSS. The SBS-method is reviewed as well, and found to be suitable (in combination with simple finite element calculations) to predict upper and lower bounds for the true ILSS. Such bounds are especially useful for establishing the quality of a new ILSS test method.

The double-lap-shear specimen is investigated numerically and experimentally. The first delamination failure loads (FDF-loads) are determined from acoustic emission experiments. The FE-analyses are based on these FDF-loads and the local (real) ILSS is finally obtained by applying a fitting procedure.

4.5.1 Standardized Shear Strength Evaluation

The standardized evaluation of the inter-laminar shear strength is based on ultimate loads F_{ult} . The inter-laminar shear strength is calculated from F_{ult} according to ASTM D2344-00 for the SBS-specimen

$$(R_{31}^{\text{IL}})_{\text{exp}}^{\text{SBS}} = \frac{3F_{\text{ult}}}{4bt}, \quad (4.2)$$

(where a parabolic shear stress distribution over the beam thickness is assumed). t is the beam thickness and b the width of the SBS-specimen. In the case of the DLS-specimen the ILSS-values are obtained from:

$$(R_{31}^{\text{IL}})_{\text{exp}}^{\text{DLS}} = \frac{F_{\text{ult}}}{2bL}, \quad (4.3)$$

where $2bL$ is the overlapping area. This formula is similar to the standardized ILSS-evaluation for a “single-lap-shear”-specimen (based on ASTM D-3846-94) where the overlapping area is equal to bL .

4.5.2 Finite Element Analysis

The geometry of the SBS- and the DLS-specimens is shown in FIGURE 4.22 and FIGURE 4.23, respectively.

Numerical and experimental investigations are performed for various distances L in the case of the DLS-specimens. All other dimensions are kept constant. Effects of the notch width, of the notch depth (undercut) or of the specimens' thickness are not

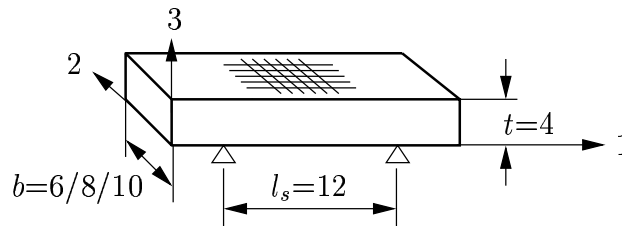


FIGURE 4.22: Geometry of the short-beam-shear specimen

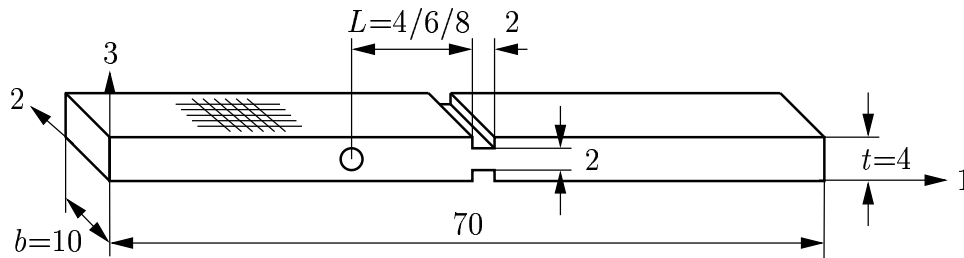


FIGURE 4.23: Geometry of the double-lap-shear specimen

investigated. Shokrieh and Lessard [1998] found that these effects do not play a major role. The SBS-specimen is analyzed for different widths b . The span length is chosen smaller (span/ $t=3$) than recommended in ASTM D-2344-00 (span/ $t=5$) because the critical global failure mode would be ply failure underneath the load introduction for the recommended span length.

The finite element analysis code MSC-Nastran (Macneal-Schwendler Cooperation) is used for all numerical investigations. Pre- and post-processing is done by the program MSC-Patran (Macneal-Schwendler Cooperation). The failure models are implemented by FORTRAN routines.

Three dimensional linear elastic finite element models are employed to obtain accurate stress results. The assumption of linear elastic material behavior is justified for the DLS-specimen if first delamination loads are applied. In contrast, the ILSS in the SBS-specimen is based on ultimate loads, although local failure occurs before complete failure. A comparison of linear and non-linear FE-analyses on SBS-specimens (see Xie and Adams [1996]) demonstrates that the difference in the ILS-stress is small (approximately 4%). Therefore, linear FE-analyses are sufficient for the investigation of SBS-specimens.

Examples of meshes for the SBS- and the DLS-specimen are shown in FIGURE 4.24

and FIGURE 4.25, respectively.

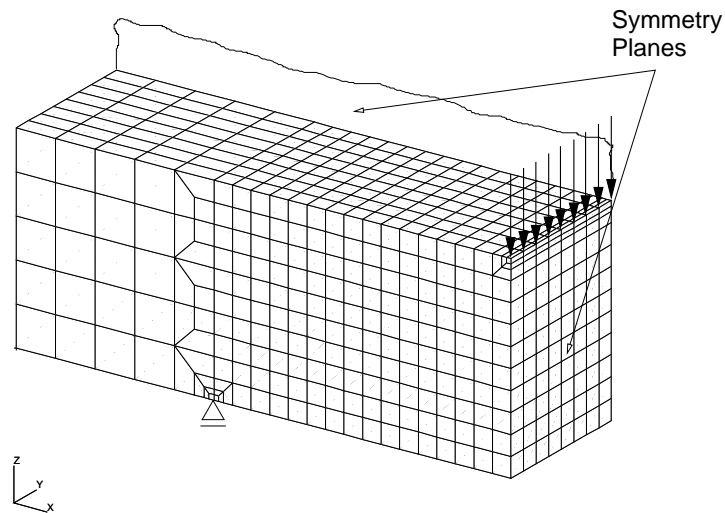


FIGURE 4.24: Example mesh of a short-beam-shear specimen

Due to the symmetries in geometry, loading and material it is sufficient to model only one quarter of the DLS- and the SBS-specimens. Here, linear, fully integrated HEX-elements are used. A comparison with other element types and integration schemes, as well as with finer mesh densities, show a very small influence on the obtained results.

4.5.3 Experimental Procedures

The laminate ISOVAL 10/E (NEMA/ASTM: G 10; ISOVOLTA AG, Austria) consists of 20 woven fabric glass fiber plies with a $[0]_{20}$ -lay-up in an epoxy (DGEBA) matrix. The material parameters are listed in TABLE 4.12, where l, q, t are the local and 1, 2, 3 are the global coordinate axes.

The subscripts “(-)” and “(+)” denote compressive and tensile loading. The values in brackets are the material parameters at test temperature of 77 K. All other values refer to 293 K (room temperature). The experiments were performed with an MTS 810 TestStar II Material Testing System under static loading conditions with a cross head speed of 0.5 mm/min (DLS tests) and of 1.3 mm/min (SBS-tests, ASTM D-2344-00), respectively.

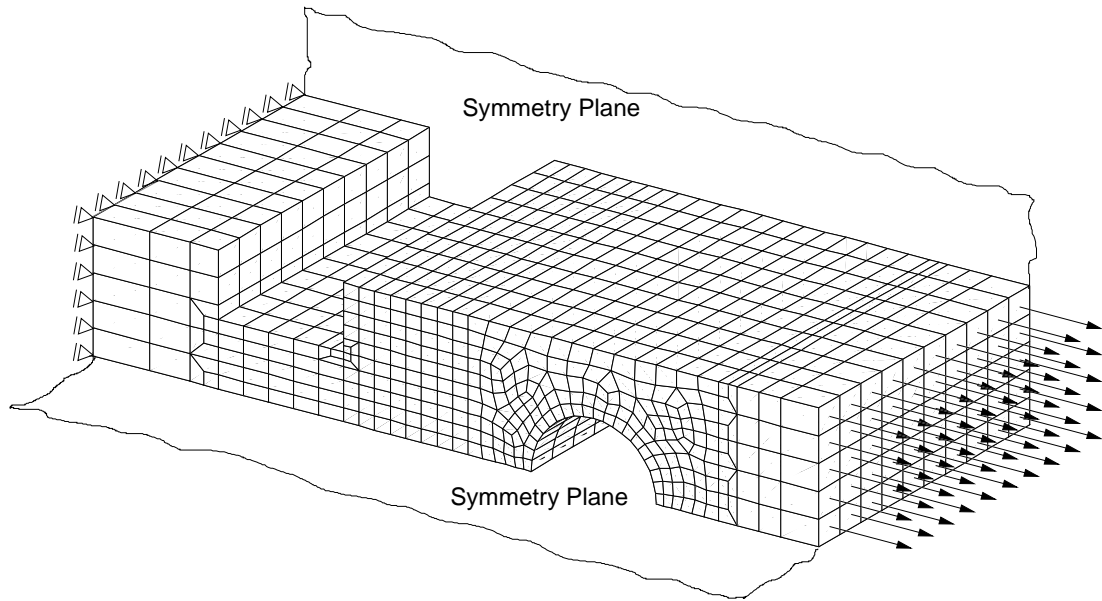


FIGURE 4.25: Example mesh of a double-lap-shear specimen

TABLE 4.12: Material parameters for a GFR woven fabric laminate at 293 K and 77 K (in brackets)

Variable	293 K (77 K)	Variable	293 K (77 K)
E_l	23000 (28000) MPa	$R_{ll}^{(+)} = R_{qq}^{(+)}$	330 (670) MPa
E_q	23000 (28000) MPa	$R_{ll}^{(-)} = R_{qq}^{(-)}$	370 (750) MPa
E_t	10000 (12000) MPa	R_{33}^{II}	70 (90) MPa
$G_{lq} = G_{tt}$	8000 (11000) MPa	$R_{tt}^{(-)}$	140 (400) MPa
$G_{qt} = G_{lq}$	8000 (11000) MPa	$R_{ql} = R_{tl}$	80 (150) MPa
ν_{lq}	0.12 (0.2)	$R_{qt} = R_{ql}$	80 (150) MPa
$\nu_{qt} = \nu_{lt}$	0.28 (0.42)		

The cross head speed of 0.5 mm/min was chosen from the tensile test standard ASTM D-3039M-00, because the investigated DLS specimen is not standardized. Each specimen geometry was investigated on four or five samples. For more details regarding the test procedure see Rosenkranz et al. [2001]. As mentioned above the span length (l_s) is chosen smaller ($l_s/t=3$) than recommended in ASTM D-2344-00 ($l_s/t=5$) because for the recommended span length the critical global failure mode would be ply failure under the load introduction. This fact can be proven by the formula for the bending stress of a

beam, which can be written in the investigated case as:

$$\frac{l_s}{t} < \frac{2 R_{ll}^{(+)} b t}{3 F_{ult}} \quad (4.4)$$

4.5.4 Analytical and Experimental Results

Short-Beam-Shear Specimen

FIGURE 4.26 shows the local delamination risk parameter computed for an SBS-specimen. FE-results on other SBS-geometries look similar. The first local failure, according to the

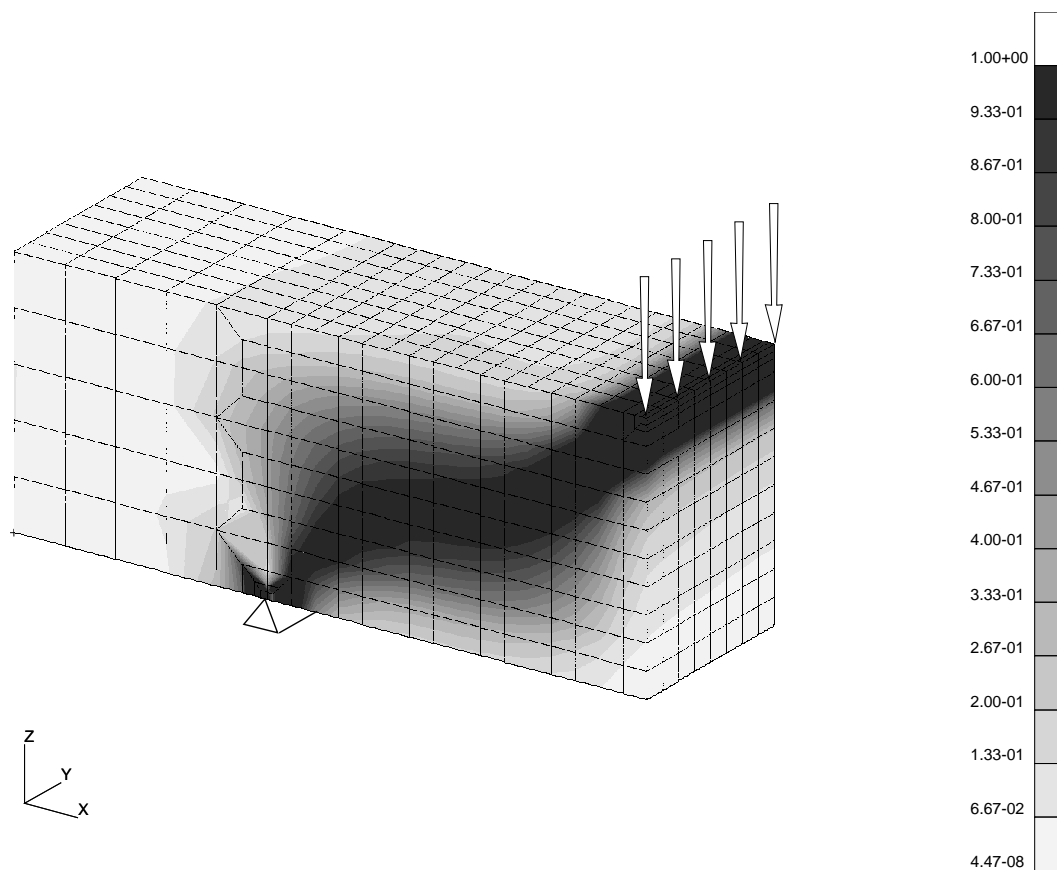


FIGURE 4.26: Delamination risk parameter of SBS-specimens ($b=6\text{mm}$) for 100% F_{ult}

FE-calculations, is observed in regions around the support and the load introduction at approximately fifty percent of the experimentally determined ultimate load. This local

failure does not affect the global failure behavior of the SBS-specimen. The complete delamination failure at the ultimate load level is mainly affected by the parabolically distributed shear stresses in the cross section between the support and the load introduction. In this critical region all other stress components are negligible.

The shear stress distributions are plotted in FIGURE 4.27 for the “inside” and “outside” region. These results are compared to those obtained from ASTM D-2344-00,

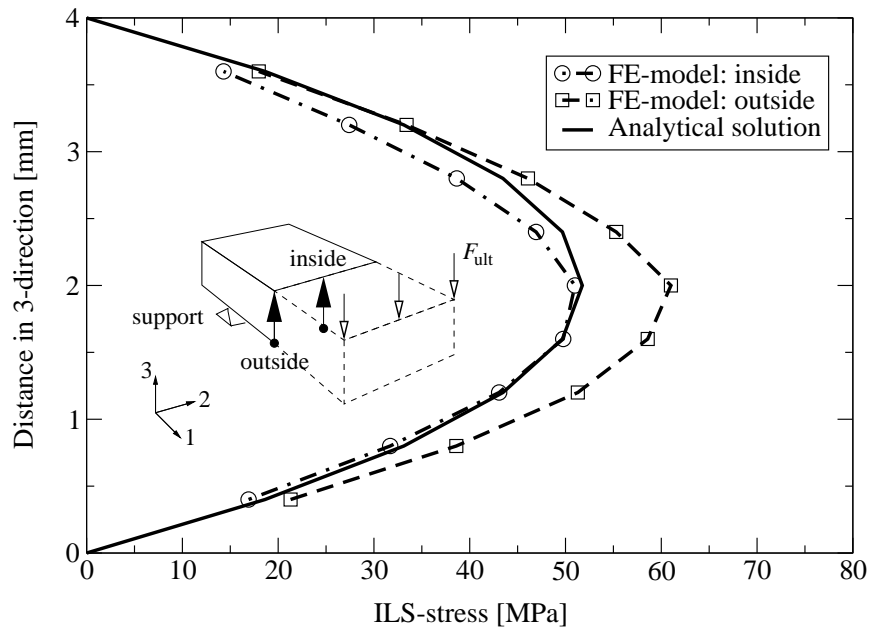


FIGURE 4.27: Parabolic ILS-stress distributions of an SBS specimen for F_{ult} , $b = 6$ mm

which is based on the assumption of a parabolic shear stress distribution that is constant over the width of the specimen (analytical 2D solution). It can be seen that the shear stresses which are predicted by the numerical analyses in the inside region are approximately equal to the analytical result. However, they are significantly higher at the outside region, although for the considered laminate no classical “free edge effect” appears. This stress concentration at the free edge cannot be reproduced by 2D analysis, where a plane stress state ($\sigma_{i2} = 0$) is assumed. Only 3D considerations of the beam problem show additional stresses ($\sigma_{i2} \neq 0$, see Reckling [1967]) and produce ILS-stress concentrations at the free edge, which should be distinguished from the “free edge effects” in laminates.

The ILS-stress concentration at the free edge depends on the width to thickness ratio

of the specimen (b/t) and may be characterized by an ILS-stress concentration factor (f) as follows

$$f = \frac{(\sigma_{31})_{3D}}{(\sigma_{31})_{2D}}, \quad (4.5)$$

where $(\sigma_{31})_{2D}$ and $(\sigma_{31})_{3D}$ stand for the shear stress obtained from 2D and 3D investigations, respectively. The distribution of the maximum ILS-stress concentration factors within the critical region (midway between support and load introduction) is shown in FIGURE 4.28. The ILS-stress concentration factors are drawn over the distance from the

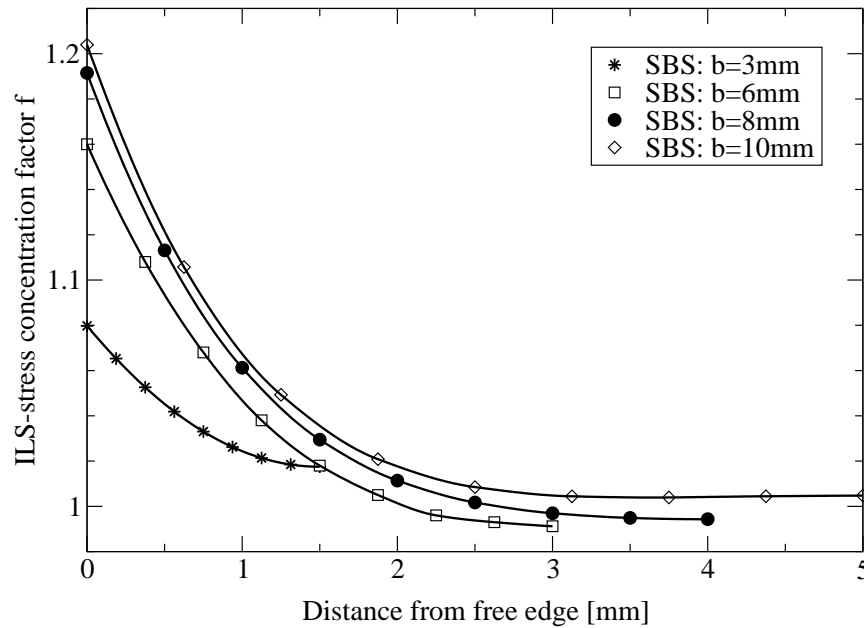


FIGURE 4.28: Maximum ILS-stress concentration factors f in the critical region of SBS specimen made of GFR woven fabrics

free edge for all specimen widths $b = 4, 6, 8$ mm, as well as for $b = 3$ mm. It can be seen that a stress concentration appears at the free edge and approaches 1.21, when b increases to 10 mm. The f -factor is approximately 1 inside the specimens, i.e., the stress is equal to the shear stress obtained from an analytical 2D solution. Only the specimen with $b=3$ mm shows a different behavior. In that case, the attenuation length (approximately 4 mm) of the ILS-stress concentration is much larger than $b/2$, which leads to a smaller difference in the ILS-stresses between the inside and outside region. This shows that a decreasing width of the specimen leads to a more uniform ILS-stress distribution within the critical region and, therefore, to higher experimental ILSS values.

The experimental ILSS results for different width to thickness ratios of the specimen are shown in FIGURE 4.29. A significant increase of the ILSS with decreasing tempera-

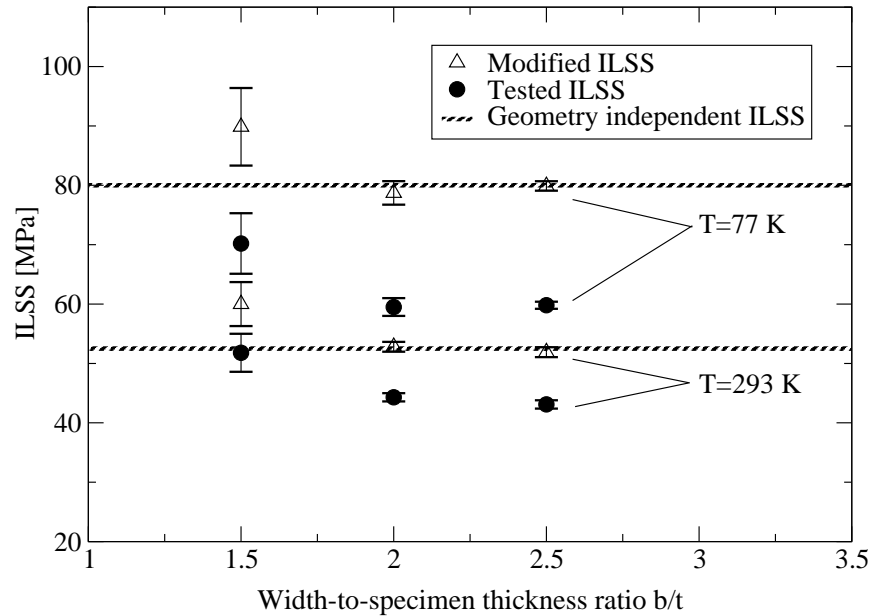


FIGURE 4.29: Measured, numerically modified and geometry independent SBS-ILSSs of a GFR woven fabric laminate at 77 K and 293 K

ture is noted. As found above the “local ILSSs” are higher than the experimental results. One way to modify the experimental ILSS results is to assume that the ILSSs are equal to the maximum shear stresses in the critical region. Then the modified ILSS is obtained by multiplying the data by the corresponding stress concentration factors. The modified ILSS-values are also shown in FIGURE 4.29. They should be geometry independent and are found to be 53 MPa for 293 K and 80 MPa for 77 K. Slight deviations occur only for $b/t = 1.5$, but this specimen type showed large error-bars and should be discarded.

Based on the above investigations two statements regarding the ILSS obtained from SBS-specimens can be made:

1. The experimental ILSS represents a lower bound for the local ILSS. The experimental ILSS is the smallest ILSS-value in the critical region, which is based on linear elastic material behavior and ultimate loads. In reality the non-linear material behavior leads, after the appearance of first delamination, to a stress transfer from the outside region (first delamination within the critical region) to the inside

region. Thus, this leads to higher shear stresses at the ultimate load level. For this reason the local ILSS-values are higher than the measured ILSS-values.

2. The maximum ILSS, which is obtained from the numerical analyses, represents an upper bound for the ILSS, if we assume that for $F = F_{\text{ult}}$ the modified ILSS is equal to the maximum shear stress appearing in the critical region. In the real structure a load $F < F_{\text{ult}}$ leads to the first local delamination and, therefore, the local ILSS-values are smaller than the computed ones.

The difference between the computed and the experimental ILSS-values is approximately 15 % (293 K) and 20 % (77 K), respectively. The local ILSS lies between 43 and 53 MPa at 293 K and between 60 and 80 MPa at 77 K.

Double-Lap-Shear Specimen

FIGURE 4.30 shows the computed delamination risk parameter of one of the investigated DLS-models for $F = F_{\text{ult}}$.

The critical region occurs near the notch (not around the hole), i.e., crack initiation starts at the notch for $F < F_{\text{ult}}$. The evaluation of the average delamination risk parameter within the overlapping zone leads to a value of approximately 50-60%. Hence, from this point of view the inter-laminar shear strength is significantly underestimated by the “standardized” analysis method (Equation (4.3)) which is based on mean shear stresses within the overlapping zone for $F = F_{\text{ult}}$. The main difficulty with the double-lap-shear test results from the fact that the standard procedure describes a complex fracture mechanical problem (crack initiation and crack growth) by a simple strength analysis.

The average stress analysis method (Brewer and Lagace [1988]) was applied to obtain the unknown ILSS-value. A priori, only the experimental first delamination (FDF) loads are known from acoustic emission testing. The averaging length a_0 and the “local ILSS” are unknown. An ILSS evaluation consisting of the following steps is applied:

1. Experimental determination of the FDF-loads.
2. Linear FE-analysis and computation of the stress state σ_{ij} within the critical notch region based on FDF-loads.

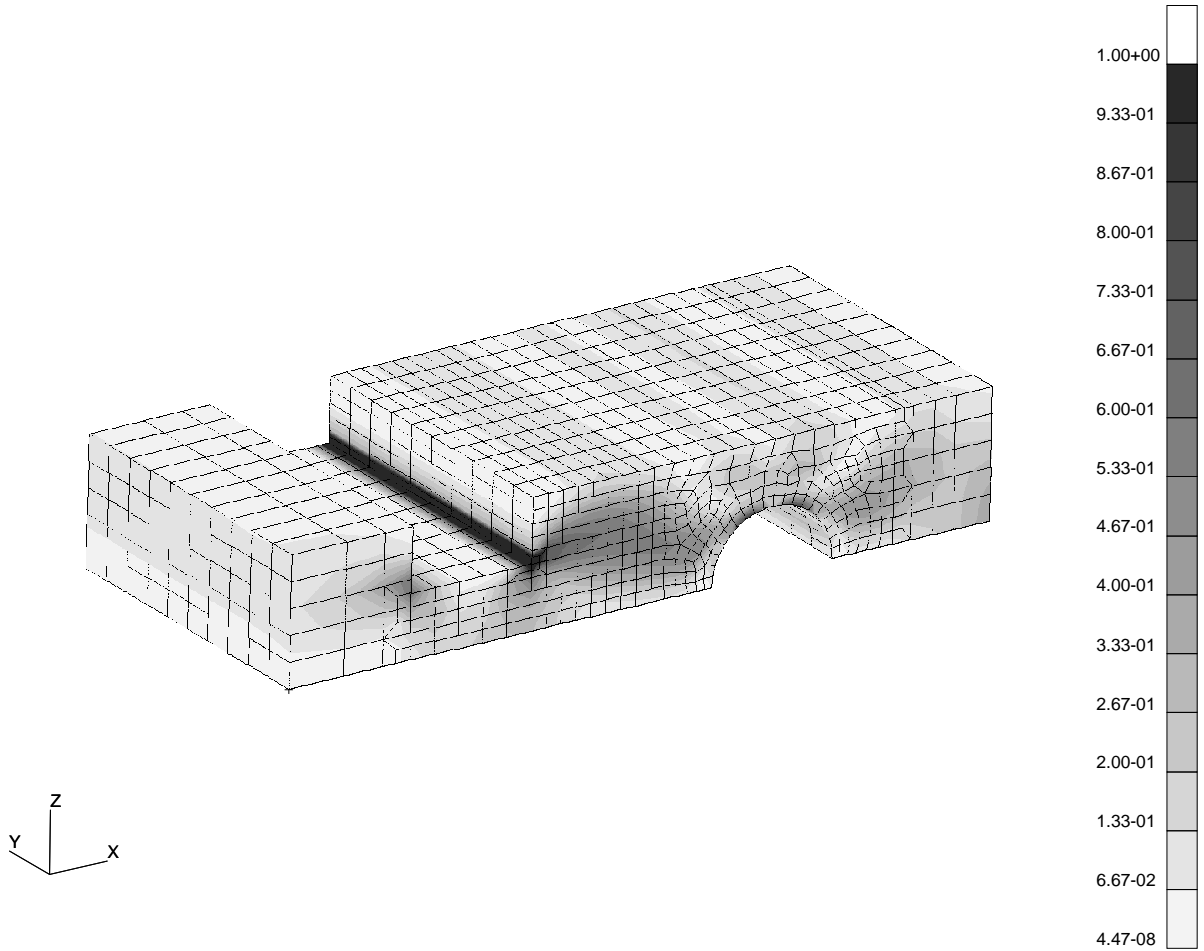


FIGURE 4.30: Delamination risk parameter of DLS-specimens ($L=4\text{mm}$), $F = F_{\text{FDF}}$

3. Evaluation of the local ILSS (R_{31}^{IL}) leading to the onset of delamination in dependence of the averaging length a_0 . To do so, Equation (2.12) can be rewritten as:

$$R_{31}^{\text{IL}}(a_0) = \mathcal{F}(\sigma_{31}^{\text{avg}}, \sigma_{33}^{\text{avg}}, R_{33}^{\text{IL}}), \quad (4.6)$$

where σ_{31}^{avg} and σ_{33}^{avg} are the averaged shear and tensile stresses over the averaging distance a_0 , respectively. R_{33}^{IL} is the inter-laminar tensile strength which must be known.

4. Determination of the “local ILSS” using $R_{31}^{\text{IL}}(a_0)$ -curves.

The local ILSSs are shown in FIGURE 4.31¹. The averaging length has a significant in-

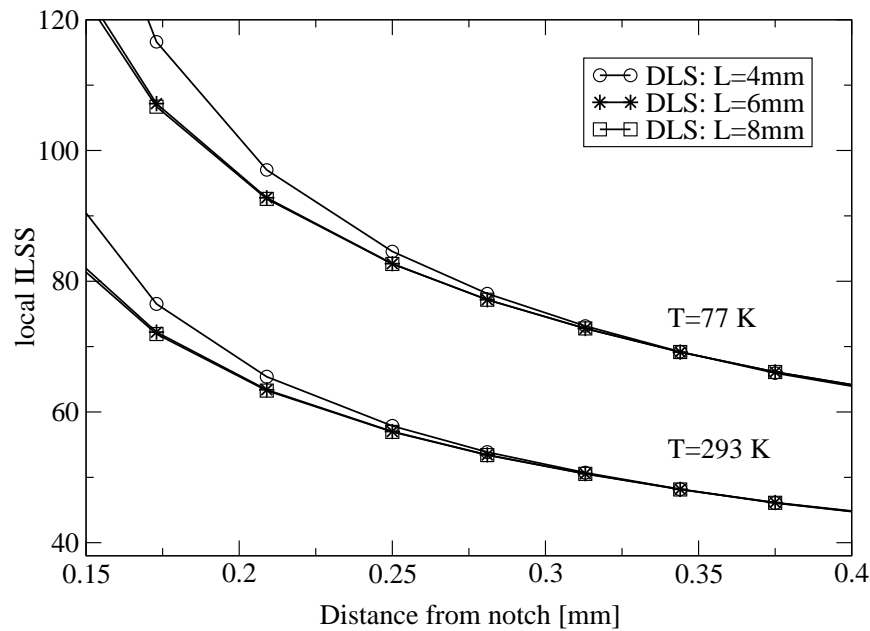


FIGURE 4.31: Local ILSS based on numerical DLS investigations and experimental FDF-loads of a GFR woven fabric laminate at 77 K and 293 K

fluence only for $a_0 < 0.34$ mm. For $a_0 > 0.34$ mm all curves coincide at both test temperatures. The difference between the DLS-specimen with $L = 4$ mm and the other DLS-specimens comes from the influence of the stress concentration due to the hole on the stress field in the notch region. This influence is not observed in the case of the two other specimens. The proper averaging distance for the present material system is found to be 0.34 mm. This corresponds to the point on the $R_{31}^{II}(a_0)$ -curves, where the ILSS of all three curves first meet. Based on the investigations in this section the local ILSS is obtained as 48 MPa at 293 K and 69 MPa at 77 K.

FIGURE 4.32 shows a comparison of the ILSS based on SBS investigations and the local ILSS obtained from DLS tests as discussed above. As mentioned above, the SBS results provide bounds for the local ILSS.

In TABLE 4.13 and FIGURE 4.33 the “local ILSSs” are compared to the experimental SBS and DLS ILSS-results, where the values in the table and in the figure correspond. The 6 mm SBS-specimen is not included in TABLE 4.13, because this specimen type did

¹For these results the mesh shown in FIGURE 4.25 is refined. The critical region is meshed using 30 elements/mm.

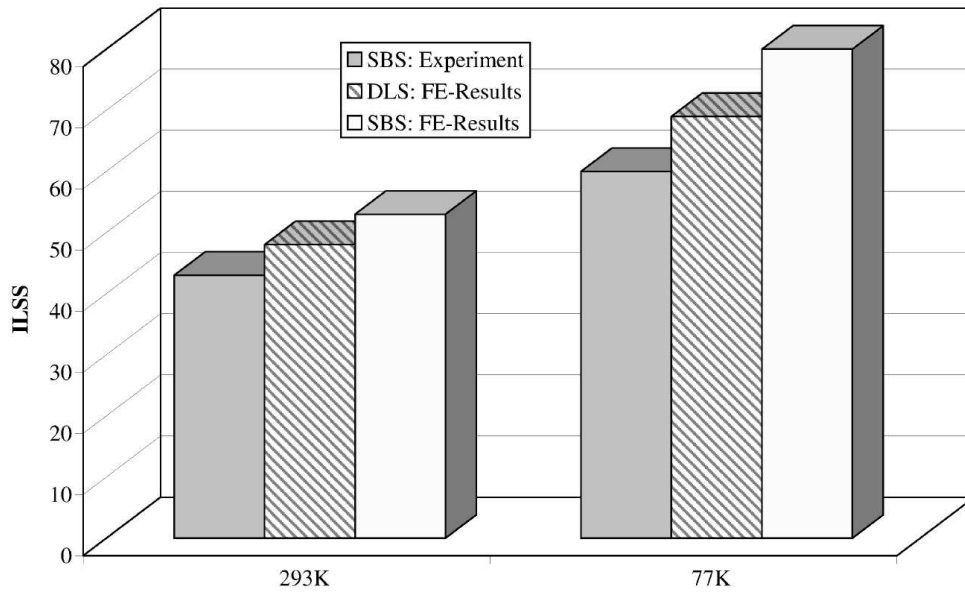


FIGURE 4.32: Comparison of the different ILSS values for 77 K and 293 K

TABLE 4.13: Comparison of the local ILSS R_{31}^{IL} and the experimental SBS- and DLS-ILSS for 293 K and 77 K (in brackets)

SBS				DLS			
Width b	R_{31}^{IL}	$(R_{31}^{IL})_{exp}^{SBS}$	Difference	Length L	R_{31}^{IL}	$(R_{31}^{IL})_{exp}^{DLS}$	Difference
10 mm	48(69)	43(60)	-10(-13)%	8 mm	48(69)	28(36)	-41(-48)%
8 mm	48(69)	44(60)	-8(-13)%	6 mm	48(69)	33(44)	-31(-36)%
				4 mm	48(69)	33(47)	-31(-32)%

not lead to reliable ILSSs. It can be seen that both tests underestimate the local ILSS, but that especially the DLS-specimens shows a significant underestimation by up to 48%, if the standard evaluation procedure is employed.

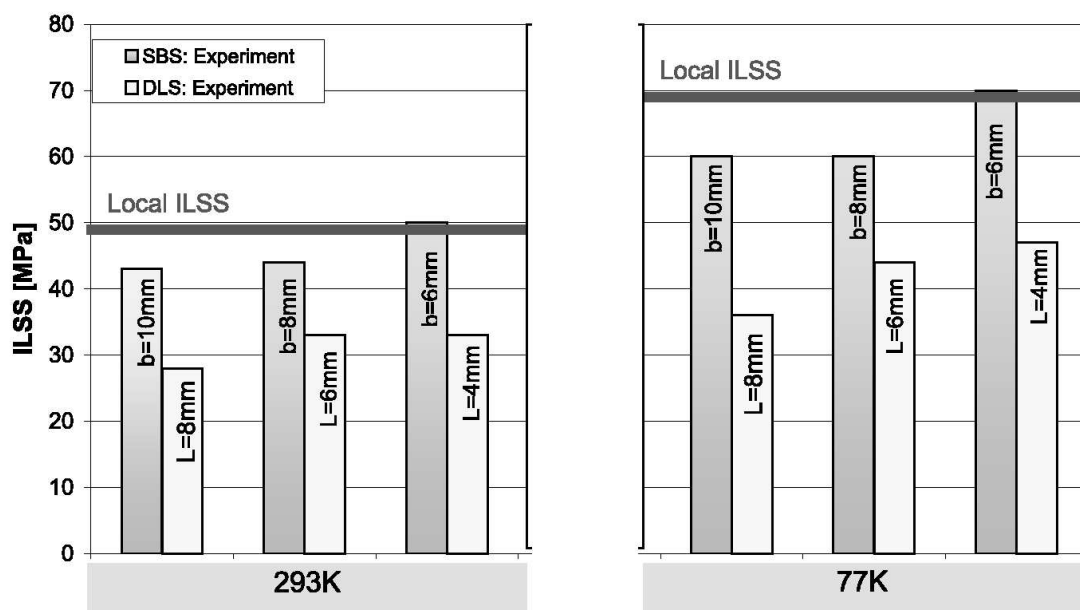


FIGURE 4.33: Comparison of the local ILSS with measured ILSS obtained from SBS and DLS experiments for GFR woven fabric laminate at 293 K and 77 K

Chapter 5

Investigations of Perforated Laminates

The first section of this chapter gives an overview of the developed two-scale analysis strategy. Next general model parameters are presented. After that three different material systems are investigated, two woven fabric laminates and one uni-directional laminate.

5.1 Two-scale Analysis Strategy

A local-global-local FE-based strategy (two-scale analysis strategy) is developed for the analysis of the stiffness and failure behavior of a global structure which is partially composed of perforated laminates (acoustic skins). FIGURE 5.1 shows the operational sequence of the developed local-global-local finite element approach.

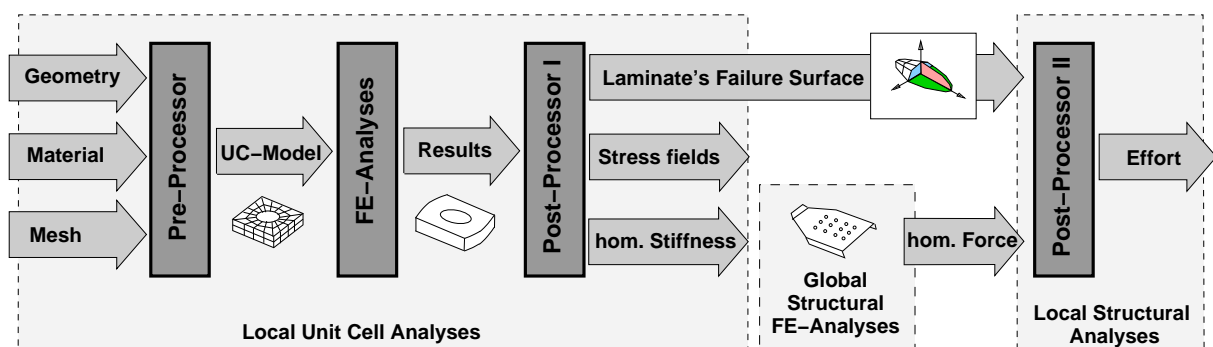


FIGURE 5.1: Two-scale analysis strategy

The simulation-strategy can be split into three parts:

1. **Local Unit cell analysis:** Input values are the geometry of the unit cell, material parameters (the lay-up of the layered laminate, stiffness and strength of the individual layers) as well as required mesh parameters (number of elements around the hole, etc.). With these input values a *Pre-Processor* generates input files for both a 2/D- and a 3/D-FE-UC-model for use with a standard finite element program. The *FE-analyses* are started interactively by the *Pre-Processor*. After obtaining solutions, the finite element results (displacements and stresses) are read by *Post-Processor I* and the homogenized stiffness matrices are calculated ($\underline{\underline{A}}^h$, $\underline{\underline{B}}^h$, $\underline{\underline{D}}^h$ for the 2/D case and $\underline{\underline{A}}^h$ for the 3/D case). The 3/D stress fields for every load case are taken to compute a failure surface for the considered UC which is the failure surface of the homogenized perforated laminate, i.e., acoustic skin. The stiffness and failure results are finally stored in newly created results files.
2. **Global structural analysis:** The global FE-analysis of the sandwich shell structure can be performed, where the perforated regions of the face sheet representing the acoustic laminate are simply considered as a homogeneous (anisotropic) face layer with the homogenized stiffness values obtained from step 1. The results of such global structural analyses are the homogenized membrane forces (stresses) in the face sheet of the sandwich shell of the investigated structure (including the perforated regions).
3. **Local structural analysis:** In this final step of the simulation strategy a second *Post-Processor (Post-Processor II)* uses the homogenized membrane forces in the relevant face sheet obtained from the global structural analysis, as well as the failure surface, defined via the unit cell analysis (both stored in results files) and calculates a safety factor $^{\text{lam}}\lambda$ for every finite element of the perforated regions of the global structure. These results are stored in a neutral-file-format and may then be pictured by the standard graphical *Post-Processor MSC-Patran*.

5.2 Model Parameters

5.2.1 Unit Cell Geometry

FIGURE 5.2 shows a plane sketch of the geometry of a unit cell. The unit cell is a par-

allelepipiped with a thickness t^{lam} . Further unit cell dimensions are the lengths l_1 and l_2 , the hole diameter D and the distance d_2 , where $d_2 = 0$ for a rectangular arrangement. Finite Element Models All investigations in this chapter are based on the same finite el-

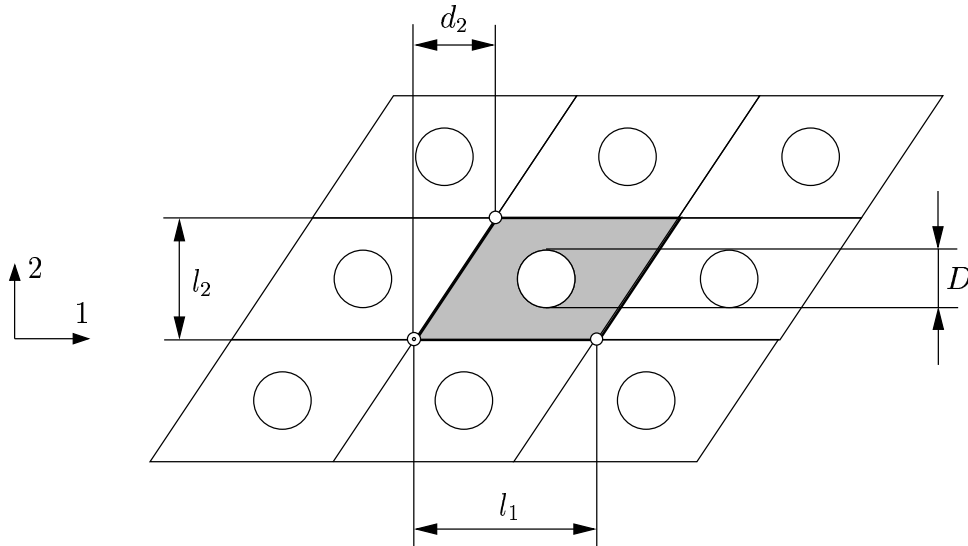


FIGURE 5.2: Dimensions of a typical unit cell

ement models. 2D and 3D finite element unit cell models are investigated. Algorithms are developed for implementing the above homogenization methods discussed in Section 3.2 together with tools for computing the failure surfaces. These algorithms access a standard displacement based FE-solver for the unit cell analyses. Linear quadrilateral (laminated shell) and hexagonal (anisotropic solid) elements are used for the 2D and 3D FE-models, respectively. Typical unit cell model sizes are about 2000 elements for the 2D models and 2300 elements per ply for the 3D models. Each ply is modeled with a minimum of four Hex Elements in thickness direction. Within the averaging length a minimum of five elements is used. Mesh density studies are performed and the error in the stiffness and strength values of the used meshes is found to be less than 2%. To ensure the reliability of the finite element method for calculating free edge stresses in composite materials the guidelines of Whitcomb et al. [1982] are used which were proven to be acceptable in Stiftinger and Rammerstorfer [1996]. A typical FE-mesh of a unit cell is shown in FIGURE 5.3.

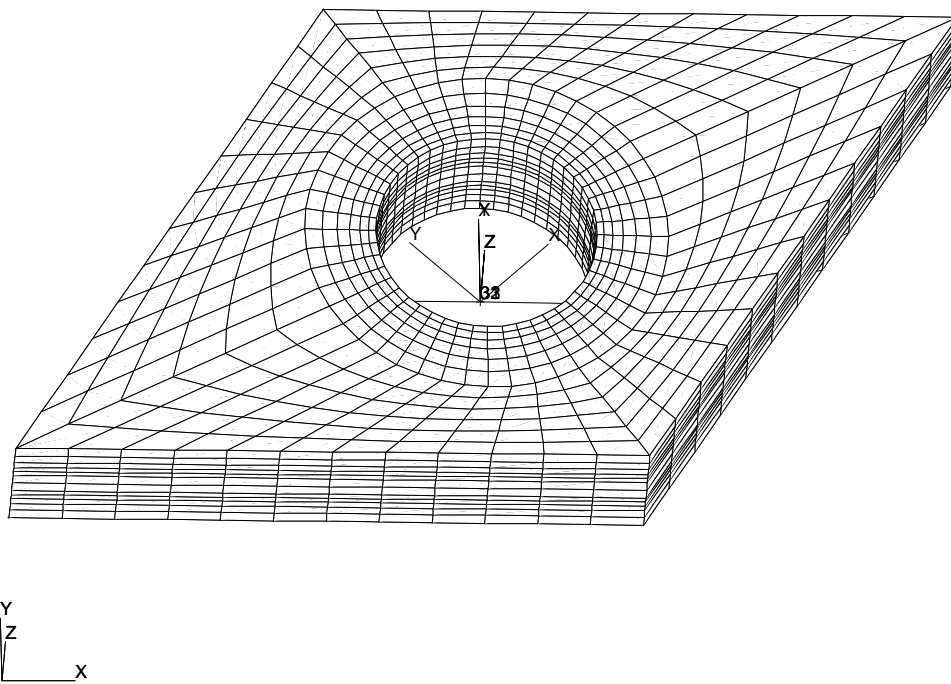


FIGURE 5.3: Finite element mesh of a unit cell

5.3 Unit Cell Investigations of Uni-directional Laminates

In the following local analyses (i.e., unit cell analysis) are carried out. They are demonstrated by examples with different lay-ups, hole arrangements and hole diameters.

5.3.1 Geometry of the Unit cell

FIGURE 5.2 shows the geometry of the investigated unit cell. For the reference unit cell the dimensions are: $D=1.5$ mm, $l_1=4.6$ mm, $l_2=3.98$, $d_2=2.3$ for a hexagonal arrangement of holes and $D=1.5$ mm, $l_1=l_2=4.28$ mm, $d_2=0$ for a square arrangement. The perforation area, the area of the hole cross section, is about 10% of the total unit cell area. For investigations of configurations with other hole diameters ($D=0.8, 1.2, 2.3, 3, 4.5, 6$ mm) the fraction of the perforation area is kept constant at 10%, and the lengths ($l_1=l_2$) of the investigated square arrangement are varied accordingly.

5.3.2 Ply Material

The used uni-directionally reinforced graphite/epoxy layers have a ply thickness of 0.2 mm. The major mechanical properties are $E_l=125$ GPa, $E_q=8$ GPa, $E_t=8$ GPa, $G_{lq}=G_{lt}=5$ GPa, $G_{qt}=4$ GPa, $\nu_{lq}=\nu_{lt}=0.3$, $\nu_{qt}=0.49$, $R_{l+}=1600$ MPa, $R_{l-}=1000$ MPa, $R_{q+}=40$ MPa, $R_{q-}=220$ MPa, $R_{t+}=40$ MPa, $R_{t-}=220$ MPa, $R_{ql}=R_{lt}=80$ MPa, $R_{qt}=65$ MPa. At the interface the intra-laminar strength values (R_{t+} , R_{qt} , R_{lt}) are based on the corresponding ply values by reducing them with a weakening factor of $f_{wI}=0.8$ (see Puck [1996]). All strength values are first failure strengths. The interaction parameter for the Tsai-Wu criterion is chosen to be 0.0 (see Jones [1999]). Parameters for the Puck criterion are on the one hand the gradients of the failure curves which are $p_{qt+}=0.27$, $p_{qt-}=0.27$, $p_{ql+}=0.35$, $p_{ql-}=0.30$ (taken from Puck et al. [2002]) and on the other hand the empirical parameters for the influence of the longitudinal stress σ_{ll} on the inter-fiber failure, which are chosen as $n=7$ and $|\sigma_{1d}| = 1.1R_{l\pm}$ (for a detailed description see Puck [1996]). The investigated laminates are composed of three layers with a $[0/\alpha/0]$ lay-up.

5.3.3 Results

Some of the results are presented for a selected reference case. This case is chosen such, that it represents also other test cases which are not shown here.

Due to the well known problems with using the maximum stress and Tsai-Wu criterion (see Section 2.2.2) the Puck criterion is used in this section to obtain failure results.

Investigations of different characteristic distances a_0 for a [0/45/0] laminate

The first investigation in this chapter deals with the dependence of the characteristic distance a_0 on the hole diameter. Laminates with perforations with hole diameters from 0.8 to 6 mm are investigated. The presented results are based on a fixed value of a_0 taken as one ply thickness. In a further investigation the characteristic distance was chosen in an alternative way. First a_0 is kept constant at 0.2 mm ($=t_s$) for all hole diameters (denoted with “fixed” in FIGURE 5.4). Then a_0 is varied proportionally with the hole diameter where the reference hole diameter is 1.5 mm with $a_0=0.2$ mm (denoted with “prop.” in FIGURE 5.4). The dimensions of the unit cells are chosen such that the fraction of the perforated area is kept constant (approximately 10%). The ply thickness and lay-up are the same in all investigations. The effective stiffness is practically not influenced by the absolute value of the hole diameter and by any averaging length and is, therefore, not displayed here.

In the following “relative stiffness” or “relative strength” means the ratio between numerical 3D finite element unit cell results (denoted with superscript “h”) of the corresponding perforated laminate and analytical classical lamination theory results of a non-perforated laminate, respectively. The relative strength values are shown in FIGURE 5.4 where the “+” subscripts denote positive tensile and shear strength values. The relative compressive strength values look qualitatively the same and are not plotted. The trend of the relative strength is nearly the same in all three pictures of FIGURE 5.4 if the fixed and proportional cases are considered separately. Only the level of strength reduction changes.

Experiments published in Xiao and Bathias [1993] show that for hole diameters approaching zero the perforation effect disappears which is in contrast to the behavior of homogeneous materials. Although even small holes theoretically exhibit a geometrical stress concentration and a free edge effect, these very local stress concentrations

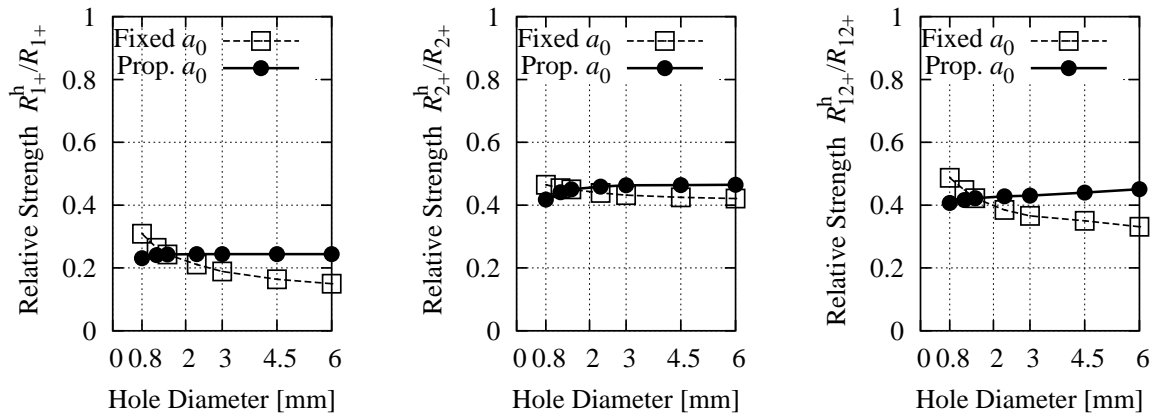


FIGURE 5.4: Relative strength for different a_0 of a [0/45/0] UD laminate. a_0 is 0.2 mm for the fixed investigations and a_0 is 0.2 mm for a hole diameter of $D = 1.5$ mm for the proportional investigations, where the perforated area is 10%.

¹ obviously become irrelevant which is an experimental justification for the averaging procedure. The disappearance of the perforation effect is more or less captured by using a fixed averaging distance, whereas the calculated effective strength would remain approximately unchanged if a_0 was scaled proportionally with the hole diameter. Hence, an a_0 value which does not depend on the hole diameter should be used, if the characteristic distance is unknown in advance.

An explanation for this scaling effect can be obtained from FIGURE 5.5. There, numerically obtained σ_{II} stress distributions (critical stress component) are plotted over the distance from the hole at the 0° interface of a [0/45/0] UD laminate for proportional scaled unit cells with hole diameters $D=0.8, 1.5, 3.0, 6.0$ mm. The ply thickness is kept constant. The stress curves show, due to the stress concentration, a constant maximum value at the hole and are affine to each other, scaled proportionally with the hole diameter. An averaging distance a_0 which is proportional to the hole diameter always leads to constant average stresses where the averaged stresses based on a constant value of a_0 decrease with decreasing hole diameter. Therefore, higher strength values are obtained. This means a_0 is an intrinsic length dependency on the material but not on the geometry of the perforation.

¹For very small hole diameters the assumption for homogenization, i.e., using effective ply properties on the meso level, are more and more violated and a more sophisticated micro mechanical approach on the fiber-matrix scale would be required.

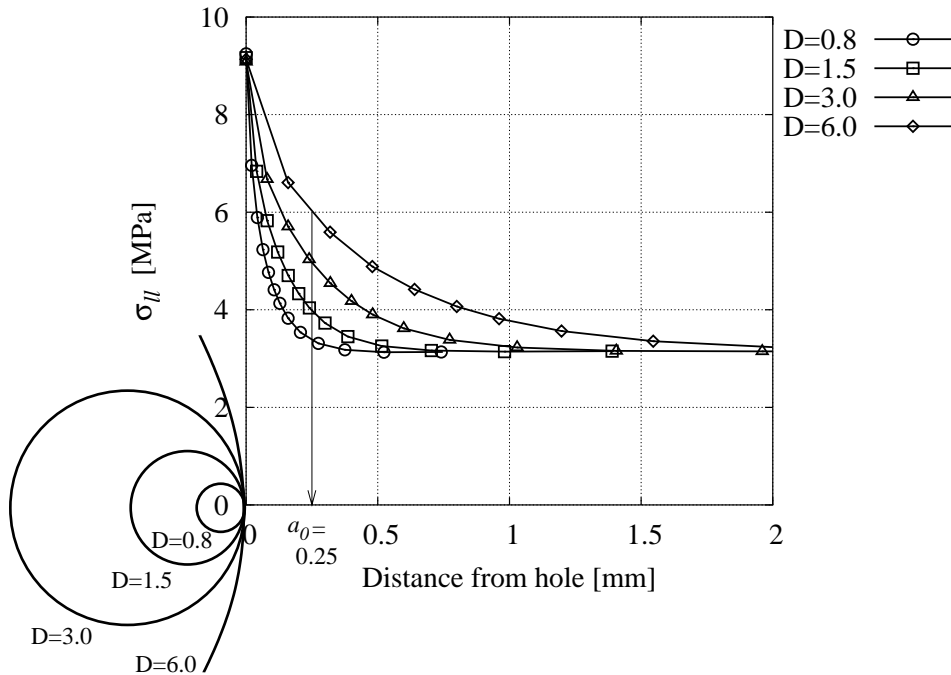


FIGURE 5.5: Numerical σ_{ll} stress distributions at the 0° interface of a $[0/45/0]$ UD laminate for hole diameters $D=0.8, 1.5, 3.0, 6.0$ mm over the distance from hole

Unit cell deformations and stresses

FIGURE 5.6 shows the deformation and σ_{ll} stress distribution of a $[0/45/0]$ laminate for a square hole pattern. The laminate is loaded in global 1-direction with $N_{11} = 1$ N/mm ($\Sigma_{11} = 1.66$ MPa). High stress concentrations appear in the 0° -plies. If the stress concentration factor is related to the stresses in the non-perforated case, σ_{ll} of the non-perforated laminate in the 0° -ply must be determined. This stress, which is defined as the nominal stress in this case, is 2.35 MPa for the considered 0° -ply. The maximum σ_{ll} for the perforated case is 10.9 MPa, leading to a stress concentration factor of $k = 4.6$. Compared to isotropic materials, where $k = 2.9$ for this unit cell geometry, the k -factor of the laminate is 60% higher.

If the above maximum σ_{ll} stress of a perforated 0° -ply in a $[0/45/0]$ compound, which is based on 3D FE-models, is compared to the same σ_{ll} stress obtained from 2D FE-models then the maximum σ_{ll} stress in the same region is 8.08 MPa. The difference of both stresses is approximately 26% which goes back to the free edge effect. That means that the high stress concentrations of perforated laminates compared to isotropic

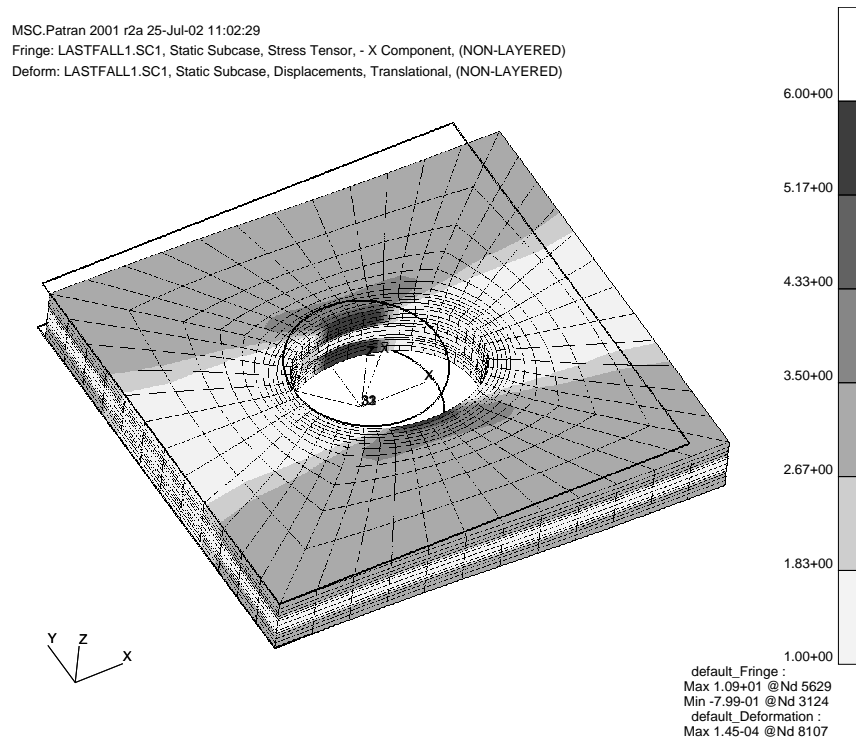


FIGURE 5.6: σ_{11} ply stresses in a [0/45/0] UD laminate, tensile loading in 1-direction

perforated materials are influenced by:

1. Ply stresses: Some ply stresses are usually higher than the applied nominal stresses, where the in-plane nominal stress is defined as the ratio of the membrane force to the laminate thickness in the case of laminates.
2. Free edge effect: On free edges a free edge effect appears, which may lead to a further stress increase.

A comparison of the far field stress (nominal stress for the isotropic material), the highest stress around a hole of an isotropic material, the ply stresses of the considered laminate (nominal stress for the laminated composite), and the highest stresses around the hole of a perforated laminated composite obtained from 2D and 3D FE-models are summarized in FIGURE 5.7. The difference between the “NP: Ply” and “P: Ply 2D” case represents the stress concentration due to the hole. The additional stress increase between the “P: Ply 2D” and “P: Ply 3D” case comes from the free edge effect.

FIGURE 5.6 shows also the periodic unit cell deformation which is not symmetric

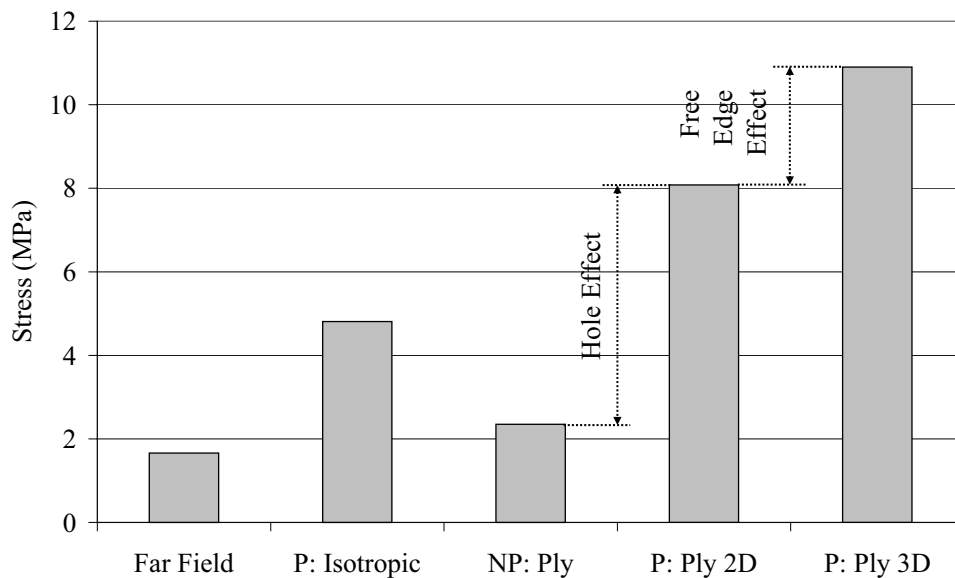


FIGURE 5.7: σ_{11} stresses: Far field stress, highest stress around a hole of a perforated (P) isotropic plate (hole diameter 1.55 mm), 0° -ply stress of a non-perforated (NP) $[0/45/0]$ UD laminate, highest stresses around a hole of a 0° -ply of a perforated (P) $[0/45/0]$ UD laminate obtained from 2D and 3D FE-models

with respect to the 1 and 2 axes because of the unbalanced nature of the $[0/45/0]$ laminate. Furthermore, the periodic stress field can be seen. That means that the stress tensor has to be the same on corresponding edges.

2D - 3D failure surfaces of a perforated $[0/45/0]$ UD laminate

FIGURE 5.8 shows the differences between the strength predictions obtained by using a 2D and a 3D finite element model for a perforated $[0/45/0]$ UD laminate. In 2D models laminated Mindlin-Reissner shell elements are used, in 3D models anisotropic continuum elements are used. In FIGURE 5.8 the 2D failure envelope is the outer curve. It is evident that the problems with the 2D model are two fold. On one hand the absolute strength values are overestimated by the 2D model (in some case up to 30-40%) and on the other hand the fracture angle and/or fracture modes are different from those predicted by 3D models. Regarding the stiffness the difference between 2D and 3D models is small and approximately less than 5%. For more detailed informations see Pahr et al. [2001]. An outcome of this part of the study (also valid for other $[0/\alpha/0]$ -lay-ups) is

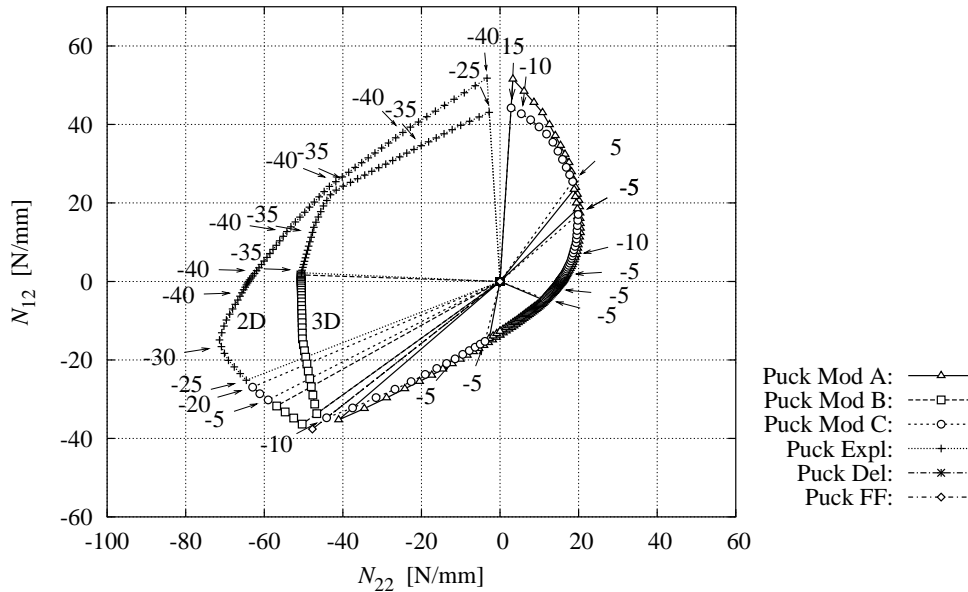


FIGURE 5.8: Difference of a 2D and 3D finite element unit cell model - perforated $[0/45/0]$ UD laminate (numbers along the Puck curves show the inter-fiber fracture plane angle θ)

that a 2D finite element model is insufficient for failure investigations. The reason for the overestimation of strength values by the 2D results lies in the fact that the 2D models cannot capture the free edge effect.

Risk of Delamination of a perforated $[0/90/0]$ UD laminate

In order to show the risk of delamination a $[0/90/0]$ lay-up is considered. The interface weakening factor f_{wI} is chosen as 0.2 and 0.8. This means the inter-laminar strength values at the interface are reduced to 20 or 80% of the intra-laminar values. FIGURE 5.9 shows a comparison for a cut along the $N_{11} - N_{22}$ plane (other failure surfaces looks similar). Especially in the case of compression loading in 2-direction the two curves are different and for $f_{wI} = 0.2$ delamination occurs. The rest of both failure surfaces looks similar. But it should be mentioned that a weakening factor lower than $f_{wI} = 0.8$ points out an improper manufacturing process. That means that delamination failure is not critical for the investigated lay-up if the laminate is carefully manufactured. Further studies have shown that delamination is not critical for any $[0/\alpha/0]$ lay-up.

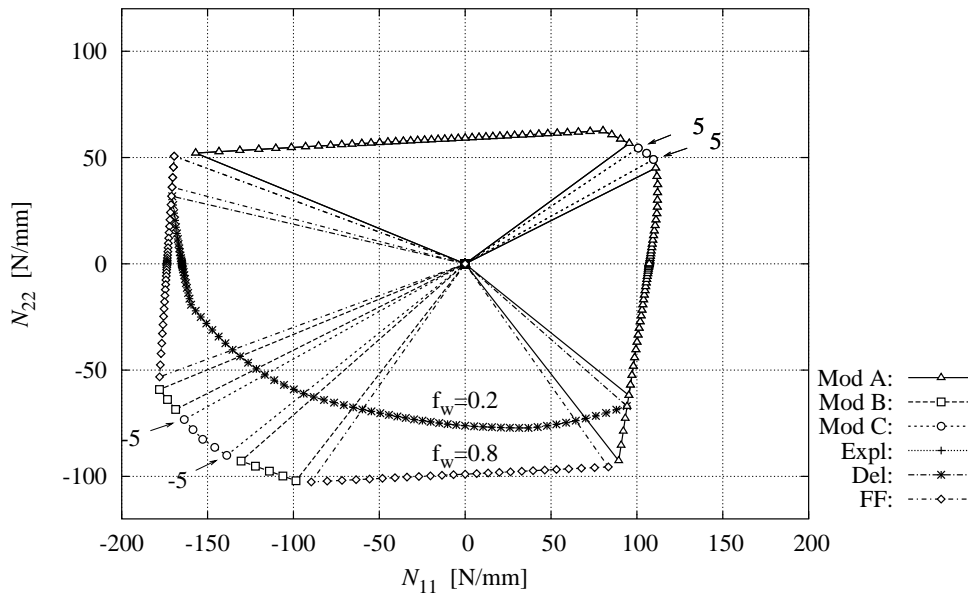


FIGURE 5.9: Delamination failure curves for $f_{wI} = 0.2$ and $f_{wI} = 0.8$ - perforated $[0/90/0]$ UD laminate (numbers along the Puck curves show the inter-fiber fracture plane angle θ)

Comparison of hexagonal and rectangular hole pattern

The influence of the arrangement of the holes (hexagonal or rectangular) is investigated for different α -angles and for a hole diameter of 1.5 mm. The angle of the mid-layer (α) is varied between 0° and 90° in 22.5° steps. As mentioned above, in the following relative stiffness or strength means the difference between results from CLT for a non-perforated laminate and numerical 3D finite element unit cell results (denoted with superscript "h") of the corresponding perforated laminate, respectively. The dimensions of both unit cells are chosen such that the perforated area (approximately 10%) is kept constant.

FIGURE 5.10 shows the relative stiffnesses, where A_{33}^h / A_{33} corresponds to the relative shear stiffness. In general the obtained stiffness for the perforated plate is 60-80 % of the stiffness of the non-perforated laminate. The relative longitudinal stiffness (A_{11}^h / A_{11}) does not show any significant influence on the angle α (mid-layer angle). It is interesting that the biggest stiffness reduction appears when the mid-plane layer becomes a load bearing part which can be seen in figure 5.10 for A_{22}^h / A_{22} (biggest stiffness reduction at $\alpha = 90^\circ$) and for the A_{33}^h / A_{33} ($\alpha = 45^\circ$). This effect is less pronounced

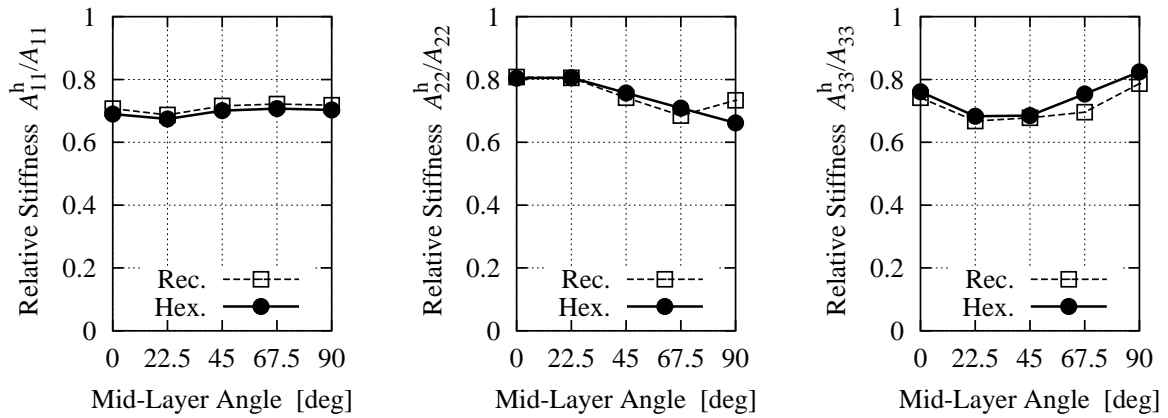


FIGURE 5.10: Relative stiffness of hexagonal and rectangular arrangements of holes (superscript “h” denoted the perforated case) for CFR UD laminates

for the A_{11}^h / A_{11} case because here the load is always transferred by two 0° -layers. For practical purposes the difference in the relevant stiffness terms between hexagonal and rectangular arrangement is negligible.

In FIGURE 5.11 the strength reductions for the two hole patterns are plotted versus the mid-layer angle α . The “+” and “-” subscripts denote “positive” and “negative” strengths, i.e., for the longitudinal directions these are tensile and compressive strengths, and in the case of shear strengths they refer to the sign of the shear stress. In general it can be seen, that the relative strength is much more affected by the perforations than the stiffness and decreases to 20-50% of the initial values. A marked increase of the R_{1+}^h / R_{1+} values is evident for an increasing α (note that the absolute strengths decrease!). The R_{2+}^h / R_{2+} and R_{2-}^h / R_{2-} values show a tendency to decrease. In the case of the shear strengths a strong increase between $\alpha = 22.5$ and $\alpha = 67.5^\circ$ can be seen. As in the case of the stiffness the differences between the hexagonal and rectangular arrangement are very small. A slight difference between both is evident only for the $[0/90/0]$ lay-up. Especially for this lay-up it can be seen that the relative longitudinal strength is larger for the rectangular arrangement and the relative shear strength is more pronounced for the hexagonal pattern. This material behavior comes from the fact that the load bearing fibers are more or less weakened in the individual arrangements, i.e., the rectangular pattern for a $[0/90/0]$ lay-up is more appropriate if higher longitudinal strength values are needed, and the hexagonal pattern leads to higher shear strength

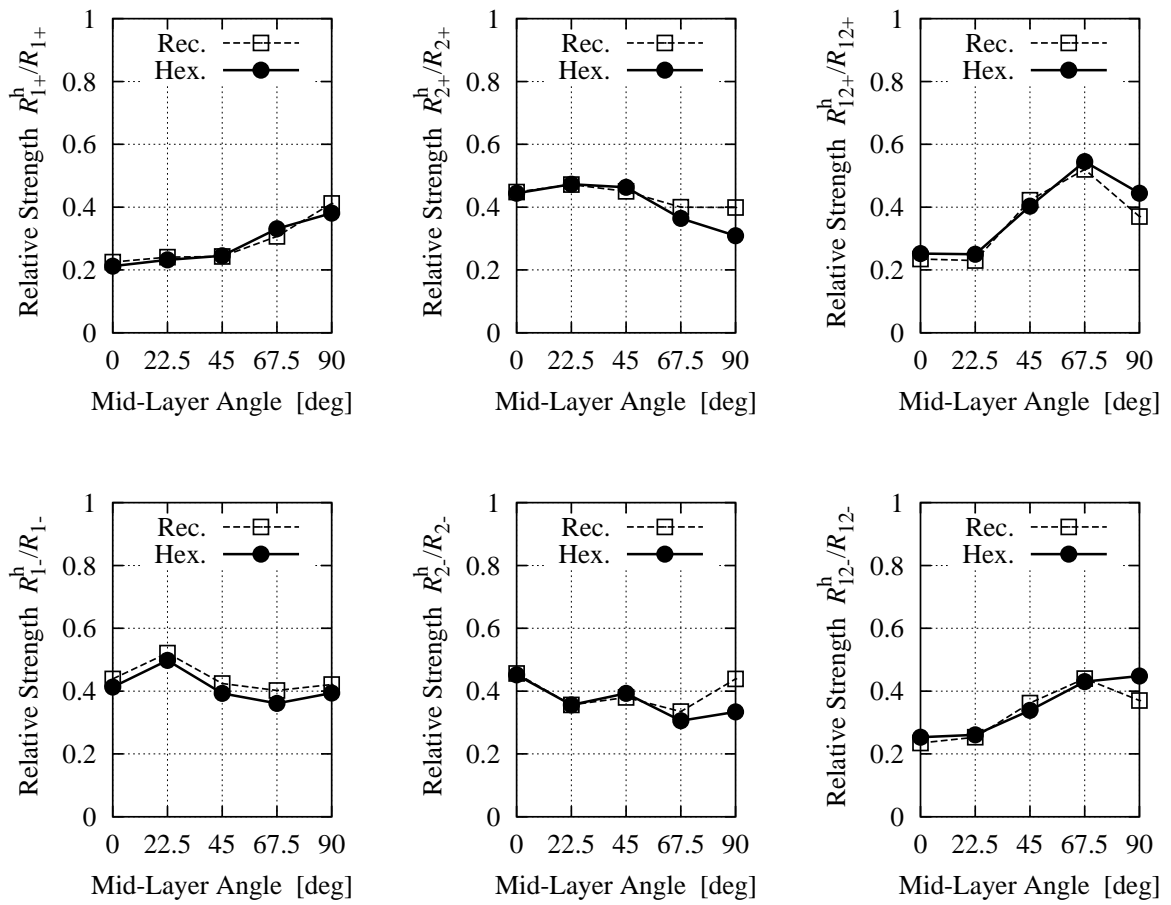


FIGURE 5.11: Relative strengths for hexagonal and rectangular arrangement of holes for CFR UD laminates

values.

5.4 Investigations of Perforated Woven Fabric Laminates - Material System I

The following analyses pertain to two laminates - a $[0]_6$ and a $[0/45/0]$ lay-up. In the first part of this section different investigations on unit cells are performed, such as on the influences of hole arrangement and hole diameter, as well as studies of the critical failure modes. In the second part global structural analyses are presented on tensile test specimens.

5.4.1 Geometry of a Unit Cell

FIGURE 5.2 shows the geometry of a unit cell, the dimension being $D=1.55$ mm, $l_1=4.6$ mm, $l_2=3.98$ and $d_2=2.3$ for the hexagonal arrangement and $D=1.55$ mm, $l_1=l_2=4.28$ mm and $d_2=0$ for the square arrangement. The perforated area is about 10% of the total unit cell area. For investigations with other hole diameters ($D=0.8$ and $D=3$ mm) the perforated area is kept constant and the pitch ($l_1=l_2$) of the investigated square arrangement is varied.

5.4.2 Ply Material

The used woven graphite/epoxy fabrics have a ply thickness of 0.35 mm. The major mechanical properties are taken from previous investigations, and are given as $E_l=69$ GPa, $E_q=69$ GPa, $E_t=12$ GPa, $G_{lq}=G_{qt}=G_{lt}=2.41$ GPa, $\nu_{lq}=0.03$, $\nu_{qt}=\nu_{lt}=0.17$, $R_{l+}=545$ MPa, $R_{l-}=260$ MPa, $R_{q+}=430$ MPa, $R_{q-}=260$ MPa, $R_{ql}=R_{lt}=50$ MPa, $R_{qt}=40$ MPa. For investigations of delamination the inter-laminar strength values are reduced by a weakening factor of $f_{wI}=0.8$ (see Puck [1996]). All strengths are FPF-strengths.

5.4.3 Results

Characteristic distance a_0

The presented results are based on a fixed value of the characteristic distance (a_0) and are taken as one ply thickness. In order to verify this assumption material tests were performed on $[0]_6$ woven fabric laminates with a ply thickness of 0.35 mm. FPF-strengths,

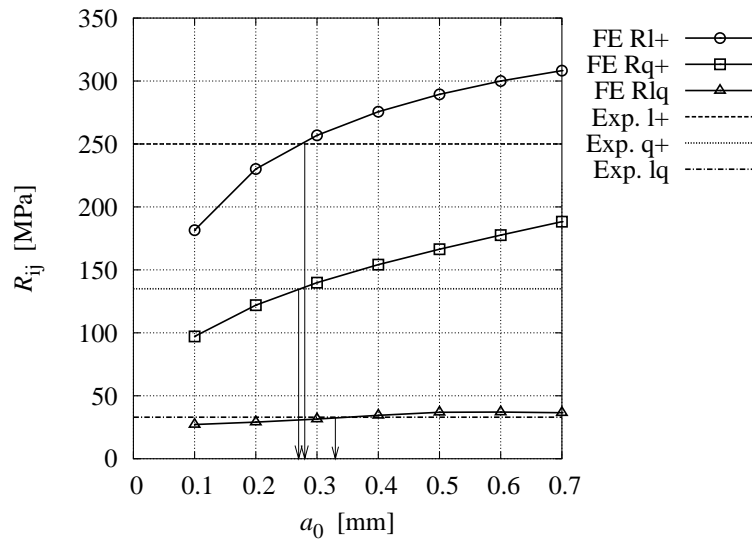


FIGURE 5.12: Evaluation of a_0 based on numerical and experimental results for a $[0]_6$ woven fabric laminate for $G_{lq}=2.55$ GPa

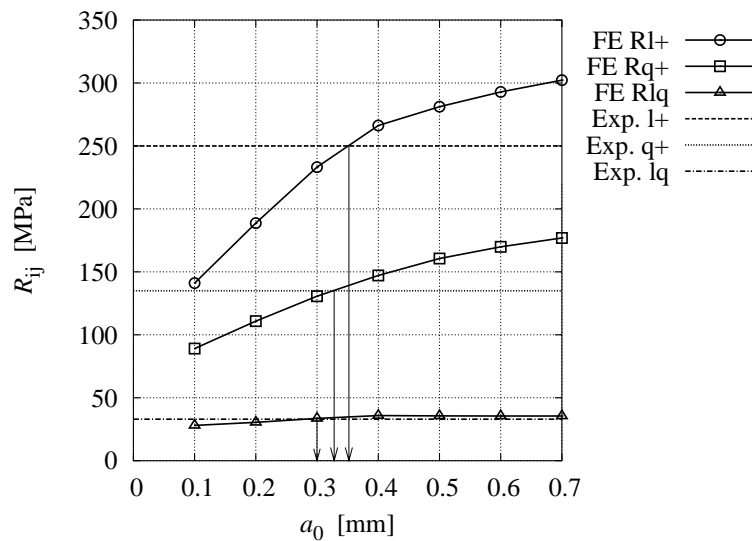


FIGURE 5.13: Evaluation of a_0 based on numerical and experimental results for a $[0]_6$ woven fabric laminate for $G_{lq}=4.0$ GPa

which are defined here as the first deviation from the linear stress-strain curve, were found to be $R_{l+}=250$ MPa , $R_{q+}=135$ MPa, $R_{ql}=30$ MPa. The compressive FPF strengths were not determined. The characteristic distance for the material system can be ob-

tained by comparing the test results with FE-results as shown in FIGURE 5.12 where the FPF strengths are computed for different a_0 values. Using the above FPF strengths a_0 lies between 0.27 and 0.33 mm.

Because of the fact that the material properties are taken from previous investigations, the material properties may show a significant error. Especially the shear modulus $G_{lq}=2.41$ GPa appears to be very low. If, for example, the above investigations are done for a shear modulus of $G_{lq}=4.0$ GPa the results shown in FIGURE 5.13 are obtained. Using the FPF strength values, a_0 lies between 0.3 and 0.35 mm, which gives slightly higher averaging distances. For the following investigation a conservative value of $a_0=0.25$ mm was chosen.

Note that for a $[0]_6$ laminate a_0 is only influenced by the geometric stress concentration and not by free edge stresses.

Comparison of square and hex arrangements of holes in a $[0]_6$ -laminate

First we start with the investigations of the hole arrangement. The angular dependence of the engineering moduli E and G are shown in FIGURE 5.14 and 5.15. It can be seen that the square arrangement (denoted with REC in FIGURE 5.14 and 5.15) shows a better longitudinal stiffness behavior (especially in the 2-direction) and a better shear stiffness than the hexagonal arrangement. In general the longitudinal off-axis behavior of both arrangements is very poor. The effective longitudinal stiffness in the 1- and 2-direction (in comparison with the non-perforated laminate, denoted with NP) reaches about 70% in the square case and about 68% and 55% for the hexagonal case in 1- and 2-direction, respectively.

The strength behavior is plotted in FIGURES 5.16-5.18. The plotted strengths are the minimum strengths of all failure criteria. Except for pure shear loading, the square arrangement shows a better strength behavior. The strength reduction due to the perforations is about 47-50% for the square arrangement and about 30-60% for hexagonal arrangement. The failure mode for pure tensile loading in 1- and 2-directions is fiber fracture and for pure shear and compression loading matrix fracture.

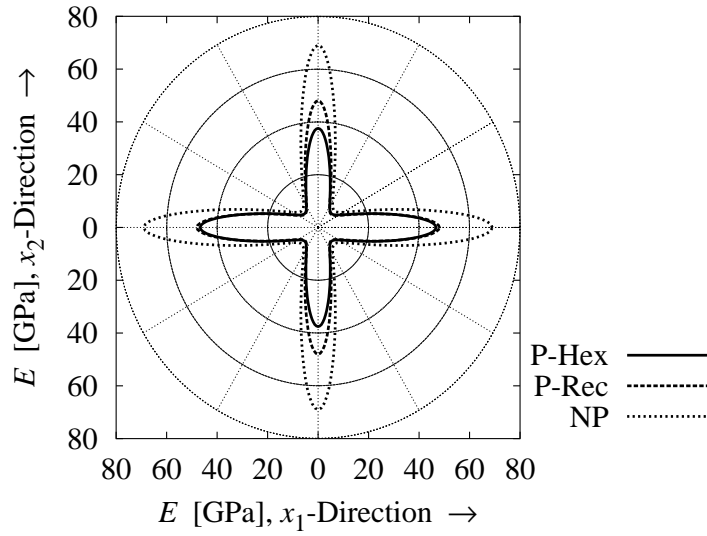


FIGURE 5.14: E -Modulus: Comparison of square and hex arrangement

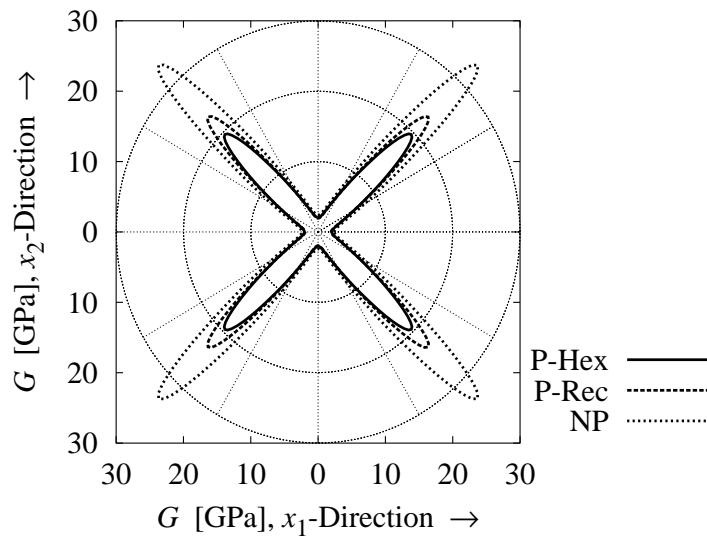


FIGURE 5.15: G -Modulus: Comparison of square and hex arrangement

Square arrangement: Investigations of different diameters of holes in a $[0]_6$ -laminate

In the next step the influence of different hole diameters is investigated. The characteristic distance is kept constant which is a valid assumption for small diameter changes.

The effective stiffness reductions are 70% for E_1 and 80% for G in all three cases,

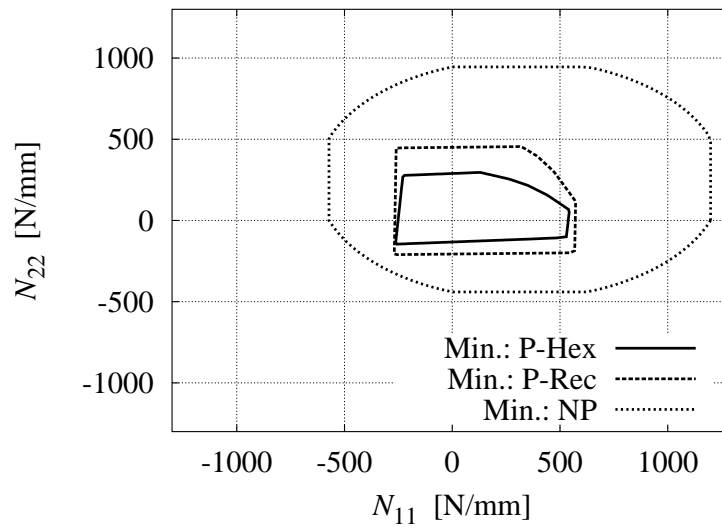


FIGURE 5.16: N_{11} - N_{22} failure curves: Comparison of square and hex arrangements for a $[0]_6$ CFR woven fabric laminate

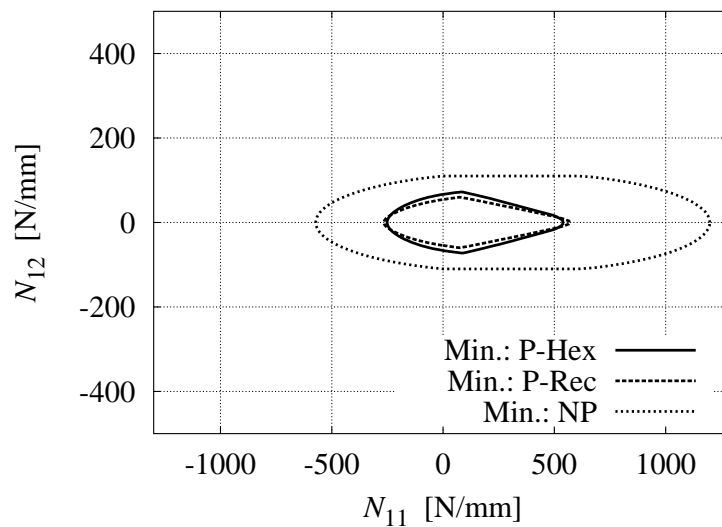


FIGURE 5.17: N_{11} - N_{12} failure curves: Comparison of square and hex arrangements for a $[0]_6$ CFR woven fabric laminate

i.e. there is no influence of the hole diameter on the stiffness behavior if the perforated area is kept constant. Results of the strength investigations are shown in FIGURES 5.19 and 5.20. The N_{22} - N_{12} failure curves are not shown because they look similar to the N_{11} - N_{12} failure curves. It is interesting to see in FIGURE 5.20 that the failure curves

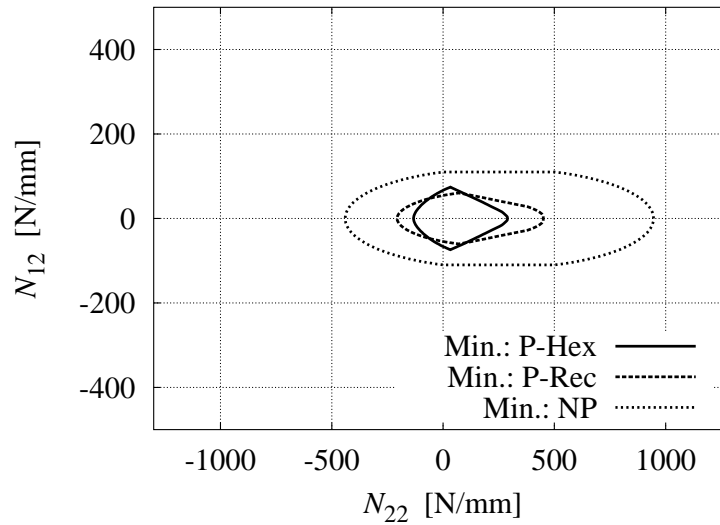


FIGURE 5.18: N_{22} - N_{12} failure curves: Comparison of square and hex arrangements for a $[0]_6$ CFR woven fabric laminate

are likely to be scaled by the hole diameter. In FIGURE 5.19 the behavior looks mostly the same, only in the case of a combined tensile loading in 1- and 2-direction a breakdown in the strengths appears mainly for $D = 0.8$ and 1.55 mm. The reduction of the tensile/compressive strength are 55%, 47% and 38% for $D = 0.8$, 1.55 and 3.0 mm.

Comparison of square and hex arrangements of holes in a $[0/45/0]$ -laminate

Up to this point 2/D FE-models were sufficient for the stiffness and strength investigations. For a $[0/45/0]$ -laminate the influence of the free edge stresses is very strong and 3/D FE-models are necessary. The deformation pattern of the laminate in FIGURE 5.21 shows the deformation of the free edge around the hole. Obviously any shell theory based on linear displacements over the shell thickness must fail here.

These effects lead, on one hand, to a difference in the predicted 2/D and 3/D stiffnesses, see FIGURE 5.22. For both arrangements of holes the difference between the 2/D and 3/D stiffness predictions lies between 5-10% and comes mainly from the kinematic over-constraint due to the shell theory. The difference between square and hexagonal arrangements is very small.

On the other hand the above mentioned free edge effect influences the 2/D and 3/D strengths predictions strongly as can be seen in FIGURES 5.23-5.25. A big difference

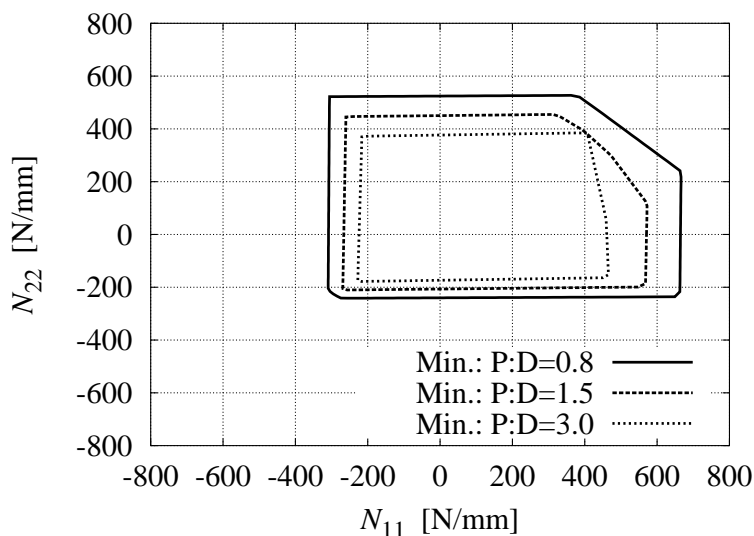


FIGURE 5.19: N_{11} - N_{22} failure curves for a $[0]_6$ CFR woven fabric laminate: Square arrangement, $D=0.8, 1.55, 3.0$ mm

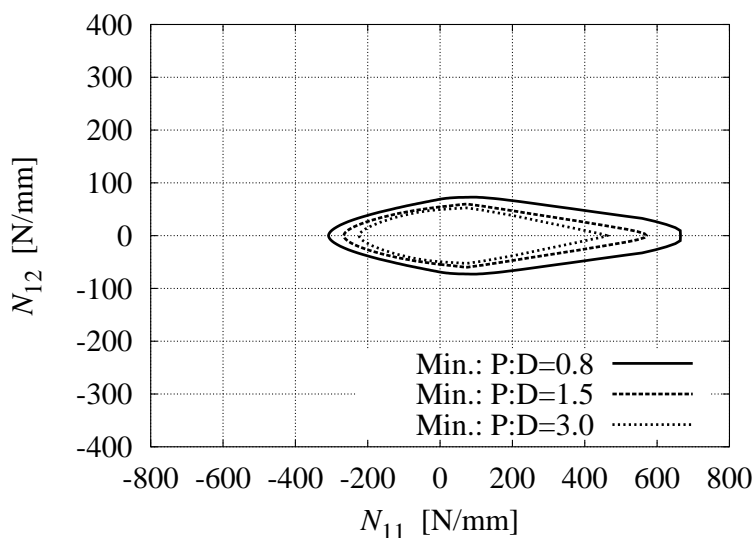


FIGURE 5.20: N_{11} - N_{12} failure curves for a $[0]_6$ CFR woven fabric laminate: Square arrangement, $D=0.8, 1.55, 3.0$ mm

between the $2/D$ and $3/D$ FE results can be observed in the case of pure tension in 1- and 2-directions. The tensile/compressive (shear) strength reduction lies between 32-34% (56%) for the hexagonal arrangement and between 36-39% (46%) for the square arrangement. The values in brackets are the shear strength reductions. The largest

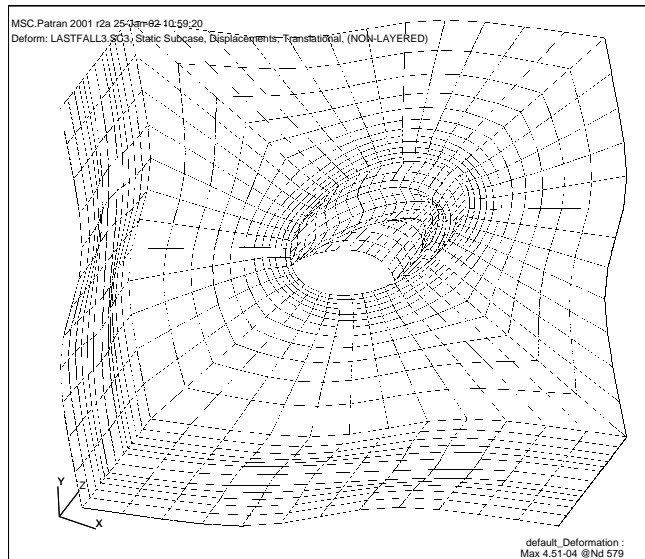


FIGURE 5.21: Shear deformation of a $[0/45/0]$ -laminate with square arrangement of holes

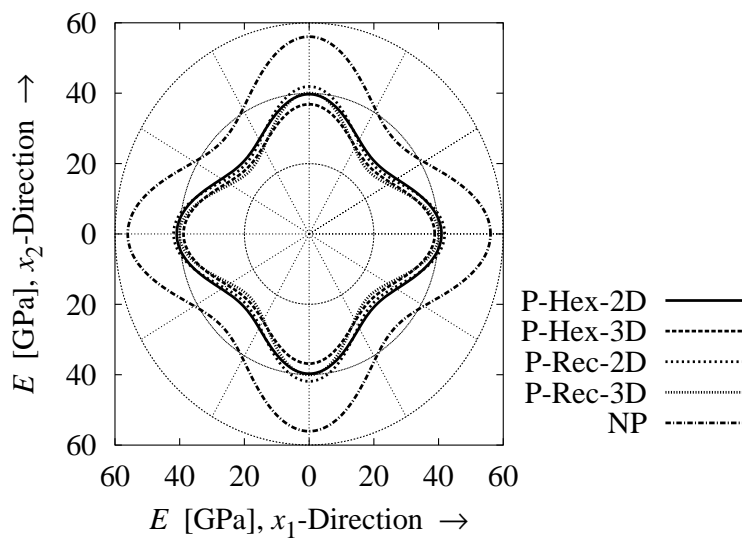


FIGURE 5.22: Young’s modulus of $[0/45/0]$ CFR woven fabric laminates: Comparison of square and hex arrangements 2D and 3D

discrepancy between the 2/D and 3/D solutions is observed for the hexagonal case (tension in 1-direction) with a value of 37%.

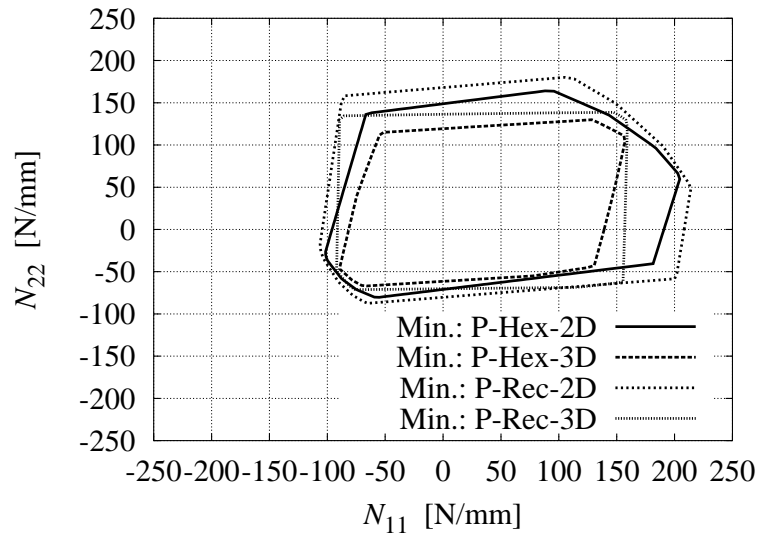


FIGURE 5.23: N_{11} - N_{22} failure curves for a $[0/45/0]$ CFR woven fabric laminate: Comparison of 2D and 3D models of square and hex arrangements

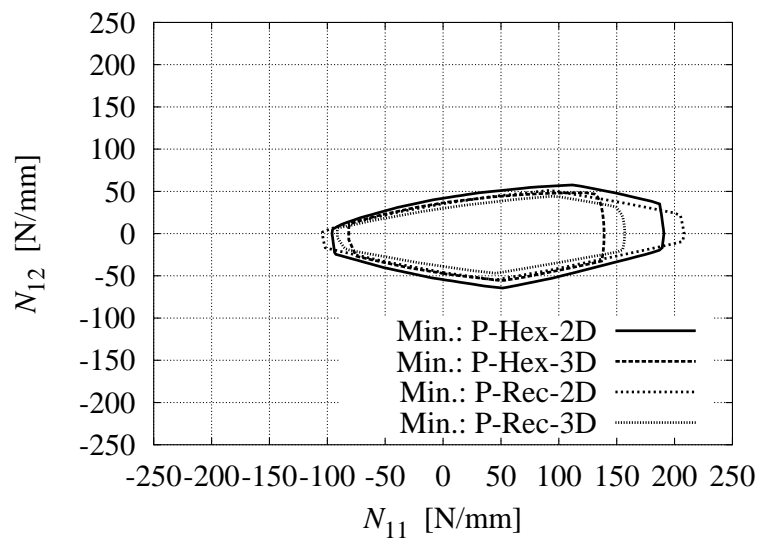


FIGURE 5.24: N_{11} - N_{12} failure curves for a $[0/45/0]$ CFR woven fabric laminate: Comparison of 2D and 3D models of square and hex arrangements

Comparison between failure modes of non-perforated and perforated (3D) $[0/45/0]$ -laminates

Finally the different failure modes for a perforated and a non-perforated plate are compared for a hexagonal arrangement of holes in FIGURES 5.26 and 5.27. The N_{22} - N_{12} fail-

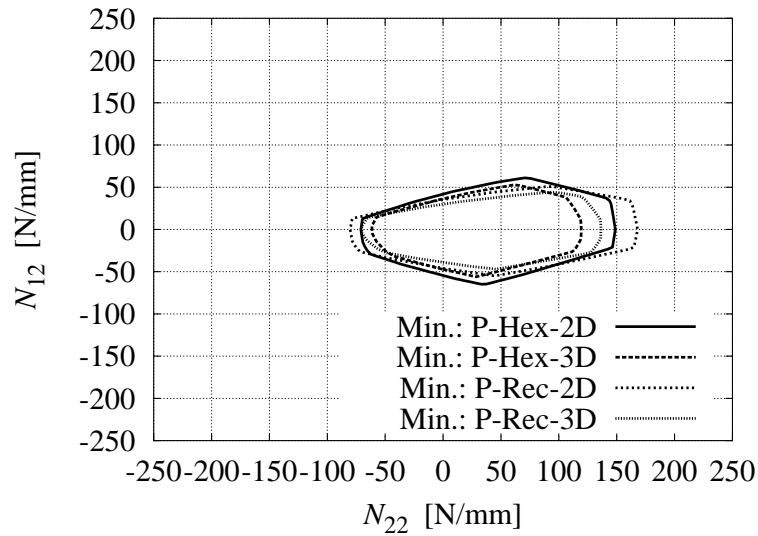


FIGURE 5.25: N_{22} - N_{12} failure curves for a [0/45/0] CFR woven fabric laminate: Comparison of 2D and 3D models of square and hex arrangements

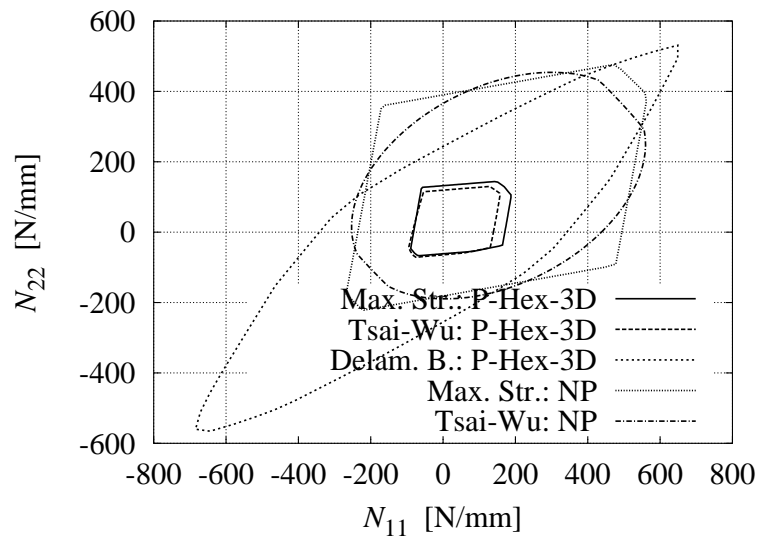


FIGURE 5.26: N_{11} - N_{22} failure curves for a [0/45/0] CFR woven fabric laminate: Failure modes of non-perforated and perforated laminates

ure curves are not shown because they look very similar to the N_{11} - N_{12} failure curves. The first three curves show the failure modes of a perforated laminate. The Tsai-Wu and maximum stress curves are very close together and the delamination failure curves are

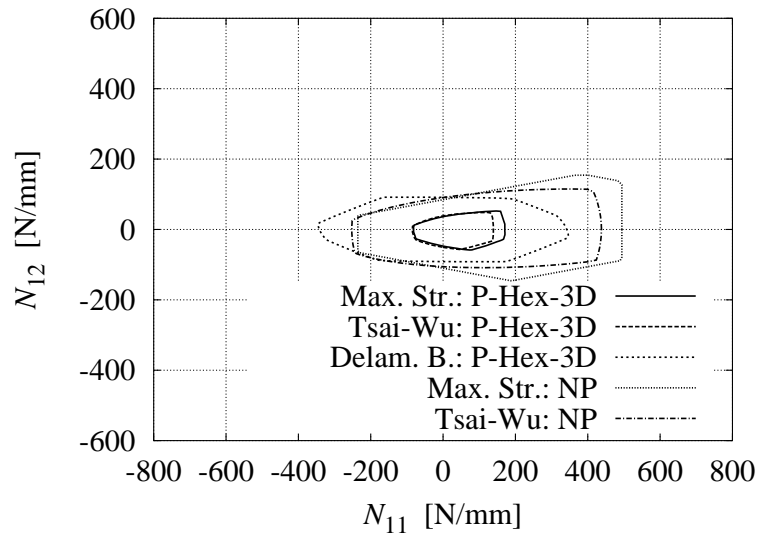


FIGURE 5.27: N_{11} - N_{12} failure curves for a [0/45/0] CFR woven fabric laminate: Failure modes of non-perforated and perforated laminates

not critical at all. That means delamination is not critical for the investigated material system. The last two curves show the failure modes of a non-perforated woven fabric. In FIGURE 5.26 it can be seen where the failure location jumps from one ply to the other ply (because the Tsai-Wu failure curve is not an ellipsoid as in the non-perforated case) and also the intersections between the Tsai-Wu and maximum stress failure curves are evident.

5.4.4 Global Analyses

For validation of the two-scale analysis strategy it is applied to a perforated tensile test specimen. The results are displayed in FIGURE 5.28. The upper picture shows the simulated risk parameters for the FPF load level of 5100 N and are based on FPF strength values (shown in 5.13). On the one hand up to this uncritical load level the specimen is homogeneously loaded in the middle part where the extensometers are mounted during the experiment and the risk parameter is approximately 1. On the other hand there are regions where the risk parameter is about 1.15 and crack initiation will start in these regions. For this reason most of the tested specimens failed in these regions. One of these specimens is shown in FIGURE 5.28 (lower picture). This means critical regions can be detected at the structural level and a proper re-design can be performed based

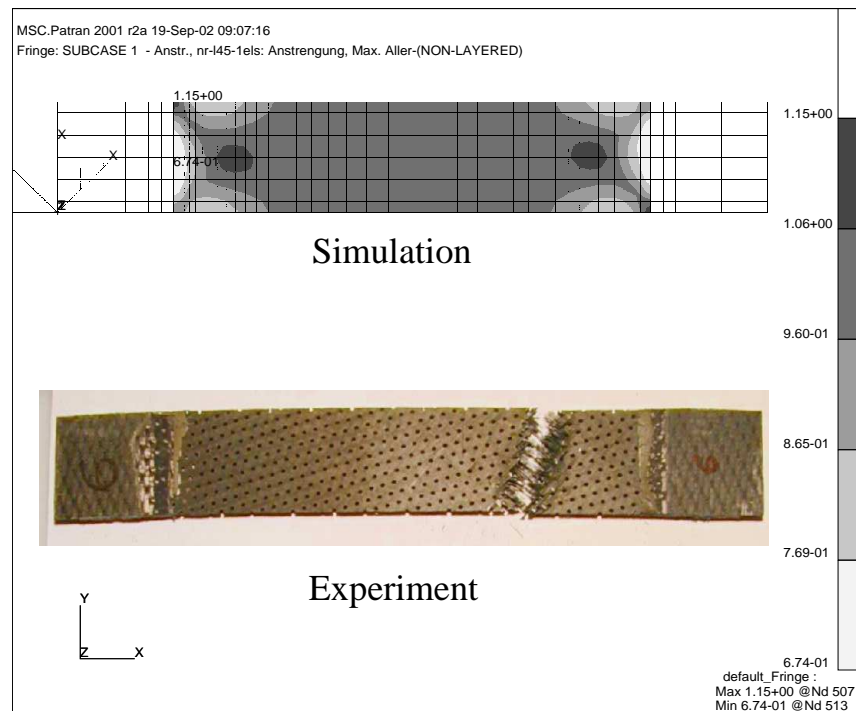


FIGURE 5.28: Comparison of simulation and experiment of a $[0]_6$ woven fabric carbon fiber laminate of a hexagonal arrangement of holes, $t^{\text{lam}} = 2.24$ mm, $D = 1.55$ mm

on the failure information within the perforated regions.

5.5 Investigations of Perforated Woven Fabric Laminates - Material System II

The unit cell model is similar to that in Section 5.4, but the hole arrangement and the material system are different. The investigations in this section are based on comprehensive material tests which are summarized in Section 4. Thus, more emphasis is put on the comparison with test results, and only one arrangement of holes and one lay-up of the perforated laminate is considered.

5.5.1 Geometry

The notations for the unit cell are shown in FIGURE 5.2. In this section the following dimensions are used: $D=1.55$ mm, $l_1=4.44$ mm, $l_2=3.65$, and $d_2=2.22$.

5.5.2 Material Model

Two different material models, a woven fabric and a laminate consisting of UD plies (equivalent uni-directional laminate model), are used for stiffness analyses of the unit cell. For the failure analysis only the woven fabric material model is used, because no strength properties are available for the equivalent uni-directional layer material model.

The lay-up of the woven fabric model is $[0/45/90]$ with a ply thickness of 0.305 mm. The used material properties and strength values are given in TABLE 5.1, where f_{wl} is the interface weakening factor and K is the Tsai-Wu interaction parameter. The determination of the material parameters is summarized in Section 4.3.3 and Section 4.4. The first ply failure strength values $R_{ll}^{(+)}$ and $R_{qq}^{(+)}$ are averaged and the mean value is used for both strengths.

Since the diameter of the holes (1.55 mm) is of the same order as the width of the rovings (3.0 mm) of a woven ply, an alternative approach based on equivalent uni-directional layers $[0/90/45/-45/90/0]$ is also considered. The slight unsymmetry of this lay-up is disregarded. The chosen material parameters for this case are shown in TABLE 5.2. As mentioned above, there are no strength values available for the uni-directional layer model. The material parameters listed in TABLE 5.2 are chosen such that the same non-perforated stiffness behavior of the investigated unit cell is obtained,

TABLE 5.1: Engineering moduli and first ply failure strength of a CFR woven fabric ply

Variable	Value	Variable	Value
E_l	57.6 GPa ^c	$R_{ll}^{(+)} = R_{qq}^{(+)}$	455 MPa
E_q	57.6 GPa ^c	$R_{ll}^{(-)} = R_{qq}^{(-)}$	210 MPa
$E_t = (E_q)_{UD}$	10 GPa ^a	$R_{tt}^{(+)}$	60 MPa ^b
G_{lq}	4.0 GPa ^c	$R_{tt}^{(-)}$	180 MPa ^b
$G_{qt} = G_{lt}$	4.0 GPa	$R_{ql} = R_{tl} = R_{qt}$	73 MPa
ν_{lq}	0.03	f_{wI}	0.8 ^b
$\nu_{qt} = \nu_{lt} = (\nu_{lt})_{UD}$	0.2 ^a	K	0.0

^a ... from the uni-directional layer model (see TABLE 5.2)

^b ... taken from the literature (see Puck [1996])

^c ... modified values from material tests (see Section 4.3.3)

TABLE 5.2: Material parameters of an equivalent uni-directional CFR ply

Variable	Applied Value
E_l	106 GPa
$E_q = E_t$	10 GPa
G_{lq}	4.0 GPa
$G_{qt} = G_{lt}$	4.0 GPa
$\nu_{lq} = \nu_{qt} = \nu_{lt}$	0.2

regardless whether the woven layer or the uni-directional layer lay-up is chosen for the unit cell. The investigations with uni-directional layers are mainly performed to study the influence of a larger number of interfaces on the stiffness behavior.

5.5.3 Stiffness Behavior of Perforated Laminates

For the calculation of the overall stiffness behavior a mesh of the unit cell as shown in FIGURE 5.3 is used. Comparisons with finer mesh densities have shown that, with respect to the effective stiffness behavior, the differences are smaller than 2%.

Various models are available for the stiffness evaluation of a perforated laminate,

where all described models are based on finite element analyses. They can be summarized as:

1. 2D unit cell model (denoted with “UC: 2D” in the following). This model is based on finite element computations of laminated shell elements, where only two in-plane displacement degrees of freedom are active. One kinematic constraint of this model is, that the displacements (strains) are constant over the thickness of the 2D element.
2. 3D unit cell model (denoted with “UC: 3D” in the following). A mesh of this model is shown in FIGURE 5.3. The individual layers are CFR woven fabric layers with material parameters shown in TABLE 5.1.
3. 3D equivalent uni-directional ply unit cell model (denoted with “UC: 3D-UD” in the following). The model is similar to the “UC: 3D” model. The difference is that each woven fabric layer is split into a 0° and 90° uni-directional layer with material parameters shown in TABLE 5.2.
4. Unit cell model in conjunction with Classical Lamination Theory (denoted with “UC: CLT” in the following). This model is based on CLT, where the layer material is obtained from 2D finite element unit cell analyses of a single perforated woven fabric layer.

A sketch which demonstrates the differences between the individual models is shown in FIGURE 5.29. There, possible free edge deformations at a hole are sketched for each model. Obviously the “UC: CLT” is the softest model, because the local effects around the hole are neglected due to the utilization of effective perforated material parameters. Regarding the softness behavior this model is followed by the “UC: 3D-UD” and “UC: 3D” models. The stiffest model is the “UC: 2D”, since the displacements over the thickness are constant.

A verification of these model effects is given in FIGURE 5.30, where the various models are compared with test results. The best agreement with the test results is obtained from the 3D models. The effective moduli of these models and the measured moduli lie between those of the “UC: 2D” model and the “UC: CLT” model, which are upper and lower bounds, respectively. A noticeable influence of the “unconstrained” free edge around the hole in the 3D case is observed in FIGURE 5.30 if the 2D and 3D results are compared with each other. The calculated stiffness based on 3D computations seems to

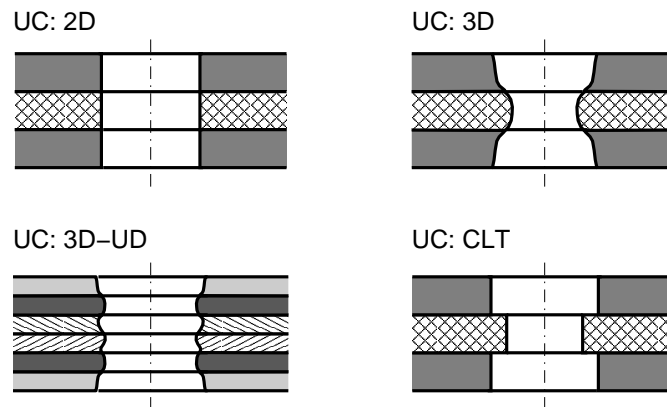


FIGURE 5.29: Sketch of possible free edge deformations around a hole in the models used for the calculation of the stiffness of perforated laminates

deliver quite realistic values for the perforated plate. A slight overestimation of the actual stiffness, however, must be assumed. The reason for this may be a reduced stiffness in the inter-phases between adjacent plies (imperfect bonding), as well as the fact that a “larger number” of sublayers in the model, which take the roving structure into account in more detail, would lead to a further stiffness decrease. Nevertheless, the “UC: 3D-UD” and “UC: 3D” models lie within the standard error-bars (which are two times the standard deviation) of the measured results.

As mentioned in Section 4.3.3 an uncertain parameter of the material model is the shear modulus. Therefore, the effective engineering moduli of a perforated CFR woven fabric laminate are calculated for three different shear moduli with the “UC: 3D” model and compared with material tests. The results are shown in FIGURE 5.31. It can be seen that for a small shear modulus of $G_{12}=2.55$ GPa the agreement with test results is excellent. In contrast, a high shear modulus of $G_{12}=5.8$ GPa lets the predicted effective shear modulus fall out of the error-bars. It should be mentioned that a small shear modulus “fits” the test results best, which does not mean that it is a realistic value (see Section 4.3.3) due to non-linear shear response (see Section 4.3.2).

5.5.4 Deformation Patterns

The deformation patterns of the “UC: 3D” model according to the three basic load cases is shown in FIGURE 5.32. It becomes obvious from the details that the assumptions

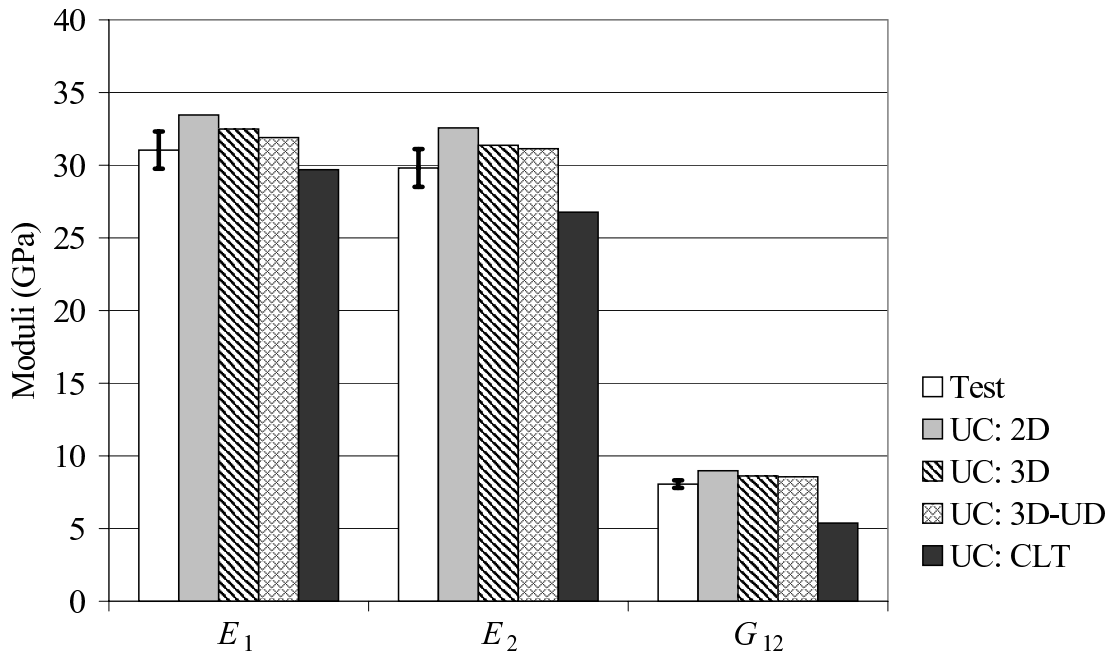


FIGURE 5.30: Comparison of engineering moduli of a perforated [0/45/90] CFR woven fabric laminate based on various evaluation methods

of the CLT (linear displacement field over the thickness of the plate) are violated not only around the hole but also within the unit cell. The periodic displacement fields can also be seen for each unit cell, i.e., the considered unit cell can be translated along the periodicity vectors, and the corresponding surfaces fit into one another.

5.5.5 Failure of Perforated Laminates

The investigations of ply failure and delamination, which are described in this section, are based on a 3D finite element unit cell model with hexagonal hole arrangement. Hence, the influence of free edge effects is taken into account.

First it is worth to remark again that in the following the notation “strength” of a laminate means the critical membrane force state for first appearance of failure within one of the layers at the considered area of the laminate (FPF), being different from LPF. This means that it is not the membrane force state at which the specimen fails totally.

The goal of the failure analysis is to calculate a safety factor ${}^{\text{lam}}\lambda$ or a risk parameter ${}^{\text{lam}}\mathcal{R}$ for any point of global structure which is composed of perforated laminates.

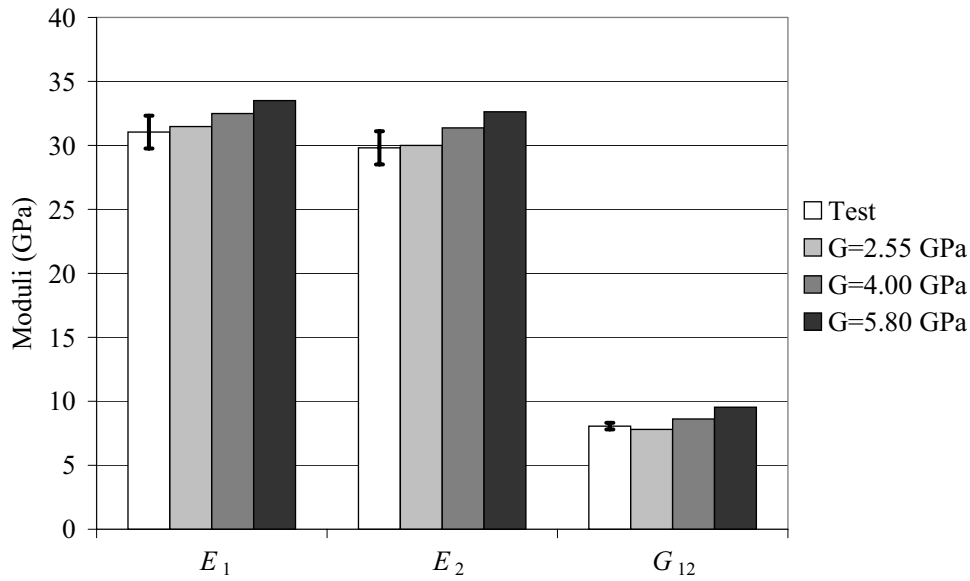


FIGURE 5.31: Effective engineering moduli of a perforated [0/45/90] CFR woven fabric laminate computed with different shear moduli

Therefore, at first the minimum safety factor is evaluated for all possible loading combinations (N_{11}^{hom} , N_{22}^{hom} and N_{12}^{hom}) by *Post-Processor I* (see FIGURE 5.1). The results of these computations, which includes the failure modes fiber failure, matrix cracking and delamination, can be plotted in the N_{11}^{hom} , N_{22}^{hom} , N_{12}^{hom} -space, building up the failure surface. FIGURE 5.33 shows such a critical failure surface (combination of the Tsai-Wu and the maximum failure surfaces), where a cutout shows the failure curves. If the homogenized membrane forces are known at any position of a homogenized laminated shell it is possible to evaluate a safety factor or a risk parameter for the considered position. This work is done by *Post-Processor II* (sketched in FIGURE 5.1). Edges in the overall failure surface are indicative of a change in the failure mode or a change of the position, i.e., the ply, where the failure occurs. This means that the overall failure surface represents the inner envelope of the failure surfaces corresponding to the different failure modes. The corresponding critical point in the unit cell may be located somewhere around the hole but may also lie inside the considered unit cell.

To provide a better insight which failure mode is critical for a given configuration three sections through the failure surfaces corresponding to the individual failure modes are plotted in FIGURE 5.34 - FIGURE 5.36. The superscript "hom" is not written in the following. The comparison of the several failure modes shows that, although

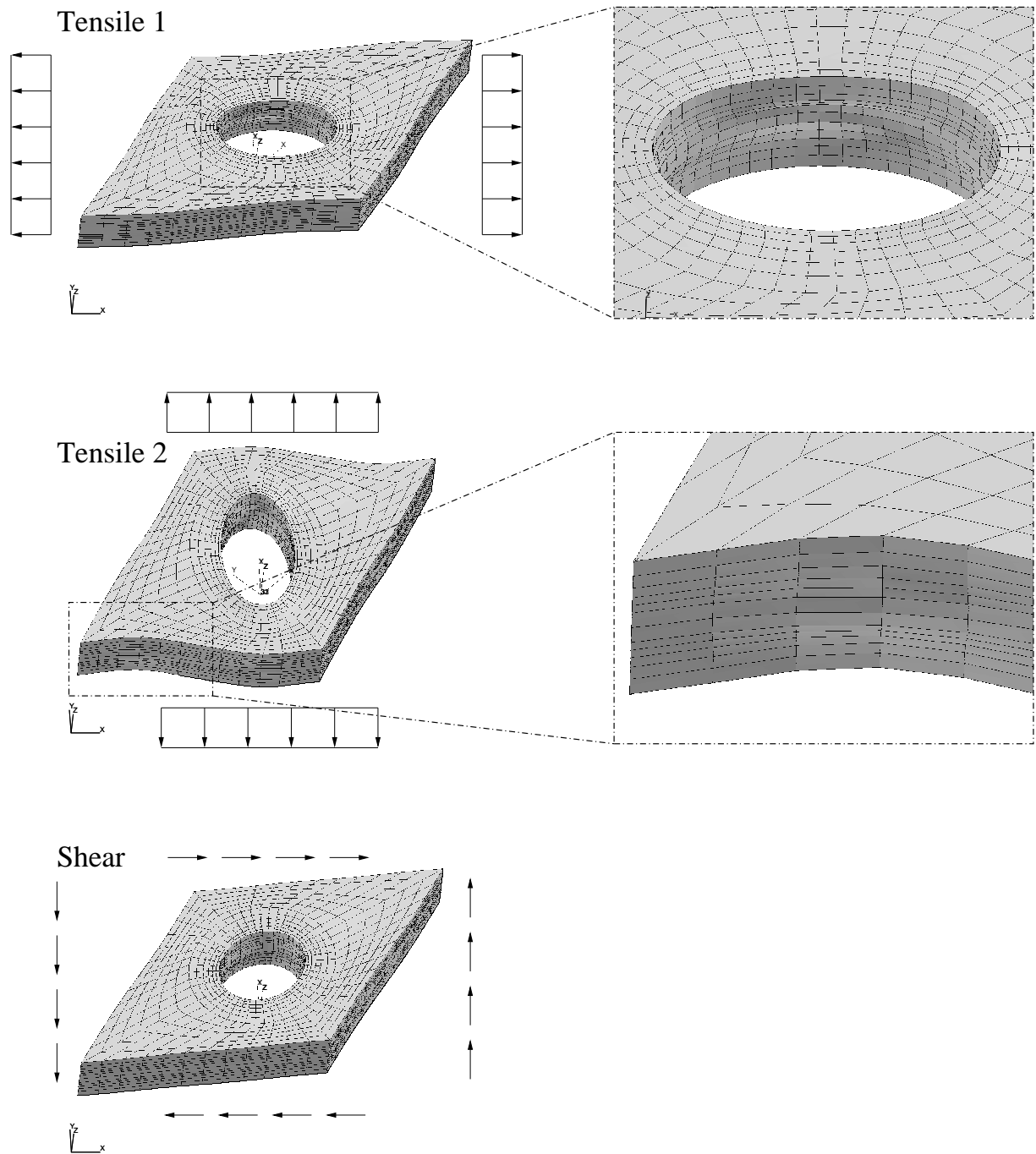


FIGURE 5.32: Deformation patterns of the “UC: 3D” model for tensile loading in 1-direction (top), tensile loading in 2-direction (middle) and shear loading (bottom)

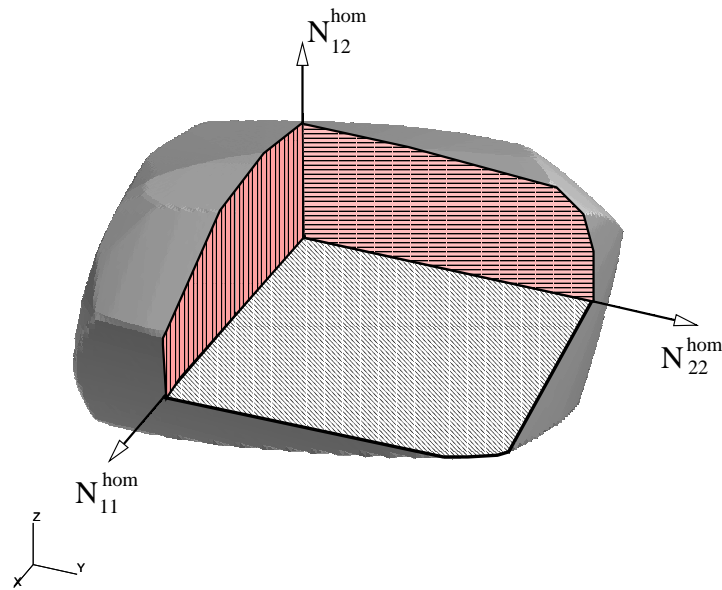


FIGURE 5.33: Critical failure surface with a cutout showing the failure curve

the inter-laminar shear strength of the interface is assumed to be only 80% of the intra-laminar shear strength, the critical failure modes of the investigated UC are always matrix cracking or fiber failure. For predominant loading in 1- and 2-directions the Tsai-Wu failure condition predicts failure first (matrix cracking). If the UC is under compressive loading in 1- and 2-directions the maximum stress failure condition gives the critical value. The Tsai-Wu failure hypothesis slightly overestimates the critical failure load in the case of compressive loading.

A comparison of measured and computed effective FPF strength values of the perforated laminate is shown in FIGURE 5.37, where the averaging distance (a_0) is set to 0.54 mm which is $1.77 t_s$. Very good agreement can be observed. All computed results lie within the error-bars. From this comparison it is evident that the introduced unit cell models are well suited for stiffness and strength predictions of perforated laminates.

All the above results are based on 3D unit cell models. In FIGURE 5.38 the error is shown if 2D models instead of 3D models are used. There, the effective first ply failure strengths $R_{ll}^{(+)}$, $R_{qq}^{(+)}$, and $R_{ql}^{(+)}$ are plotted over the averaging distance, where the open symbols correspond to the 3D calculations and the solid symbols pertain to the 2D computations. First of all a strong dependence of the longitudinal and transverse FPF strengths on the averaging distance is evident, whereas the influence on the shear

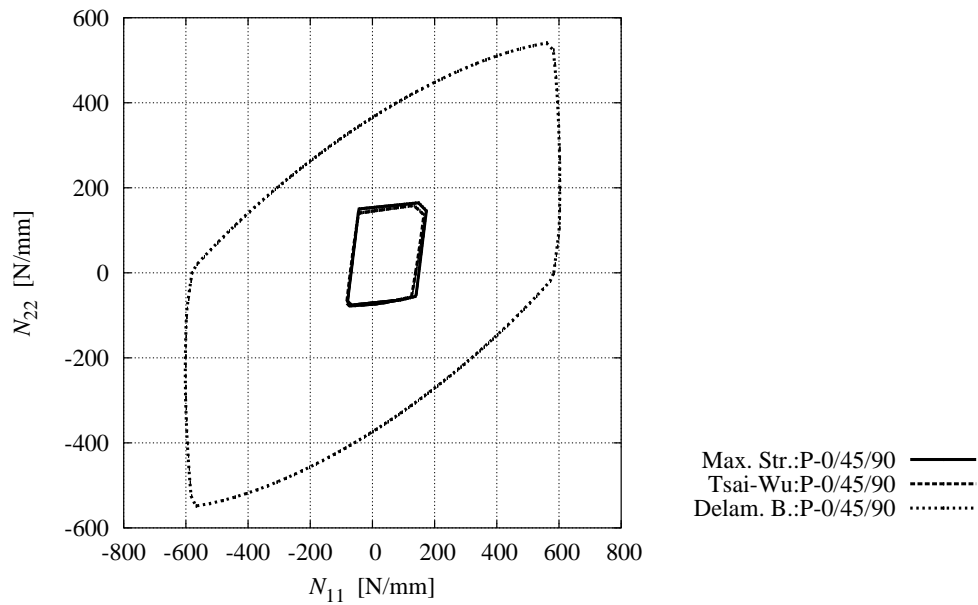


FIGURE 5.34: $N_{11} - N_{22}$ section through the failure surface of a perforated [0/45/90] woven fabric laminate

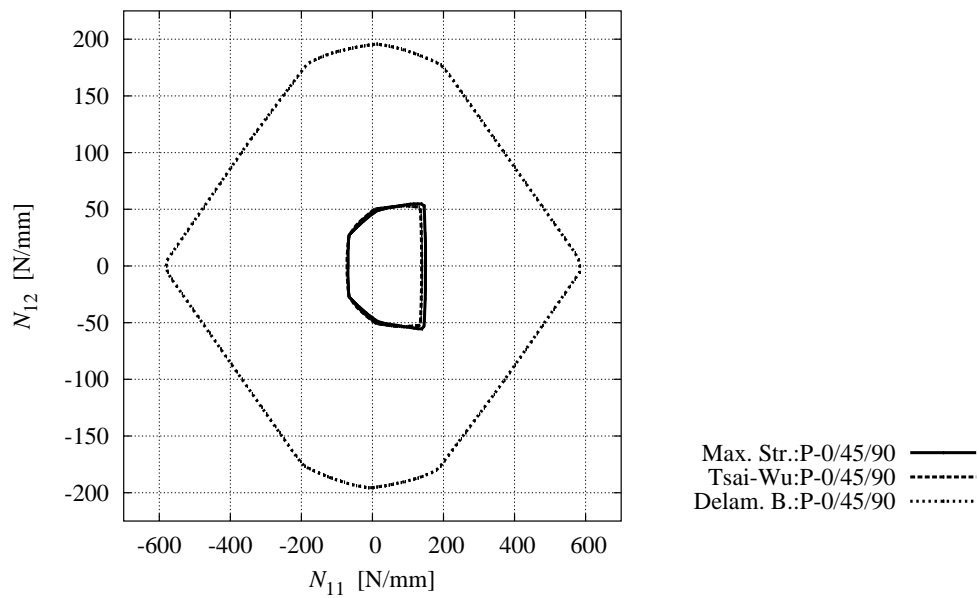


FIGURE 5.35: $N_{11} - N_{12}$ section through the failure surface of a perforated [0/45/90] woven fabric laminate

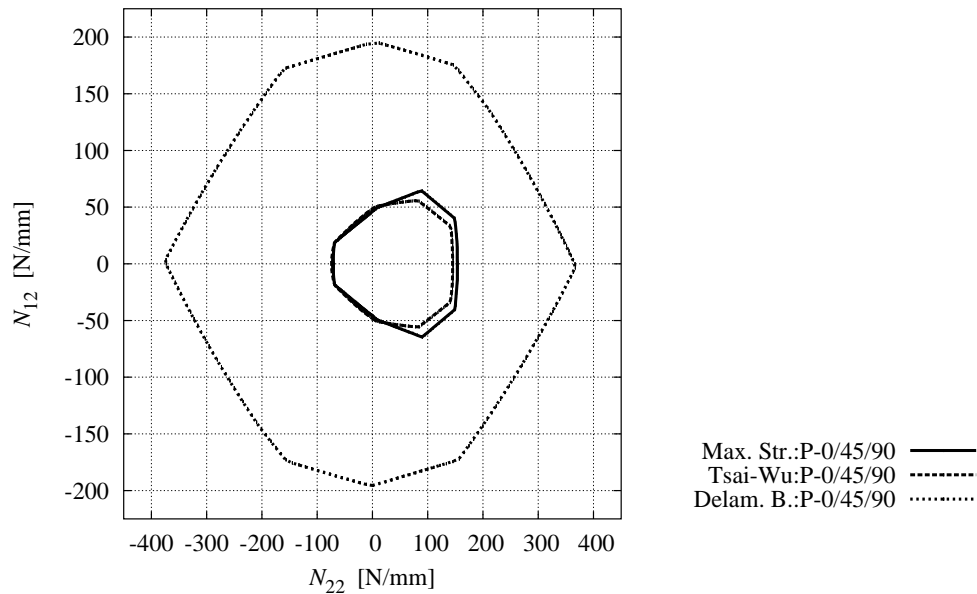


FIGURE 5.36: $N_{22} - N_{12}$ section through the failure surface of a perforated [0/45/90] woven fabric laminate

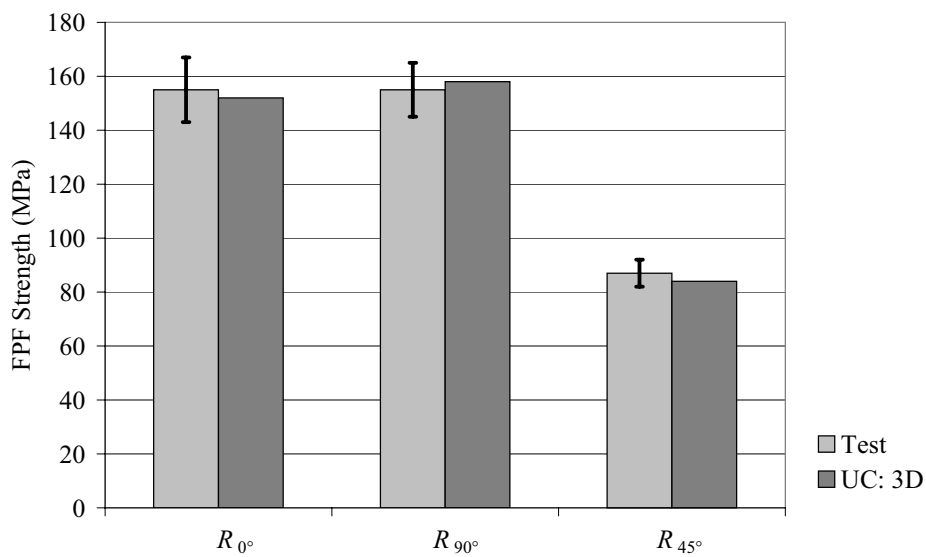


FIGURE 5.37: Comparison of measured and computed effective FPF strength values of a perforated [0/45/90] CFR woven fabric laminate with $a_0 = 0.54$ mm ($1.77 t_s$)

strength is rather small. The difference between the two models is obvious if, for example, the FPF strength is determined for a averaging distance of $a_0 = 0.54$ mm (indicated

by arrows). The FPF strengths are 178.1 MPa and 151.6 MPa for the 2D and 3D models, respectively. The difference of both results is then approximately 18%. The error is much higher if, for example, $R_{ii}^{(+)}$ is given and the averaging distance is determined. In case of $R_{ii}^{(+)}=151$ MPa the obtained averaging distances are 0.31 mm and 0.54 mm for the 2D and 3D model, respectively, which leads to an error of 43%! These results show why 3D unit cell models are necessary for strength predictions for perforated laminates.

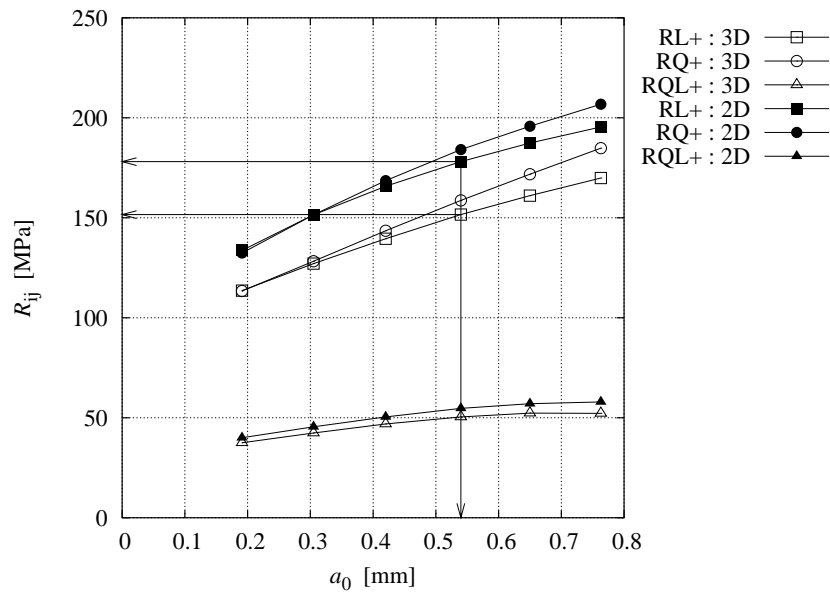


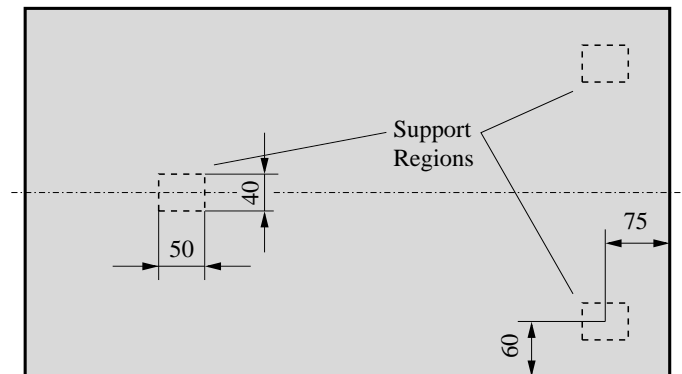
FIGURE 5.38: Predictions of effective FPF strengths of 2D and 3D unit cells as functions of the averaging distance a_0 of a perforated $[0/45/90]$ woven fabric laminate

5.5.6 Application of Two-Scale Modeling

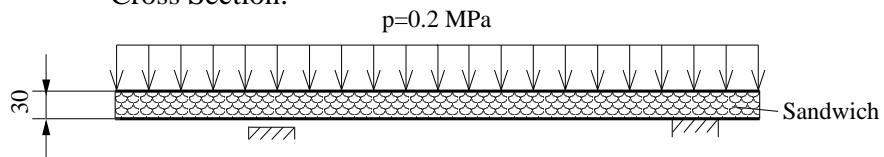
Finally, an application of the two-scale modeling is presented. As mentioned in Section 1.1.3 a typical application of perforated laminates is a blocker door in the thrust reverser unit of a commercial aircraft turbine engine.

A simplified model of the blocker door is shown in FIGURE 5.39. The blocker door consists of a sandwich, where the top skin is partially perforated and the bottom skin is non-perforated. In the model the blocker door is supported by three supports and loaded with a uniform pressure load of 0.2 MPa. The material parameters are given

Bottom View:



Cross Section:



Top View:

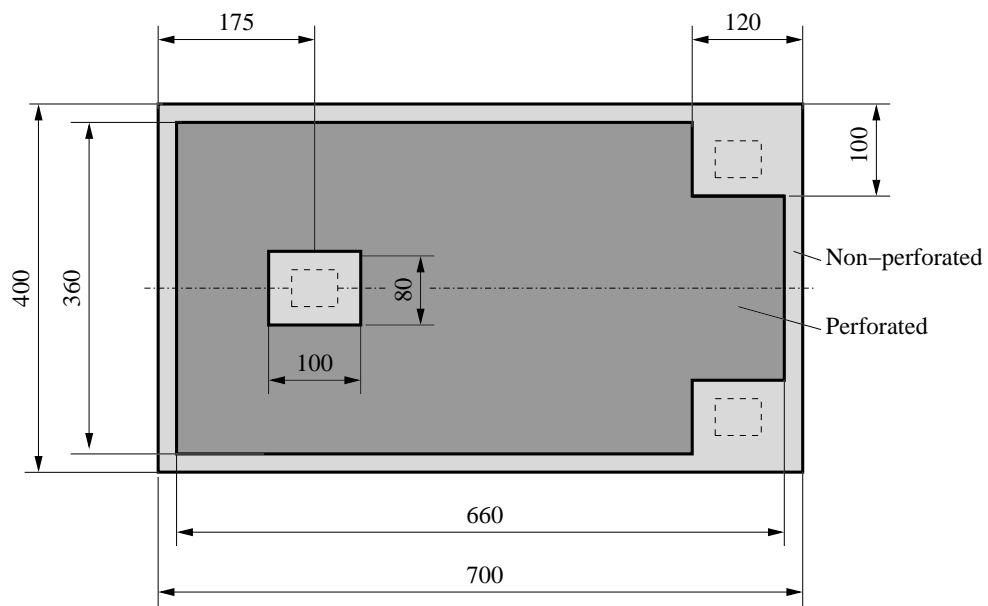


FIGURE 5.39: Simplified model of a blocker door

in TABLE 5.1, and a [0/45/90] lay-up with a ply thickness of 0.305 mm is used for the non-perforated and perforated regions.

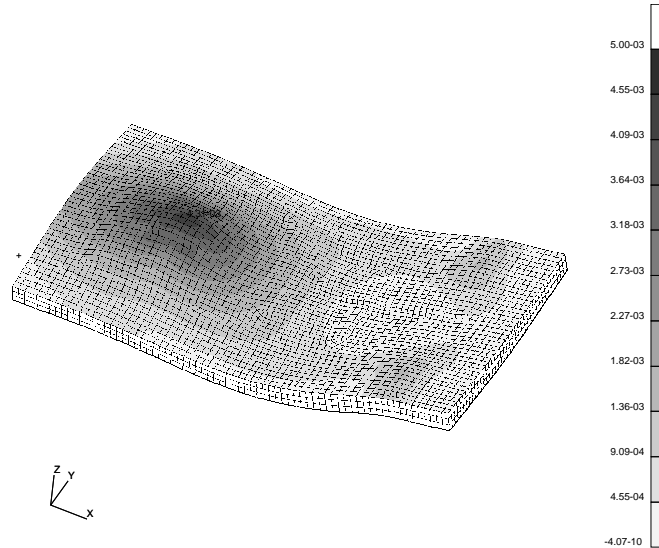


FIGURE 5.40: Maximum principal strains of a blocker door

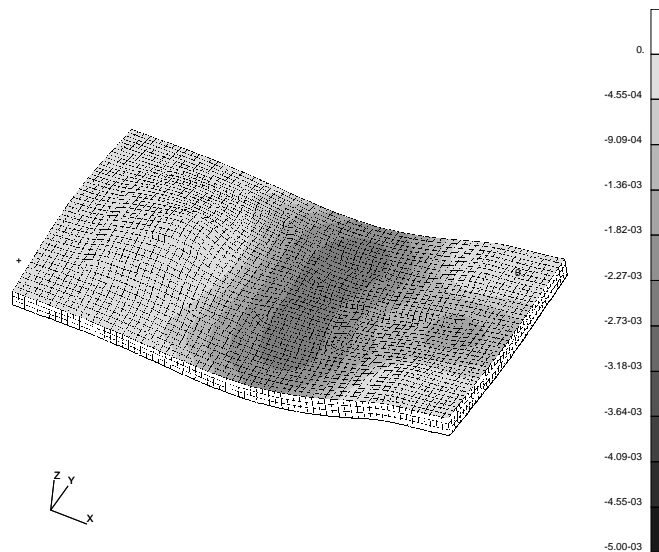


FIGURE 5.41: Minimum principal strains of a blocker door

A common practice in aerospace industry with respect to failure analysis is to compare the maximum and minimum principal strains. FIGURE 5.40 and FIGURE 5.41 show the maximum and minimum principal strains of the blocker door structure. Based on

these figures one hardly can decide which region is more critical, because a bi-axial stress state is evident.

Therefore, the two-scale modeling strategy is introduced and the following analysis steps are carried out for the perforated blocker door structure:

1. Unit cell analysis: As described in Section 5.5.3 and Section 5.5.5 the homogenized stiffness values and the effective first ply failure surface are computed, respectively.
2. Global structural analysis: Next a global FE-shell-analysis of the blocker door is performed with a standard finite element program. The perforated regions are modeled with the effective homogenized stiffness from point (1), and the effective stresses within the perforated regions are calculated.
3. In the last step the effective first ply failure strengths from point (1) and the effective laminate stresses, more precisely the stress resultant N_{ij} , from point (2) are combined. Thus, the risk parameter for the individual failure hypotheses is computed within the perforated region of the blocker door and can be display in a standard Post-processor.

The advantages of the failure results obtained this way are twofold: On the one hand the risk parameter of the perforated blocker door region can be displayed (see FIGURE 5.42) for different failure criteria. On the other hand the predicted failure mode can be shown within the perforated region (see FIGURE 5.43). In combination with the failure information of the non-perforated regions a re-design of the structure can be done easily if it is necessary.

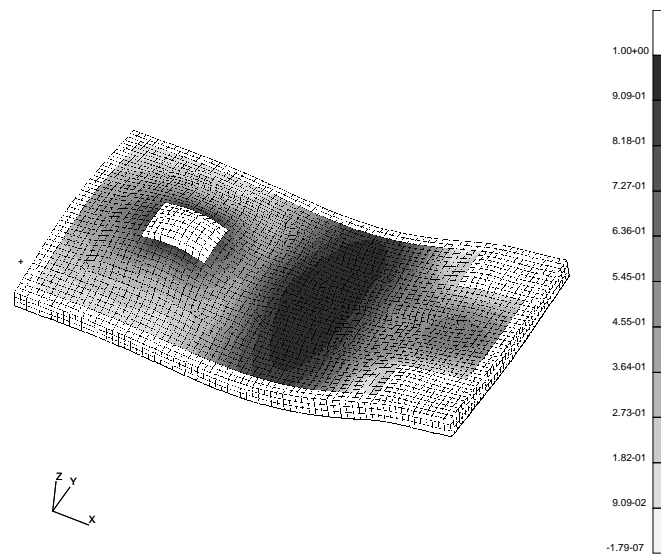


FIGURE 5.42: Maximum risk parameter of the perforated region of the blocker door

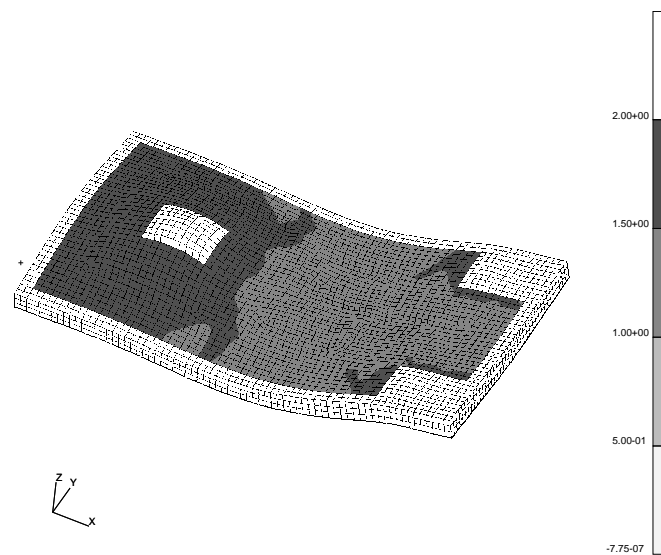


FIGURE 5.43: Failure modes of the perforated region of the blocker door. A value of 1.0 corresponds to the maximum stress criterion (fiber failure) and 2.0 indicates that the Tsai-Wu risk parameter (matrix failure) is the critical one

5.6 Conclusion

A fast two-scale modeling analysis tool is introduced for the prediction of the stiffness and failure behavior of perforated laminates. The obtained results are based on 3D finite element unit cell calculations, where free edge effects are taken into account, and within which first ply failure is considered under averaged stress assumptions.

Comprehensive material tests are performed in order to obtain in-plane stiffness and strength values of non-perforated and perforated woven fabric laminates. Furthermore, inter-laminar shear tests are done on various non-perforated coupon geometries. It is shown that the quality of the measured inter-laminar shear strength strongly depends on the specimen type. In all tests acoustic emission measurements are accomplished parallel to the classical material tests to obtain first ply failure strength values.

Various material systems, a CFR uni-directional and two CFR woven fabric laminates, are investigated. Predominantly numerical parameter studies are performed on the uni-directional material system and on one CFR woven fabric laminate. With respect to failure hypotheses it is found that the Puck criterion is well suited for failure predictions of uni-directionally reinforced laminates, whereas a combined Tsai-Wu and maximum stress criterion is preferable if perforated woven fabric laminates are investigated. Studies of the characteristic distance show that it can be chosen as approximately one ply thickness if it is unknown in advance, which in general leads to conservative results. This way a scale effect becomes visible, explaining why perforations with larger holes lead to decreased strength as compared to laminates with smaller holes that have the same ratio of perforation area.

Further studies deal with the comparison of numerical and experimental results for non-perforated and perforated CFR woven fabric laminates. Very good agreement between the experimental and numerical results (stiffnesses and first ply failure strengths) is achieved. This comparison verifies the presented two-scale modeling analysis strategy on an experimental basis.

Finally an application of the analysis tool is presented which is useful for the design of structures containing perforated laminates. This way the deformation and strength evaluation of structures containing perforated laminates can be performed simply on the structural, i.e., macroscopic level. Furthermore, this procedure is very efficient because the structural analysis does not need to account for the perforation explicitly, neither in the finite element discretization nor in the evaluation of stress fields.

Bibliography

- Adams, D. F. and Lewis, E. Q. (1995). Experimental study of three- and four-point shear test specimens. *J. Comp. Tech. & Research* **17**, pp. 341–349.
- Adams, D. F. and Lewis, E. Q. (1997). Experimental assessment of four composite material shear test methods. *J. Testing & Evaluat.* **25**, pp. 174–181.
- Anthoine, A. (1995). Derivation of the in-plane elastic characteristics of masonry through homogenization theory. *Int. J. Sol. Struct.* **32**(2), pp. 137–163.
- ASM-Handbook (2002). *ASM Handbook - Composites*, volume 21, pp. 766–768. ASM International, Materials Park, OH.
- Baron, J. and S.P., Y. (1990). *Acoustic emission source location*, volume 5, pp. 136–154. American Society of Nondestructive Testing, USA.
- Bassim, M. N. (1990). *Macroscopic origins of acoustic emission*, volume 5, pp. 46–61. American Society of Nondestructive Testing, USA.
- Bathe, K.-L. (1996). *Finite Element Procedures*. Prentice-Hall, Inc., New Jersey, USA.
- Brewer, J. C. and Lagace, P. A. (1988). Quadratic stress criterion for initiation of delamination. *J. Comp. Mat.* **22**, pp. 1141–1155.
- Chimani, C. M. (1998). *Micro- Macromechanical Models for Hybrid, Selectively Reinforced Structures*. Ph.D. thesis, Vienna University of Technology.
- Chu, G. G. and Sun, C. T. (1993). Free edge and size effects on failure initiation and ultimate strength of laminates containing a center hole. In: *Proc. of 9th Int. Conf. on Composite Materials (ICCM/9 '93), July 12–16, 1993, Madrid, Spain*.
- Eitzen, D. and Breckenridge, F. R. (1990). *Acoustic emission sensors and their calibration*, volume 5, pp. 122–134. American Society of Nondestructive Testing, USA.

- Hassani, B. and Hinton, E. (1998a). A review of homogenization and topology optimization I-homogenization theory for media with periodic structure. *Comput. and Struct.* **69**, pp. 707–717.
- Hassani, B. and Hinton, E. (1998b). A review of homogenization and topology optimization II-analytical and numerical solution of homogenization equations. *Comput. and Struct.* **69**, pp. 719–738.
- Hill, R. (1963). Elastic properties of reinforced solids: Some theoretical principles. *J. Mech. Phys. Solids* **11**, pp. 127–140.
- Hinton, M. J. and Soden, P. D. (1998). Predicting failure in composite laminates: The background to the exercise. *Comp. Sci. and Tech.* **58**, pp. 1001–1010.
- Iarve, E. V. and Pagano, N. J. (2001). Singular full-field stress in composite laminates with open holes. *Int. J. Sol. Struct.* **38**, pp. 1–28.
- Jones, R. M. (1999). *Mechanics of Composite Materials*. Taylor and Francis Inc., Philadelphia, USA, 2nd edition.
- Juhasz, J., Rolfes, R. and Rohwer, K. (2001). A new strength model for application of a physically based failure criterion to orthogonal 3d fiber reinforced plastic. *Comp. Sci. and Tech.* **61**, pp. 1821–1832.
- Kirsch, G. (1898). Die Theorie der Elastizität und die Bedürfnisse der Festigkeitslehre. *VDI* **42**, p. 797.
- Ladevèze, P. (2001). *Handbook of Material Models*, chapter 10.6, pp. 1004–1013. Academic Press.
- Ladevèze, P. and Lubineau, G. (2002). An enhanced mesomodel for laminates based on micromechanics. *Comp. Sci. and Tech.* **62**, pp. 533–541.
- Lekhnitskii, S. G. (1936). Stresses in infinite anisotropic plate weakened by elliptical hole. *DAN SSSR* **4**.
- Mang, H. and Hofstetter, G. (2000). *Festigkeitslehre*. Springer Verlag, Wien.
- McBride, S., Boyce, W., Perschbacher, J. P. and Pless, W. (1990). *Acoustic emission applications in the aerospace Industry*, volume 5, pp. 418–445. American Society of Nondestructive Testing, USA.

- Michel, J. C., Moulinec, H. and Suquet, P. (1999). Effective properties of composite materials with periodic microstructure: a computational approach. *Comput. Meth. Appl. Mech. Eng.* **172**, pp. 109–143.
- Ng, S. P., Lau, K. J. and Tse, P. C. (2000). 3D finite element analysis of tensile notched strength of 2/2 twill weave fabric composites with drilled circular holes. *Composites Part B* **31**, pp. 113–132.
- Ng, S. P., Tse, P. C. and Lau, K. J. (2001). Progressive failure analysis of 2/2 twill weave fabric composites with moulded-in circular hole. *Composites Part B* **32**, pp. 139–152.
- Niederstadt, G. (1985). *Leichtbau mit kohlefaserverstärkten Kunststoffen*. Expert Verlag, Sindelfingen.
- Pahr, D. H. (2000). Final report: Mechanical behaviour of acoustic skins. Technical report, Institute of Lightweight Structures and Aerospace Engineering, Vienna University of Technology.
- Pahr, D. H., Daxner, T., Rammerstorfer, F. G. and Böhm, H. J. (2001). On micro/meso/macro modeling of composite lightweight materials and structures. In: *Proc. of First Asian-Pacific Congress on Computational Mechanics, November 20-23, 2001, Sydney, Australia*, pp. 753–762.
- Pahr, D. H., Hampel, S. and Rammerstorfer, F. G. (2003). Extension and implementation of Puck's uni-directional layered laminate damage model in a finite element program. In: *GAMM 2003, 24 - 28 March, 2003, Padua, Italy*.
- Pahr, D. H., Rammerstorfer, F. G., Rosenkranz, R., Humer, K. and Weber, H. W. (2002). A study of short-beam-shear and double-lap-shear specimens of glass fabric/epoxy composites. *Composites Part B* **33**, pp. 125–132.
- Puck, A. (1996). *Festigkeitsanalyse von Faser-Matrix-Laminaten*. Carl Hanser Verlag, München, Wien.
- Puck, A., Kopp, J. and Knops, M. (2002). Guidelines for the determination of the parameters in Puck's action plane strength criterion. *Comp. Sci. and Tech.* **62**, pp. 371–378.
- Puck, A. and Schürmann, H. (1998). Failure analysis of FRP laminates by means of physically based phenomenological models. *Comp. Sci. and Tech.* **58**, pp. 1045–1067.

- Rammerstorfer, F. G. and Böhm, H. J. (1998). *Composite Engineering*. Lecture Notes, Vienna University of Technology, Wien.
- Reckling, K. A. (1967). *Plastizitätstheorie und ihre Anwendung auf Festigkeitsprobleme*. Springer-Verlag, Berlin-Heidelberg.
- Rose, C. A. and Herakovich, C. T. (1993). An approximate solution for interlaminar stresses in composite laminates. *Comp. Eng.* **3**, pp. 271–285.
- Rosenkranz, P., Humer, K., Weber, H. W., Pahr, D. H. and Rammerstorfer, F. G. (2001). Static and dynamic scaling experiments on double lap shear specimens at room temperature and at 77 K. *Cryogenics* **41**, pp. 21–25.
- Rosselli, F. and Santare, M. H. (1997). Comparison of short beam shear (SBS) and interlaminar shear device (ISD) tests. *Composites Part A* **28A**, pp. 587–594.
- Saleeb, A. F. and Chen, W.-F. (1983). *Constitutive equations for engineering materials*. John Wiley & Sons, Inc., West Lafayette, Indiana.
- Schneider, K., Lauke, B. and Beckert, W. (2001). Compression shear test (CST) - A convenient apparatus for the estimation of apparent shear strength of composite materials. *Appl. Comp. Mat.* **8**, pp. 43–62.
- Shokrieh, M. M. and Lessard, L. B. (1998). An assessment of the double-notch shear test for interlaminar shear characterization of a unidirectional Graphite/Epoxy under static and fatigue loading. *Appl. Comp. Mat.* **5**, pp. 49–64.
- Skrna-Jakl, I. C. (1994). *Numerical and Experimental Investigations of Interlaminar Stresses and Free Edge Effects in Integrally Stiffened, Layered Composite Panels*. Fortschritt-Berichte VDI Reihe 18 Nr. 188. VDI-Verlag, Düsseldorf.
- Spanner, S. R., Brown, A., Hay, D. R., Mustafa, V., Notvest, K. and Pollok, A. (1990). *Fundamentals of acoustic emission testing*, volume 5, pp. 12–44. American Society of Nondestructive Testing, USA.
- Stiftinger, M. and Rammerstorfer, F. (1996). *Advances in Analysis and Design of Composites - Semi-Analytical Finite Element Formulations for Delamination Prediction in Layered Composite Structures*, pp. 61–72. Civil-Comp Press, Edinburgh.

- Stiftinger, M. A. (1996). *Semi-Analytical Finite Element Formulations for Layered Composite Shells with Consideration of Edge Effects*. Fortschritt-Berichte VDI Reihe 18 Nr. 203. VDI-Verlag, Düsseldorf.
- Suquet, P. M. (1987). *Lecture Notes in Physics - Homogenization Techniques for Composite Media*, chapter IV. Springer-Verlag.
- Tan, S. (1988a). Effective stress fracture models for unnotched and notched multidirectional laminates. *J. Comp. Mat.* **22**, pp. 322–340.
- Tan, S. (1988b). Mixed-mode fracture notched composite laminates under uniaxial and multiaxial loading. *Eng. Frac. Mech.* **31**, pp. 733–746.
- Tsai, S. W. and Wu, E. M. (1971). A general theory of strength for anisotropic materials. *J. Comp. Mat.* **5**, pp. 58–80.
- van Rens, B. J. E., Brekelmans, W. A. M. and Baaijens, F. P. T. (1998). Homogenization of the elastoplastic behavior of perforated plates. *Comput. and Struct.* **69**, pp. 537–545.
- Whitcomb, J. D., Raju, I. S. and Goree, J. G. (1982). Reliability of the finite element method for calculating free edge stresses in composite laminates. *Comput. and Struct.* **15**, pp. 23–37.
- Withney, J. and Nuismer, R. (1974). Stress fracture criterion for laminated composites containing stress concentrations. *J. Comp. Mat.* **8**, pp. 253–265.
- Wolters, J. (1989). *Anwendungen der Schallemissions-Messtechnik zum Beschreiben von Versagensmechanismen in partikelgefüllten Thermoplasten*. Fortschritt-Berichte VDI Reihe 5 Nr. 163. VDI-Verlag, Düsseldorf.
- Xiao, J. and Bathias, C. (1993). Modified Tan's model for the strength prediction for woven laminates with circular holes. *Comp. Eng.* **3**, pp. 961–973.
- Xie, M. and Adams, D. F. (1996). A nonlinear finite element analysis for composite materials. *Finite Elements in Analysis and Design* **22**, pp. 211–223.

Curriculum Vitae

Name : Dieter H. Pahr
Title : Dipl.-Ing.
Date of birth : June 15, 1973
Place of birth : Vienna, Austria
Nationality : Austria

Education

1987 – 1992 “Höhere Technische Bundeslehranstalt”, Pinkafeld (A);
July 92 – Feb. 93 Compulsory military service;
1993 – 1998 Studies of mechanical engineering at the Vienna University of
Technology (A). Diploma thesis: “Design of a new driving unit
of a bulb turbine”
Oct. 1998 Graduated with honours with the degree of Diplomingenieur;
since Nov. 1998 Doctoral student at the Institute of Lightweight Structures and
Aerospace Engineering, Vienna University of Technology (A).
Working title of thesis: “Experimental and Numerical Investiga-
tions of Perforated FRP-Laminates”.

Professional Development

since Dec. 1998 Assistent Professor at the Institute of Lightweight Structures and
Aerospace Engineering, Vienna University of Technology (A);
July – Sept. 2000 Visiting scientist at the NASA Glenn Research Center, Ohio
(USA);

Vienna, 10th March 2003

Dieter H. Pahr